

**Experimental Methods for the Analysis of Frost Nucleation and Frost Growth on
Hydrophilic and Hydrophobic Coated Flat Plate Surfaces in Forced Convection Channel
Flows**

by

Burak Muhammed Adanur

A thesis submitted to the Graduate Faculty of
Auburn University
in partial fulfillment of the
requirements for the Degree of
Master of Science

Auburn, Alabama
December 14, 2019

Keywords:

Frost Growth, Nucleation, Hydrophobic, Hydrophilic, Forced Convection, Surface Coatings

Copyright 2019 by Burak Muhammed Adanur

Approved by

Dr. Lorenzo Cremaschi, Chair, Associate Professor
Dr. Sushil Bhavnani, Associate Department Chair
Dr. Roy Knight, Associate Professor

Abstract

An experimental system was designed and built to explore the effect of coated surfaces on frost formation. The experimental system consists of a wind tunnel test apparatus, dew point sensors, thermocouples for temperature measurements, pressure sensors and other devices. The experimental system is equipped with a computerized data acquisition and storage system. The temperature and humidity of the experimental system is computer controlled. The system is suitable to study the condensation and frosting effects on various coated and uncoated surfaces.

The formation of frost and ice decreases the energy efficiency of refrigeration systems and of air-source heat pump systems. This work presents experimental data of frost nucleation and frost growth on cold flat plates operating in frosting conditions with air forced convective flow. The plates surfaces had different wettability: from an uncoated aluminum surface with fine finish roughness and contact angle of 75° , to hydrophobic ($\theta \approx 110-116^\circ$) and hydrophilic ($\theta \approx 19-29^\circ$) coatings. An experimental technique was developed in order to mimic actual field type operating conditions of convective channel flow experienced by fin structures of heat exchangers of typical air-source heat pump systems. The surface wettability characteristics affected the elapsed time and the initial thickness of the frost before the droplets froze on the test plates. They also affected the starting point for the phase changeover from crystal growth to frost growth. The hydrophobic surface had early phase changeovers and high thresholds of the frost thickness before switching to the frost growth phase due to the presence of large droplets on the surfaces before they froze into ice beads. Fine-finished aluminum surface and hydrophilic coating had delayed phase changeovers and low frost thicknesses with respect to the other surfaces.

During pull-down tests, nucleation on the hydrophilic surface occurred quickly, leaving less time for disc-like shaped water droplets to continue to grow in the radial and vertical directions before freezing. Frost thicknesses followed “S” shaped like profiles due to transitions of droplets to ice beads, to crystals growth, and to initial frost accretion on the top of the ice beads. The wettability characteristics of the surfaces affected the elapsed time at which these changeovers occurred and the thresholds of the frost thickness when switching to the frost growth phase.

Acknowledgments

I would like to thank my advisor Dr. Lorenzo Cremaschi for his support, guidance and encouragement throughout this work. His help has been invaluable.

I would also like to thank my committee members Dr. Sushil Bhavnani and Dr. Roy Knight for their support.

I would like to acknowledge and thank the members of the research group Ellyn Harges, Amy Strong and Pratik Deokar for their help in the lab.

I would like to thank Dr. Amy Betz and her research group at Kansas State University (KS, USA) for providing the coatings of the test plates used in this work.

I thank the National Science Foundation, Chemical, Bioengineering, Environmental, and Transport Systems Division for supporting my research through the Award No. 1604084, which is appreciated.

Last but not least, I would like to thank my wife Sumeyye Adanur for her patience, encouragement and support throughout my graduate studies.

Table of Contents

Abstract	ii
Acknowledgments.....	iv
Table of Contents	v
List of Tables	viii
List of Figures.....	ix
Nomenclature	xiv
Chapter 1: Introduction	1
Chapter 2: Literature Review	4
2.1 Frost Nucleation.....	4
2.2 Frost Properties	8
2.3 Measurement Methods for Frost Properties.....	15
2.4 Summary of Literature Review and the Approach of this Thesis.....	16
Chapter 3: Thesis Objective.....	19
Chapter 4: Experimental Setup	21
4.1 Introduction.....	21
4.2 Experimental Facility.....	21
4.2.1 EGW booster assembly.....	24
4.2.2 Steam Humidifier.....	27
4.3 Test Apparatus	28

4.3.1 Inlet duct	31
4.3.2 Test section assembly	32
4.3.3 Test plate clamping mechanism.....	35
4.3.4 Test Section Airflow Handling	37
4.3.5 Outlet Airflow Handling.....	38
4.4 Sensor Instrumentation	39
4.4.1 Temperature probes	43
4.4.2 IR Camera	43
4.4.3 Videoscope.....	45
4.4.4 Dew Point Sensor.....	46
4.4.5 Pressure Transducer	48
Chapter 5: Experimental Procedure	51
5.1 Introduction.....	51
5.2 Achieving the test condition	51
5.3 Constant surface temperature test procedure	52
5.3.1 Manual frost mass measurement procedure.....	54
5.3.2 High humidity testing procedure	56
5.4 Pull-down test procedure	57
5.5 Cycling test procedure	57
5.6 Surface cleaning procedure between experiments	58
5.7 Test plate replacement and plate cleaning procedure	59
Chapter 6: Data Analysis	62
6.1 Introduction.....	62

6.2 Frost Thickness Image Processing.....	62
6.3 IR Camera Image Processing.....	64
6.4 Frost mass calculations	65
6.5 Dew point temperature correction	66
6.6 Uncertainty Analysis.....	67
Chapter 7: Calibration and Verification of Test Setup	69
7.1 Introduction.....	69
7.2 Double tee calibration test	69
7.3 Steady state wet test	71
7.4 Sensor calibration and verification	76
7.4.1 Temperature	77
7.4.2 Air Water Content – ω	80
Chapter 8: Results and Discussion.....	82
8.1 Frost characteristics during tests with small variations of the surface temperature ...	82
8.2 Frost characteristics during pull-down tests	87
8.3 Effect of test conditions on hydrophobic, hydrophilic and uncoated surfaces	92
8.4 Cycling tests.....	104
Chapter 9: Conclusions	105
References.....	109

List of Tables

Table 1: Measurement devices, set points, ranges, accuracies, and control tolerances	42
Table 2: Set point conditions for steady state wet tests	71
Table 3: Nusselt number for hydrodynamically and thermally developed laminar flow in various cross-sections [Ozisik, M. N., Heat Transfer: A Basic Approach, McGraw-Hill Book Company, 1985].....	74
Table 4: Frost variables during the pull-down tests for the all surfaces (air at 5 °C and 78-80 % R.H., 8.5 m ³ /h)	87
Table 5: Test Conditions and Legend Number for Figure 43 to Figure 54	92
Table 6: Frost characteristics for test No. 1 conditions (air at 5 °C and 80 % R.H., 8.5 m ³ /h)	98
Table 7: Summary of cycle duration results from cycling tests.....	104

List of Figures

	Page
Figure 1: Schematic of the experimental test facility	22
Figure 2: Chiller (left) and pump module (right).....	24
Figure 3: EGW booster assembly	26
Figure 4: Photo of steam generator.....	28
Figure 5: Schematic of main test apparatus	29
Figure 6: Isometric model of test apparatus.....	29
Figure 7: Isometric model of test apparatus (cross section)	30
Figure 8: Picture of the test apparatus inside the large wind tunnel	30
Figure 9: Inlet duct construction	31
Figure 10: Inlet sensor layout	32
Figure 11: Schematic of T-block assembly (airflow indicated by arrows).....	34
Figure 12: Photo of thermoelectric cooling module from Custom Thermoelectric (model # 19911-5L31-03CQ).....	34
Figure 13: Cross section of test section and custom clamping system	36
Figure 14: Test section where the coated surface is positioned.....	38
Figure 15: LabVIEW data acquisition and computer control system.....	40
Figure 16: Illustration of the frost visualization sensors (HR CCD camera and IR camera) with respect to the test plate.	41
Figure 17: Diagram of test apparatus with sensor positions and their distance to the leading edge of the test section	42

Figure 18: Representation of optically translucent quality of zinc selenide in the infrared spectrum compared to the optically opaque quality of acrylic and borosilicate glass.....	44
Figure 19: Pressure measurement locations.....	48
Figure 20: Outlet nozzle and pressure sampling nodes	50
Figure 21: Test plate surface temperature vs. time during entire a typical frost test.....	53
Figure 22: Thickness profile vs. time during the entirety of a typical frost test (square points are the measured thickness from the HR CCD camera)	53
Figure 23: Images from IR camera showing typical type of iced droplets (a) contaminated hydrophilic surface; (b) new surface never cleaned; (c) after cleaning with Method 1; and (d) after cleaning with Method 2	58
Figure 24: (a) Flattened image from video scope, and (b) frost outline created from the actual image.....	62
Figure 25: Sample frost thickness analysis.....	63
Figure 26: Droplet size (a) and (b) actual ice bead shapes and sizes immediately after freezing	65
Figure 27: Example of inlet and outlet dew point temperature correction	67
Figure 28: Layout of double T-block calibration test.	70
Figure 29: Temperature comparison at the inlet and outlet of the test section for steady state wet tests	72
Figure 30: Humidity ratio comparison at the inlet and outlet of the test section for steady state wet tests.....	73
Figure 31: Ultra accurate thermometer	77
Figure 32: Circulating temperature bath.....	78

Figure 33: Example of temperature measurements of thermocouples at test section inlet during an iso-temperature check	79
Figure 34: Example of water content recordings during an iso- ω check.....	81
Figure 35: Frost thickness vs. time for all surfaces (coatings) during the nitrogen displacement tests - Frost thickness during the entire test period (Heat Flux of 1300-1500 W/m ² , T _s = -15 °C, T _{a,in} = 5°C, Humidity inlet of 80 % R.H., Flow Rate of 8.5 m ³ /h).....	83
Figure 36: Frost thickness vs. time for all surfaces (coatings) during the nitrogen displacement tests - Frost thickness during the initial early frost nucleation stage (Heat Flux of 1300-1500 W/m ² , T _s = -15 °C, T _{a,in} = 5°C, Humidity inlet of 80 % R.H., Flow Rate of 8.5 m ³ /h).....	83
Figure 37: Frost density vs. time for all surfaces (coatings) during the nitrogen displacement tests - Frost density during the entire test period (Heat Flux of 1300-1500 W/m ² , T _s = -15 °C, T _{a,in} = 5°C, Humidity inlet of 80 % R.H., Flow Rate of 8.5 m ³ /h)	84
Figure 38: Frost density vs. time for all surfaces (coatings) during the nitrogen displacement tests - Frost density during the initial early frost nucleation stage (Heat Flux of 1300-1500 W/m ² , T _s = -15 °C, T _{a,in} = 5°C, Humidity inlet of 80 % R.H., Flow Rate of 8.5 m ³ /h) ..	85
Figure 39: Time dependent variables for the surfaces (coatings) during the nitrogen displacement tests - Frost surface temperature vs. time (Heat Flux of 1300-1500 W/m ² , T _s = -15 °C, T _{a,in} = 5°C, Humidity inlet of 80 % R.H., Flow Rate of 8.5 m ³ /h)	86
Figure 40: Time dependent variables for the surfaces (coatings) during the nitrogen displacement tests - Air-side convective heat transfer coefficient (normalized) vs. time (Heat Flux of 1300-1500 W/m ² , T _s = -15 °C, T _{a,in} = 5°C, Humidity inlet of 80 % R.H., Flow Rate of 8.5 m ³ /h).....	86

Figure 41: Frost thickness vs. time for all surface (coatings) during the pull-down tests - Frost thickness during the entire test period (Heat Flux of 1300-1500 W/m ² , T _s = -15 °C, T _{a,in} = 5°C, Humidity inlet of 80 % R.H., Flow rate of 8.5 m ³ /h).....	88
Figure 42: Frost thickness vs. time for all surface (coatings) during the pull-down tests -Frost thickness during the transitions from droplets to ice beads, and to frost growth (Heat Flux of 1300-1500 W/m ² , T _s = -15 °C, T _{a,in} = 5°C, Humidity inlet of 80 % R.H., Flow Rate of 8.5 m ³ /h).....	89
Figure 43: Frost density vs. time for all surfaces during the pull-down tests - Frost density during the entire test period (Heat Flux of 1300-1500 W/m ² , T _s = -15 °C, T _{a,in} = 5°C, Humidity inlet of 80 % R.H., Flow Rate of 8.5 m ³ /h)	91
Figure 44: Frost density vs. time for all surfaces during the pull-down tests - Frost density during the transitions from droplets to ice beads, and to frost growth (Heat Flux of 1300-1500 W/m ² , T _s = -15 °C, T _{a,in} = 5°C, Humidity inlet of 80 % R.H., Flow Rate of 8.5 m ³ /h)..	91
Figure 45: Test results from test conditions No. 1 - Frost mass vs. time	94
Figure 46: Test results from test conditions No. 1 - Surface temperature vs. time	94
Figure 47: Test results from test conditions No. 1 - Normalized heat transfer coefficient vs. time (h _o = 120 W/m ² -K).....	95
Figure 48: Test results from test conditions No. 1 - Pressure drop vs time.....	95
Figure 49: Frost thickness vs time for test conditions No. 1	97
Figure 50: Density vs time for test conditions No. 1	97
Figure 51: Frost thickness vs time for test conditions No. 2	100
Figure 52: Density vs time for test conditions No. 2	100
Figure 53: Frost thickness vs time for test conditions No. 3	101

Figure 54: Density vs time for test conditions No. 3	102
Figure 55: Frost thickness vs time for test conditions No. 4	103
Figure 56: Density vs time for test conditions No. 4	103
Figure 57: Example of pressure drop across test section for cycling test.....	104

Nomenclature

A_s	surface area of the test plate (m^2)
h	heat transfer coefficient (W/m^2-K)
$H_{channel}$	height of the channel above the plate (m)
m	mass (kg)
\dot{m}	mass flow rate (kg/s)
q''	heat flux (W/m^2)
R	resistance (m^2-K/W)
T	temperature (K)
t_{step}	time step (s)
\dot{V}	volume flow rate (m^3/hr)
Vol	volume (m^3)

Greek symbols

δ	frost thickness (m)
θ	surface contact angle (degrees)
ρ	density (kg/m^3)
ω	absolute humidity ratio (kg water vapor/kg dry air)

Subscript

a	air
f	frost

fs frost surface
in inlet of the test section
out outlet of the test section
s test plate surface
tee T-block flux meter

Abbreviations

EES Engineering Equation Solver
EGW Ethylene Glycol and Water mixture
RH Relative Humidity
RTD Resistance Temperature Detector
TECM Thermoelectric Cooling Module

Chapter 1: Introduction

Frost formation and growth is a phenomenon that is usually unwanted. Therefore, analysis and understanding of frost formation and growth parameters are critical for many applications to be able to stop or reduce it. This knowledge is critical for the performance of heat exchangers, gas coolers, heat pumps, freezers, refrigeration systems, etc. The performance of these devices are negatively affected by frost formation and growth. Frost formed on aircraft wings affect the lift and drag on airplanes. Other areas where frost formation is critical include transmission lines, wind turbine blades, oil and gas rigs, ships, etc.

If there is a cold surface below freezing temperature, humid air causes frost formation on the surface. Water droplets form first and as the cooling continues, they freeze and turn into ice particles. This is considered to be the beginning of the frost formation. For sufficiently dry air, water can immediately freeze on the surface without a liquid phase. These ice particles continue to grow in vertical and horizontal directions with respect to the cold surface with the continuous feed of moisture from the humid ambient air.

Frost formation and growth is another wonder of nature: each frost particle forms and grows differently just like each flame and each snowflake is different. Frost growth is a complicated process that is still not very well understood. Frost characteristics such as thickness, density, growth rate, mass, porosity and surface temperature are affected by many ambient conditions such as air humidity, air temperature, air flow rate and surface conditions, etc.

Frost formation decreases the energy efficiency of refrigeration and heat pump systems. Frost accretion is a transient phenomenon that includes variation of frost thickness, frost mass,

frost temperature, heat flux (or heat transfer coefficient), mass flux (or mass transfer coefficient), and freezing droplet diameter. It is noteworthy to mention that frost thermal conductivity is also an important property that needs to be measured or estimated during frost growth. The challenge is that all of these variables are time-dependent during the heat and mass transfer process, and they are fairly sensitive to air temperature, humidity, and velocity. They also depend on surface conditions and surface geometries.

Frost growth is affected by ambient and surface temperatures, humidity, contact angle, and coating thickness. Frost accretion penalizes energy efficiency of air-source heat pump and refrigeration systems and can also have negative effects for other applications such as aircraft flight surfaces. Therefore, methods of reducing or delaying frost growth by reducing its height and density would help with the energy efficiency.

Frost nucleation and frost growth are transient phenomena and the observations are difficult to generalize to a broader range of conditions and surface types. In addition, the instantaneous values of all key variables necessary to develop and validate frost models are often not measured concurrently and distinctly during the same frosting test, or not completely documented and reported.

This thesis presents the design, development, and operation of an experimental setup that explores these frosting phenomena. A large experimental facility was used to maintain air and surface conditions inside of a small wind tunnel test apparatus. Some of these equipment include a chiller and pump module, a large recirculating 2ft x 2ft cross section wind tunnel, cooling coils, heaters, humidifiers, and air handling devices. Sensor instrumentation include thermocouples, dew point sensors, mass flow meters, pressure transducers, and frost visualization sensors including a high definition CCD camera and an infrared camera. Condition variables such as air temperature

and humidity as well as different surface coatings were varied to observe the effect that each of these variables had on freezing and frosting phenomena on a flat plate in forced convection duct conditions.

Chapter 2: Literature Review

The phenomena of frost starts with condensation of moist air on a cold surface which nucleates into ice thus forming an ice layer. Then, dendritic crystals start growing in vertical and horizontal directions, which is followed by frost growth and densification. Although frost phenomena is as old as the earth, the research about it has increased within the last couple of decades. A summary of the relevant research in this important area is given below.

2.1 Frost Nucleation

The initial stages of droplets nucleation and growth on surfaces undergoing freezing operating conditions include water vapor condensation. Several studies on the basic behavior of water droplets deposited on hydrophobic and hydrophilic surfaces and under condensing conditions identified and quantified the surface wettability effects on droplets growth and motion. The effect of surface wettability on frost formation of flat plates and fin structures was investigated by several researchers (Şahin (1994), Hayashi et al. (1997), Hoke et al. (2000), Lee et al. (2004), Wu et al. (2007), Tourkine et al. (2009), Kim and Lee (2011), Alizadeh et al. (2012), Huang et al. (2012), Rahman and Jacobi (2015), Sommers et al. (2016), Sommers et al. (2018), Hermes, et al. (2018)). Once frost started to accumulate, then defrosting could be performed after a certain time. Excellent recent review papers in these topics are the ones of Kim et al. (2017) and Song and Dang (2018).

Sahin (1994) did an experimental study to investigate the nucleation stage of frost formation to “clarify” the fundamental nature of early stage crystal growth, as opposed to crystal growth after a porous layer of frost had grown. He analyzed the effect of aluminum and Plexiglas

plate temperatures, air temperature, relative humidity and Reynolds (Re) number on frost height, deposition and density. He reported that air temperature, air humidity and plate temperature affect the frost layer thickness. High mass deposition is caused by high humidity, Re number and temperature difference. Frost surface temperature affects the frost density the most. He concluded that frost formation starts when the surface is covered with a thin, smooth frost layer. Then, frost crystals form on the thin frost layer and grow vertically. The frost layer height was measured using a micrometer and cathetometer. The diameter of the frost column grows with vapor diffusion through the voids.

Hayashi et al. (1997) studied frost formation stages and resulting frost properties on an acrylic plate within -25 to 0° range using microscopes and photographs. They categorized frost formation process under three stages:

- Crystal growth stage
- Frost layer growth stage
- Frost layer full growth stage

In the first stage, cryosurface is covered first with a thin frost layer. Then, frost crystals form on the frost layer and grow vertically similar to trees growing in a forest. In the second stage, the crystals start developing branches in 3D growth and the frost layer becomes almost flat. In the third stage, the frost layer experiences full growth. Then, they classified the frost formation types into four groups. In Type A, the frost growth takes place by having feather type crystal growth. In Type B, the crystals are plate-like, rather than feather shape. In Type C, needle-type crystals cause the growth. Type D is similar to Type C with a denser frost growth resulting in homogeneous frost layer. They explained how frost density and frost thermal conductivity are affected by each type of growth. They also developed a model to represent the frost layer.

Using a microscope and high speed imaging techniques, Hoke et al. (2000) studied the effect of several substrates (polytetrafluoroethylene (PTFE), Kapton polyimide, glass, etc.) on frost inception and growth with different contact angles in laminar airflow. They found that substrate temperature, humidity, and contact angle affect the water distribution on the substrate at the end of the condensation period. Small and uniform droplets are caused by cold substrates and larger droplets are caused by small contact angles. Hydrophobic substrates caused lower condensate densities compared to that of hydrophilic substrates. Substrate conditions also affect the structure and form of the ice after freezing. They observed that a protrusion formed on top of each droplet on a hydrophobic surface, which was not visible on a hydrophilic surface. They used a model to simulate the frost growth rate and density and compared with the experimental data.

Lee et al. (2004) developed frost maps for two different surfaces with different hydrophilic characteristics and found ambient conditions associated with the formation of frost structures using a wind tunnel in a humid airflow. They classified the frost structures as feather type, grass type and plate type for both surfaces. Feather type frost is caused by high humidity and plate type frost is caused by low humidity. They showed that surface with low dynamic contact angle had lower frost thickness and higher frost density compared to the surface with high dynamic contact angle; however, the frost structures on both surfaces were similar.

Delayed freezing was observed on hydrophobic microtextured copper surfaces by Tourkine et al. (2009). They suggested that by slightly tilting the substrate surface, the drops can be removed without freezing, which might be useful in design of cooling and similar systems.

Alizadeh et al. (2012) studied the dynamics of ice nucleation on hydrophobic surfaces (Si-PEG, Si-F, Si-STex-F, Si-DTex-F) using infrared thermometry and high speed photography. They showed experimentally that ice nucleation in low humidity can be delayed by changing the

chemistry and texture of the surface. Limiting water-surface contact area plays an important role in delaying nucleation on super hydrophobic surfaces by reducing heat transfer and probability of nucleation. They also made an analysis based on classical nucleation theory to predict nucleation rates under icing conditions. They concluded that icing of the surface is dominated by water-surface interface and high contact angles reduce the water-plane contact area and therefore reduce the nucleation rate for intermediate super cooling.

Huang et al. (2012) experimentally examined the effect of contact angle on water droplet freezing process on plain and hydrophobic copper surfaces under natural convection. They took SEM pictures of different copper surfaces (plain and etched) for comparison purposes as well as high resolution pictures of water droplet freezing stages and crystal growth. The maximum contact angle they were able to get was 156.2° , which gave nearly a perfect spherical shape of the water droplet. They observed a sharp protruding point at the top of the droplet where the frost crystals form first and spread away. They concluded that increasing contact angle (increasing hydrophobicity of the surface) increases the freezing time of water droplet due to smaller contact area between the droplet and surface. They also observed that hydrophobic copper surface offer more favorable conditions for faster crystal growth on the droplet surface compared to the plain copper surface, which makes the selection of hydrophobic copper surface questionable.

Sommers et al. (2016) and Sommers et al. (2018) focused on surface wettability effects on frost density for water droplets freezing on surfaces subjected to natural convection flow regimes. Sommers et al. (2016) examined the effect of surface wettability on frost mass, thickness and densification under natural convection. They used three conditions on aluminum surface: untreated, hydrophobic and hydrophilic. The relative humidity was kept constant in the experimental system using an ultrasonic humidifier. Frost images were taken by a CCD camera.

Compared to the untreated aluminum surface, on average, frost density was increased by 26% on the hydrophilic surface and decreased by 39% on the hydrophobic surface. They checked their data against the models in the literature and realized that untreated surface data agreed reasonably well but hydrophilic and hydrophobic surface data did not. Therefore, they suggested that surface wettability should be included in any frost densification model as a parameter. Sommers et al. (2016) later extended their work to examine the effect of environmental conditions on frost layer growth with different contact angles. They developed a semi-empirical model to predict frost thickness in which surface contact angle, Jakob number, humidity and time were included as parameters. The model gave an average predictive error of 12%.

Hermes, et al. (2018) proposed a semi-empirical model to predict frost deposition on hydrophilic and hydrophobic surfaces under natural flow. They developed an algebraic equation to determine frost thickness based on time, modified Jakob number, humidity and contact angle. The semi-empirical model errors were within $\pm 15\%$, with an average of 11.7%.

2.2 Frost Properties

Several researches studied the frost properties after frost nucleation stage including frost growth, frost mass, frost thickness, frost density, frost conductivity and porosity.

Brian et al. (1970) deposited water frost on a nitrogen cooled copper plate in a wind tunnel with forced humid air under different conditions of velocity, humidity and temperature. They determined the frost densities and thermal conductivities. They used the data to develop an analytical method that takes internal diffusion process in the frost into account. Their density measurements in the thin frost layer showed that there was no significant density gradients in the frost, which was a surprising result.

Lee et al. (1997) developed a one dimensional analytical method for frost formation on a flat surface and compared its results with the experimental data, which showed a 10% difference. In their method, they considered the molecular diffusion of water and sublimation of water-vapor in the frost layer. The effects of air velocity and relative humidity on frost thickness and frost surface temperature were determined. They reported that frost surface temperature increases with increasing relative humidity and air velocity.

Yun et al. (2002) modeled the frost growth and properties on an aluminum flat plate at subfreezing temperature. They measured frost roughness and developed an empirical relation for average frost roughness. They calculated heat and mass transfer coefficients using modified Prandtl scheme while including frost roughness and boundary layer thickness. They developed formulas for frost layer growth to estimate the frost thermal conductivity, thickness, mass concentration and density with respect to time and location.

Cheng and Shiu (2002) experimentally investigated the frost thickness spatial variation and the formation and pattern of crystal growth on a copper cold plate in atmospheric flow in a suction type open loop wind tunnel using a microscopic image system. They used methanol as the refrigerant in the cooling unit which was made of Plexiglas to reduce heat transfer from the surroundings. The image system included a CCD camera, a zoom enlarging lens unit and an illuminator unit. The images were analyzed with Matrox image processing software. The cold plate temperature was measured using T-type thermocouples. They observed that frost density and thickness increase with increasing relative humidity. At lower air velocity, frost thickness increases with an increase in air temperature; at higher air velocity, frost thickness decreases with increasing air velocity. They likened the structure of the frost layer to a forest in which the trees grow at different rates and shapes.

Lee et al. (2003) developed a model to predict frost formation including thickness growth, density and surface temperature on flat surfaces and compared their model with the previous models. They used aluminum tapes for the measurement of frost mass. They claimed that the previous models gave erroneous results compared to their model, which gave results within an error of 10% compared to the experimental data after the early stages of frost formation.

Cheng and Wu (2003) examined the early frost formation on a Plexiglas cold plate of 10 mm thickness in atmospheric air flow experimentally and theoretically. They used a microscopic image system to record the frost pattern and thickness every five seconds. They observed a multi-step ascending frost growth pattern that is caused by melting of frost crystals. By varying the surface temperature of the cold plate, they studied the effects of velocity, temperature and relative humidity. They verified their experimental results using a previous theoretical model with good agreement.

Yang and Lee (2004) proposed dimensionless correlations for predicting the properties of frost formed on a cold plate. Using dimensionless analysis, they correlated the thickness, density, surface temperature, effective thermal conductivity, average heat and mass transfer coefficients of the frost layer as functions of the Reynolds number, Fourier number, absolute humidity, and dimensionless temperature. They reported that the maximum error between the proposed correlations and the experiments was 10%. They claimed that, as a result, their correlations can be used to predict the average frost properties in certain ranges of air temperature, air velocity, absolute humidity and cooling plate temperature.

Qu et al. (2005) studied frost formation on an aluminum surface with regular and forced air flows. They observed a stepwise increase of the frost layer thickness. They suggested that initially water drop or ice particle growth increased the frost layer thickness first slowly followed

by rapid increase of the thickness caused by the growth of needle shaped ice crystals. Then, the column-shaped ice crystals grew lengthwise and widthwise alternatively, causing the frost layer thickness to increase fast and slow in turn.

Hermes et al. (2009) investigated the frost growth and densification on Perspex flat plates using an open loop wind tunnel to simulate the freezer compartment of the refrigerators within a range of air velocity, relative humidity, and plate surface temperatures. They used a digital camera with a software to monitor the plate surface changes. Frost surface temperature was measured with an infrared camera. First, they investigated the frost growth and densification experimentally. Then, based on this data, they developed a theoretical model to predict frost thickness and mass variation with time, based on the previous work. In the model, they simulated the frost as a porous medium. They reported that the difference between the theoretical model and experimental data was within $\pm 10\%$ for the prediction of frost thickness as a function of time. Then, they used the model to predict the frost growth and densification. They claimed that their model differs from the previous models because it is analytical and not based on heuristic approach. They concluded that frost growth is affected by the plate surface temperature the most.

Huang et al. (2010) studied the frost growth (crystal pattern and frost thickness) on a horizontal copper surface under forced air flow (2.2 – 8.0 m/s) and low air temperature (-5° to $+5^{\circ}$ C). They used a microscope, CCD camera and a luminescence illuminator to observe the frost growth in their experimental system. They found out that the cold surface temperature and relative humidity affected the frost growth almost linearly. Decreasing cold surface temperature and increasing RH increases the frost thickness drastically. Frost crystal growth and thickness are also affected directly by the air temperature and Reynolds number; however, this affect tended to diminish at higher air temperatures and Reynolds number higher than 37400.

Yoon et al. (2010) measured the frost thickness and frost mass experimentally on a flat plate using a 50% ethylene glycol aqueous solution as the coolant. Using a balance, they measured the frost mass every 30 minutes by measuring an aluminum tape before and after the test. They stated that it was difficult to measure instantaneous frost mass. The frost surface temperatures were measured using an infrared thermometer and T-type thermocouples. A digital CCD camera with a stepping motor was used to measure the frost thickness. The pictures of the frost was taken every 10 minutes. They measured the frost thickness profiles at four different positions. They suggested that it would be possible to determine the frost thickness profile by monitoring only the left side of the frost thickness. Using the experimental data, they developed correlation equations to predict the local and average frost thickness, frost density and frost mass. They experimentally investigated the effect of air temperature, air humidity, air velocity and surface temperature on the frost thickness and frost mass. In general, the correlation equations gave approximately 30-50% higher values than the experimental data. However, the difference between the estimated frost mass and measured frost mass was less than 8%. They suggested that the correlation equations they developed could be applied to the part of the freezer condition.

Cai et al. (2011) studied frost growth using hydrophobic (car wax) and hygroscopic (glycerol) coatings for the purpose of restraining frost growth. Frost growth was recorded using photographic techniques with a camera and CCD video camera. Their results showed that compared to normal copper surface, frost growth on hydrophobic and hygroscopic coatings were delayed. The frost height was lower with sparse distribution and less aggradations of ice crystals. As a result, they concluded that hydrophobic and hygroscopic coatings could be used in heat exchangers in refrigeration and air conditioning equipment. Each coating type had some advantages over the other one.

Wang et al. (2012) developed a model to predict the frost growth on a cold plate in a suction type wind tunnel using Hayashi correlation. They used a microscope attached to a CCD to visualize the frost growth and convert the captures to images using YRMV v.10 software. However, the image resolution was not very high. They used a variety of test conditions (air temperatures, relative humidities, air velocities and cold plate temperatures) to obtain experimental data. To reduce random error, they repeated each test three times, which limited the error to $\pm 3.5\%$. They developed a one dimensional theoretical model for quasi-steady state conditions. After validating their model for initial frost density based on the experimental results, they used their model to predict frost thickness, frost density, surface temperature and heat flux under different conditions. They reported that the simulated results agree with the experiments and previous literature within $\pm 10\%$.

Janssen (2013) suggested small scale rather than large scale experimental systems to understand the frost growth process better. He developed a small insulated polycarbonate chamber for the experiments under a variety of conditions. In the system, he used a camera with zoom lenses to capture images. He stated that most models related to frost growth parameters are applicable only to specific conditions albeit they are not very reliable. He developed a new algorithm to predict frost thickness for a range of conditions, which is based on partly experimental data and partly on some physical laws. He emphasized the importance of obtaining large data to be able to establish more accurate models with the help of computers.

Boreyko et al. (2013) examined if facile defrosting is possible on superhydrophobic surfaces. They investigated defrosting on chilled, nanostructured superhydrophobic surfaces. They reported that nanostructured superhydrophobic surfaces promote the growth of frost in a suspended Cassie state which enables its dynamic removal with partial melting at tilt angles less

than 15°. They developed a molecular dynamic simulation for the dewetting process on pillared graphite surface, which predicted that ice slab must be 90% melted for dewetting to occur.

Using a closed loop wind tunnel, Leoni et al. 2017, studied the frost formation and development on flat aluminum plate, carbon plate and aluminum foil experimentally and then compared their data to those of the predictive models with generally satisfactory agreement. A digital camera was used to photograph the frost layer and an infrared camera was used to measure frost surface temperature. They examined the effect of environmental conditions such as air velocity and temperature, relative humidity and plate temperature on frost properties such as thickness, density and thermal conductivity. They reported that the frost thickness, density and thermal conductivity are affected by the plate temperature and air relative humidity. Thermal frost conductivity increases with increasing air temperature, decreasing plate temperature and decreasing relative humidity. They verified the Lewis analogy using mass and heat flux measurements. They suggested that tortuosity of crystal shapes need to be studied in more detail. They also suggested that frost density predictive models need to be improved.

Schmiesing and Sommers (2017) examined defrosting performance of gradient pattern and nonpattern surfaces with different wettability in a small chamber: uncoated/untreated aluminum, hydrophilic coated surface, plain and hydrophobic surfaces with micro channels, microstructurally rough plain and hydrophobic surfaces. Each surface was subjected to cyclic one hour frosting first and then 10 minutes defrosting. They observed small defrosting behavior among the samples with a defrosting effectiveness between 52-77%. However, more water was removed from the gradient surfaces during defrosting. They concluded that defrosting is directly related to the thermophysical properties of the frost layer.

2.3 Measurement Methods for Frost Properties

Frost thickness can be measured by contact and non-contact methods. Methods of gathering frost thickness data include coupling a camera with a microscope (Cheng and Wu (2003), Huang et al. (2010), Cai et al. (2011), Wang et al. (2012)), using a camera with a zoom lens (Hoke et al. (2000), Cheng and Shiu (2002), Hermes et al. (2009), Yoon et al. (2010), Janssen (2013), Leoni et al. (2017)), using a micrometer (Lee et al. (2003), Lee et al. (1997), Sahin (1994), Yang and Lee (2004), Yun et al. (2002)), using laser displacement (Qu et al. (2005)), and using a cathetometer ((Sahin (1994), Hayashi et al. (1977))). Frost mass, and thus indirectly frost density, is almost always measured by removing a section of the test surface (or a tape or film covering the surface) and weighing on a balance.

It is difficult to obtain droplet size and freezing time data under forced convection conditions without disrupting the airflow, so there are only a few researchers who attempt this. Tao et al. (1993) placed their frosting surface directly after the exit of a small wind tunnel and positioned a microscope over the frosting aluminum surface to record droplet growth. Using a microscope, they observed frost growth on a cold plate. Bryant (1995) used a high-resolution CCD camera attached to the eyepiece of a stereo dissecting microscope to visualize the condensed droplets. Hoke et al. (2000) placed their entire microscopic test section on the stage of a scanning confocal microscope in order to see the droplets. Kim et al. (2016) used two high-resolution cameras to observe droplets; one was placed over the over a cut out in the top of their wind tunnel, while the other was placed in front of a second cut-out in the side.

There are currently two common methods of measuring the surface temperature of the frost: using thermocouples on or in the frost layer ((Brian et al. (1970), Hayashi et al. (1977))), and using an infrared device (Lee et al. (1997), Lee et al. (2003), Yang and Lee (2004), Hermes et al.

(2009), Leoni et al. (2017)). The first method is not ideal because it is invasive and thus has the potential to affect the measurements in an undesirable manner. It is difficult to obtain accurate measurements from the second method as an emissivity of the frost layer must be provided to the device. Lee et al. (1997) reports that an emissivity value of 0.94 was used for their measurements. A few studies report heat transfer data in the form of heat flux values ((Hoke et al. (2000), Lee et al. (2003), Yang and Lee (2004), Janssen (2013) or Nusselt numbers ((Yang and Lee (2004)), but many researchers do not collect heat transfer data at all. Hoke et al. (2000) reports data for both the frost layer and for initial droplets, but the data were gathered in different experiments and at different test conditions, creating some inconsistencies. Kim et al. (2017) and Song and Dang (2018) presented a literature reviews of several studies that investigated surface wettability effects on frost characteristics. Kim et al. identifies a need to investigate inter-droplet freezing and the study of ice propagation. Song and Dang also summarized methods for measuring frost characteristics and particularly how frost morphology impacts the frost density and thickness.

2.4 Summary of Literature Review and the Approach of this Thesis

In summary, frost growth is a complex, natural phenomenon that is still being studied. The literature review show that frost characteristics such as thickness, density, growth rate, surface temperature are affected by the experimental conditions such as air temperature, humidity, flow rate, surface conditions, etc. Just like snowflakes, each frost growth and characteristics are different than the others. There have been inconsistencies in the data reported in the literature regarding the frost inception and growth characteristics. Some results reported are even contradictory. Some theoretical models that are proposed in the literature are applicable to specific conditions and are not capable of predicting the frost formation and characteristics to a satisfactory level. Some models are heuristic in nature. The difference between experimental data and the

results of predictive models is too much to be acceptable. Therefore, it is necessary to do further experiments and measurements as well as theoretical studies for frost growth and characteristics to be able to develop a generalized understanding of frost growth for all practical conditions. Then, based on this background and more fundamental knowledge, a theoretical model could be developed to predict the frost phenomena satisfactorily.

In the previous work of our research group, a new model was presented for frost nucleation and frost growth on flat plates (Cremaschi, et al., 2018; Harges and Cremaschi, 2018a) and included the variability of the surface contact angle on the frost nucleation (Harges and Cremaschi, 2018b). The developed model was compared with the data from the literature, but an in-depth validation was recommended. This current research is a natural continuation of our research group's prior work and builds on it.

In this thesis, droplet growth and freezing time as well as frost thickness during a frost nucleation and subsequent frost growth processes are measured. Non-contact technique is used to measure the average frost thickness from a frost profile. The top and the leading edge of the test surfaces are recorded to provide the instantaneous measurements of droplet growth, droplets freezing time, as well as frost growth and frost layer thickness during each experiment. An in-situ calibrated noninvasive infrared thermal camera is used to measure the frost surface temperature while the test apparatus measured the instantaneous heat flux and frost mass deposited on the surfaces.

Results on a fine finish aluminum surface, on a hydrophobic-coated surface, and on a hydrophilic coated surface are presented for two modes of runs. In the first mode, the surface temperature had small variations during frosting nucleation. In the second mode of run, the surface temperature decreased from ambient to sub-freezing conditions, mimicking the actual behavior of

a fin in a heat pump system. This mode is referred to as “pull-down” mode and it is helpful for comparing the frosting performance of the coatings in realistic field type operating conditions. However, each physical quantity varies significantly with time and care should be taken to use the data from these modes of operation to develop physics-based frost models. The experimental methodology was refined such that the plate surface temperature remained constant (i.e. within $\pm 0.6^{\circ}\text{C}$ or 1.1°F) during initial frost nucleation and subsequent frost growth. This mode of operation allows to obtain data frost data that can be used for frost model development. Tests were conducted by varying the airflow velocity and humidity of the air in a parametric fashion, in order to quantify the effects of surface wettability characteristics on droplets elapsed time and radius at the onset of freezing. Measurement of droplets growth, droplets freezing time, as well as frost growth and frost layer thickness during frost nucleation and subsequent frost growth periods were done. The observations reveal that during the first minutes of frost nucleation, the wettability of the surface plays a significant role.

Chapter 3: Thesis Objective

The motivation behind this thesis is to develop an experimental setup that is capable of comparing frosting characteristics of coated flat plate surfaces in forced convection. The data collected by these experiments were tailored to be used to develop and verify a frosting model. The frosting model is currently being developed by another student and it is not part of this thesis.

The specific objectives of this thesis are:

- To design an experimental setup with the necessary devices to measure the effects of surface coatings on frost formation
- To build the test setup, install sensors and calibrate the apparatus
- To demonstrate that the new setup worked by testing three surfaces
 - Aluminum
 - Hydrophobic
 - Hydrophilic
- Freezing times, droplet diameters and frost thicknesses were measured at varying surface temperatures, air temperatures, air flow rates, and relative humidity.

This thesis was as part of a larger research project. My own contributions were to design, assembly, calibrate the test apparatus, and conduct preliminary tests of frost nucleation with the new testing methodology. I also serviced and repaired the test facility during the 3 years of the experimental campaign. Mrs. Ellyn Harges was involved with running some of the experiments

as well as the data reduction and analysis. In the present thesis 56 % of the figures in the results and discussion chapter were directly derived by myself. The remaining results derived with the assistance of Mrs. Eilyn Harges are included for the completeness of the work. Ms. Amy Strong developed the MATLAB software to analyze the frost thickness. Dr. Pratik Deokar assisted with the LabVIEW programming and data acquisition system.

Chapter 4: Experimental Setup

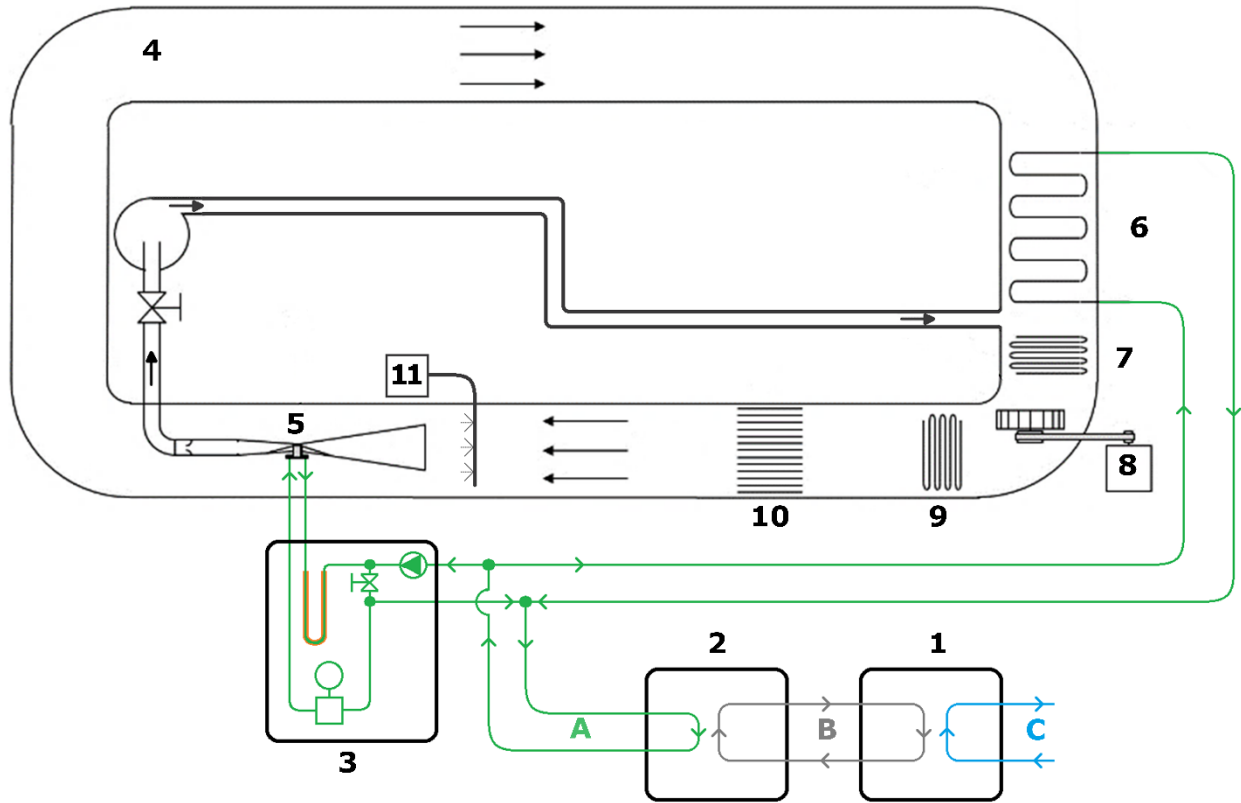
4.1 Introduction

Three test plate samples were machined from aluminum to dimensions of 25mm length (i.e., depth of the plate along the airflow direction by 152 mm width and 6 mm thickness (1 in x 6 in. x 0.25 in). These plates are referred to as the “test plates” throughout this thesis. Haque and Betz (2018) provided a detailed description of the coatings for the test plates. The first plate was uncoated aluminum surface with fine finish roughness and contact angle of $\theta \approx 75^\circ$. The second plate had its top surface coated with hydrophobic ($\theta \approx 110-116^\circ$) coating and the third plate had hydrophilic ($\theta \approx 10-29^\circ$) coating.

The experimental setup can be separated into two categories which this thesis will refer to as the experimental facility and the test apparatus. The experimental facility had the role of housing the test apparatus, providing a controlled environment for the experiment to be conducted in, and facilitating the collection of data from various sensor equipment. The test apparatus held, cooled, and facilitated smooth airflow over the test plate. Additionally, the test apparatus provided a structure for numerous measurement instrumentation to be housed.

4.2 Experimental Facility

A test plate was supported and enclosed by the test apparatus which facilitated the temperature control of the test plate surface temperature. The test apparatus was contained within a subsonic, closed return, climate-controlled wind tunnel with a flow path square cross section of 61 cm by 61 cm (2 ft x 2 ft) as shown in Figure 1 as item 4 with a detailed description in Figure 5.



1. Low temperature refrigeration system
2. Pump module
3. Booster assembly
4. Large wind tunnel
5. Test apparatus
6. Air cooling coil
7. Post-heater (hot water)
8. VFD blower
9. Post-heater (radiative electric)
10. Flow straightener
11. Steam humidifier
- A. Ethylene glycol flow loop
- B. Syltherm flow loop
- C. Chilled water flow loop

Figure 1: Schematic of the experimental test facility

Air temperature, humidity and wind speed entering and flowing around the test apparatus were maintained at constant levels during the experiments by a system of conditioning equipment. This equipment included a pump module, chiller, data acquisition (DAQ) system, and a computer.

A chilled ethylene glycol and water mixture (EGW) (item A) facilitated cooling of the air through cooling coils and heat removal to the test apparatus. An EGW booster assembly measured and controlled the temperature and flow rate of the EGW flowing through the test apparatus. The EGW also passed through the cooling coil for the large wind tunnel. This cooled the air and help to regulate the humidity of the wind tunnel by condensing moisture out of the air. A radiative air heater fine-tuned the air temperature after the cooling coil to bring the air temperature back up to operating conditions. Higher air temperatures could be reached with a hot water post-heater (item 7) facilitated by an external heat pump system; however, this was not used in this thesis. A steam humidifier was implemented at the inlet of the test apparatus to modify the humidity conditions of the experiment. A variable speed fan moved the airflow through the large wind tunnel. A flow straightener helped to ensure laminar flow up to the test apparatus.

The chilled EGW was supplied by a Mydax PM180 pump module (Figure 2) which contained a 180 gallon storage tank for EGW which acted as a large thermal mass resulting in a relatively constant EGW temperature. This pump module contained three pumps and in line and immersion heaters which controlled and maintained the EGW tank temperature.

A CryoDax 25 water-cooled chiller/heater (chiller) from Mydax was used to cool a Syltherm™ low temperature heat exchange fluid. On the hot side of the chiller, heat was extracted by chilled water sourced from the building facility. The chilled Syltherm™ provided cooling to the EGW through a brazed plate heat exchanger. The CryoDax 25 was capable of providing chilled fluid at a temperature range of -70°C to $+80^{\circ}\text{C}$. For this thesis, the chiller provided up to 24 kW of cooling.

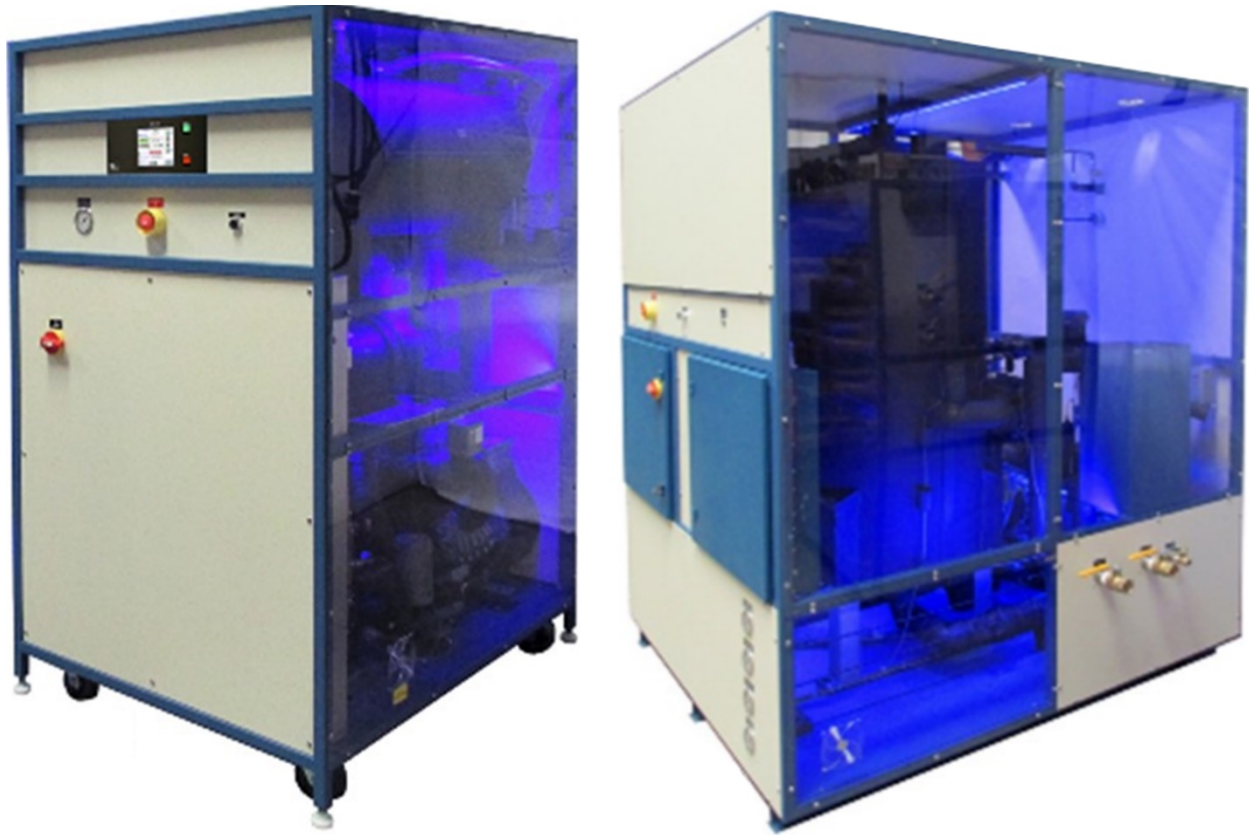


Figure 2: Chiller (left) and pump module (right)

4.2.1 EGW booster assembly

An EGW booster assembly was designed and constructed to facilitate the flow rate of EGW through the test apparatus as well as to aid in temperature control of the fluid. Figure 3 is an annotated photograph of the booster assembly. A 1/2 horsepower electric centrifugal pump was sized to handle the estimated pressure drop required to circulate the EGW through approximately 25 feet of 3/8 inch copper tubing as well as various fittings, and valves. The pump was installed on the EGW supply line and connected with copper union joints to make replacement or upgrading easier in the future. The pump was also mounted on an aluminum T-slot frame which was anchored to the ground and rested on four rubber vibration dampening feet. A flow switch was used as a safety precaution and would cut power to the booster pump in the event that the pump stalled or if there was an obstruction that caused the flow to slow or stop.

During standby and upon booster pump startup, the bypass valve was opened to allow all of the EGW to pass through the bypass loop. Once the pump started, the bypass valve was slowly closed to meter the pressure on the supply side. This pressure was monitored by a pressure gauge which allowed the operator to quickly see if the pressure was increasing excessively. The bypass valve was adjusted until a target volume flow rate was reached and confirmed by the flow meter transmitter. On the supply side of the flow loop, the tubing diameter was increased to a 1-1/2 inch sized pipe through a reducer fitting. This large diameter section was about 5 feet long and was wrapped with a flexible 576 watt resistance heater. The heater was further secured to the tubing surface by wrapping it with an insulated wire. This heater allowed the EGW to operate at a higher temperature than the temperature of the large wind tunnel's cooling coils which were also cooled by the supply ETW. This increased temperature allowed the entire T-block assembly to operate at a higher temperature which provided a wider variety of testing options.

After the heater section, the tubing was reduced to a 3/8 inch tubing and was then guided through the wall of the large wind tunnel and down to the test section. A check valve ensured that the flow direction was not reversed on this circuit and two ball valves on the inlet and outlet to the T-block assembly's cold plate were used to prevent any flow if needed. Two flexible braided tube fittings were used to connect directly to the copper tubing. These allowed the T-block assembly to be positioned without applying excessive force on the tubing and also helped to isolate the test section from any vibrations that could come from the copper tubing.

On the return side of the cold plate, copper tubing exited through the same port which the EGW entered in the wall of the large wind tunnel. EGW was passed through a Micro Motion Inc. mass flow sensor (CMFS010M319N2BAECZZ) to get an accurate reading on the amount of EGW passing through the T-block assembly. Specification of this sensor are described later in this

chapter. The EGW then recombined with the bypass flow and was recirculated back to the pump module.

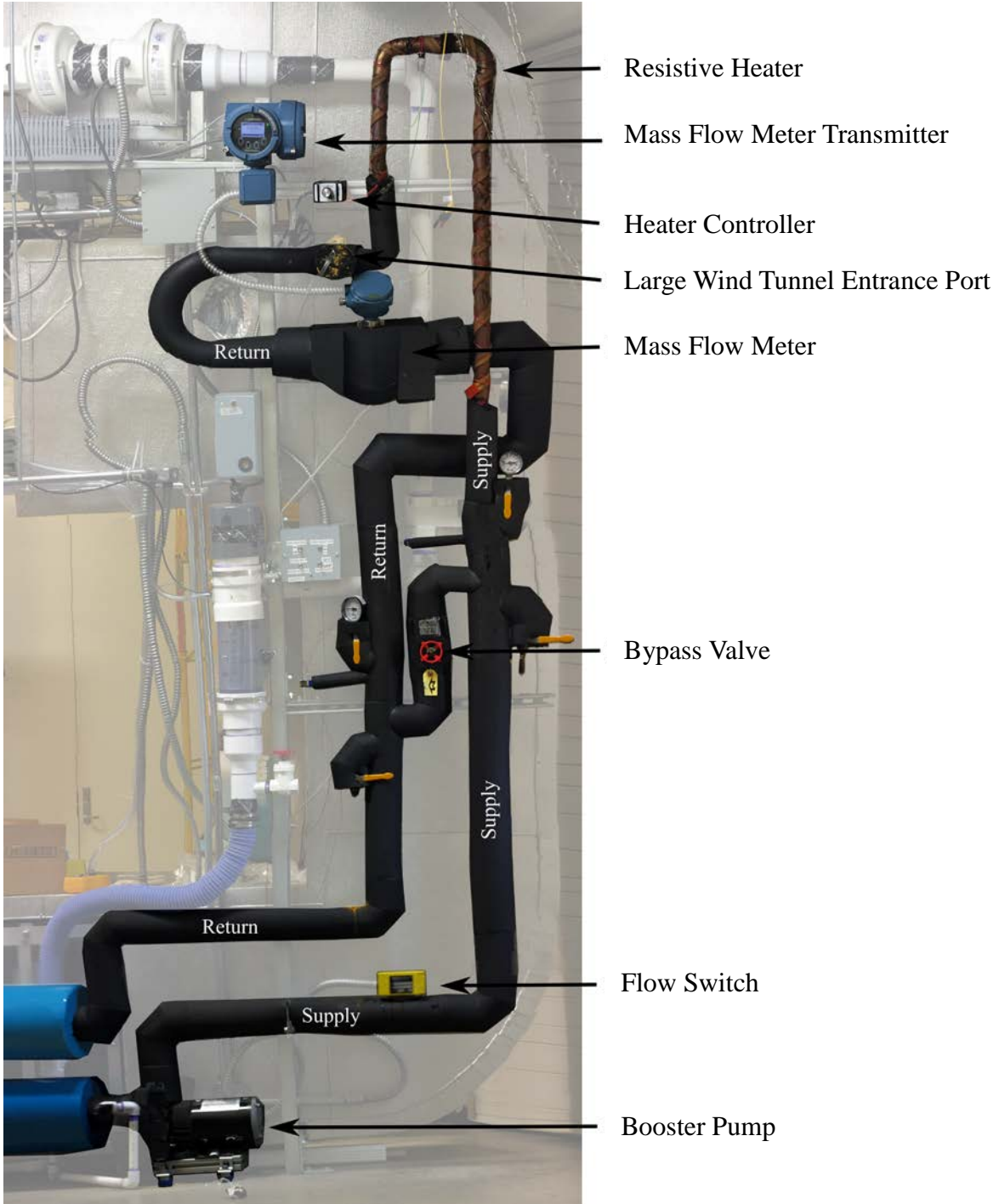


Figure 3: EGW booster assembly

4.2.2 Steam Humidifier

A Cenco Physics electric steam generator (Figure 4) was used to increase the relative humidity of the air at the inlet of the test section. Figure 1 shows the position of the humidifier with respect to the test apparatus. The generator included a large cap with two holes in it. One of the holes acted as the steam outlet and a rubber plug with stainless steel tubing inserted through it provided an airtight seal for the steam to travel through. The other hole was closed with a solid rubber plug. This hole provided access to the generator for refilling and for checking the water level. Once the water inside of the steam generator was heated, the generated steam traveled through the insulated stainless-steel tube, through the wall of the large wind tunnel, and to a steam wand/nozzle. The steam wand evenly distributed the vapor across the inlet of the test apparatus.

This steam generator had a maximum capacity of 1 L (0.26 gal) however to avoid liquid water from splashing and entering the tubing, approximately 500 mL (0.13 gal) was used. Any liquid water that did get into the tube, or any steam that condensed on the inside of the tube was collected in a water trap prior to entering the steam wand which prevented liquid water from being sprayed inside of the wind tunnel and on the test apparatus.

Ultra-purified type 1 deionized water was used to generate the steam. This ensured that very few contaminants would be introduced in the experiment and thus prevented contamination on the test plate surfaces. To prevent the steam from leaking before entering the stainless-steel tubing, a silicone sealant was used to fill gaps between the large cap and the steam generator's heated water vessel. This seal allowed sufficient steam pressure to build up and force steam through the stainless-steel outlet tubing. This seal was not perfectly leak tight however. This was intentional so that the pressure inside of the steam generator could not reach dangerous levels, and

if the pressure reached a high enough point, the large cap could be pushed open with relative ease.



Figure 4: Photo of steam generator

4.3 Test Apparatus

The test apparatus was essentially a subsonic open return wind tunnel (Figure 5 - 8). It was important that the test apparatus was contained inside the larger climate-controlled wind tunnel not only to maintain steady air conditions but also so that the temperature of the air inside the test apparatus was the same as the air flowing around the outside. With balanced temperatures on both sides of the test apparatus walls, there would be no heat transfer. This permits the adiabatic wall assumption to be made. The test apparatus can be subdivided into three subassemblies: Inlet converging duct, T-block assembly (test section), and the outlet duct.

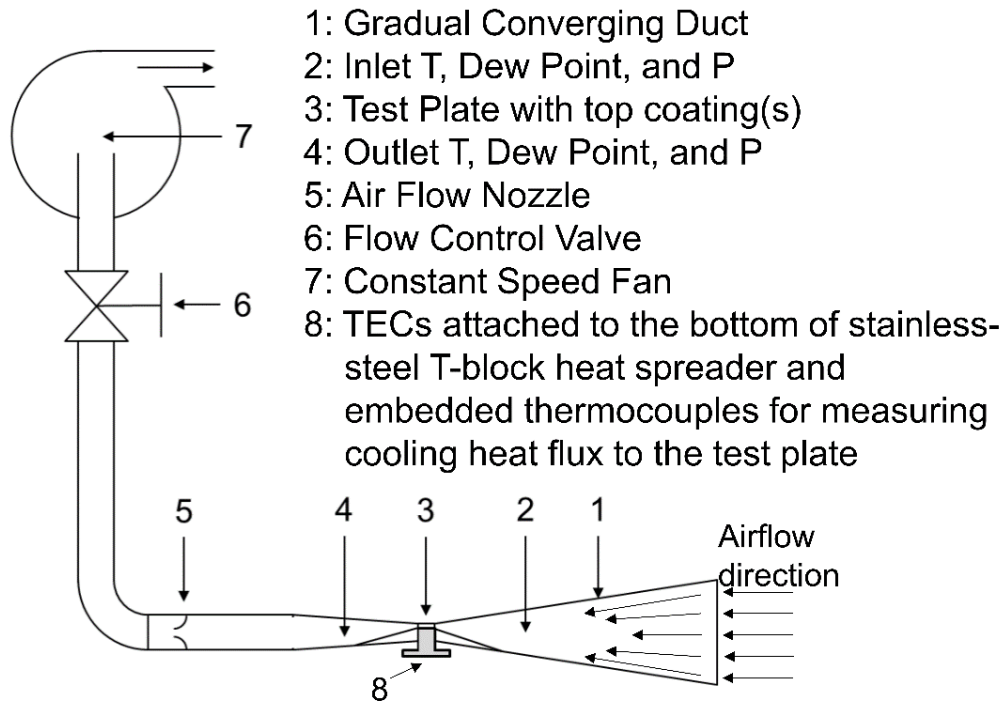


Figure 5: Schematic of main test apparatus

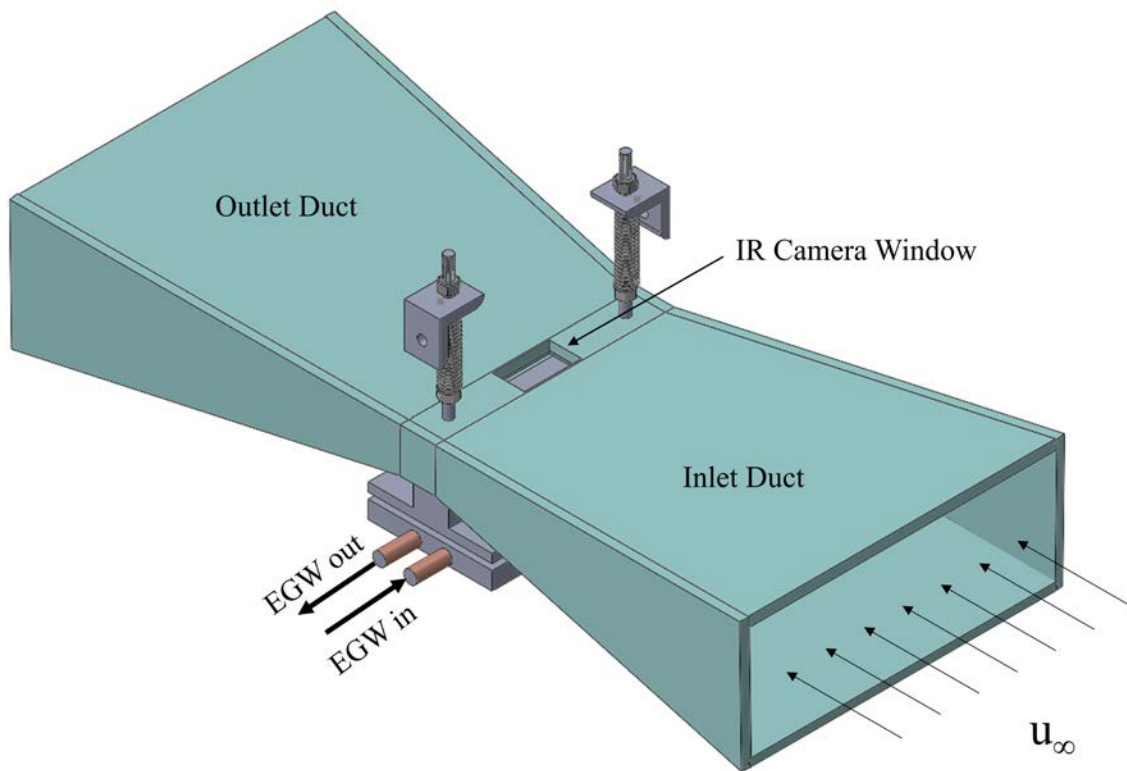


Figure 6: Isometric model of test apparatus

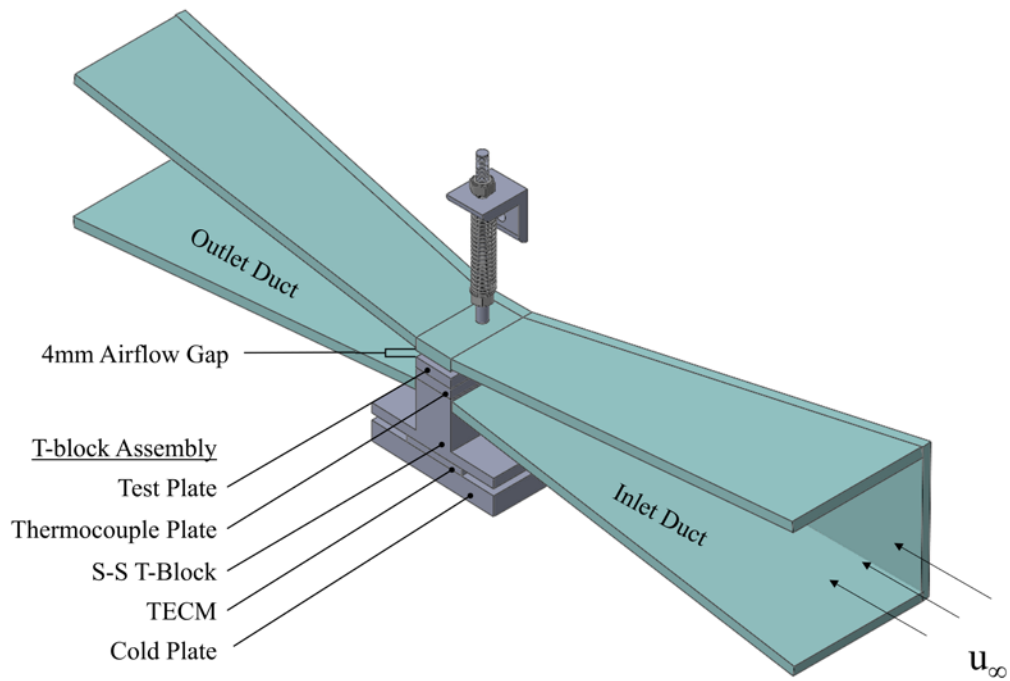


Figure 7: Isometric model of test apparatus (cross section)

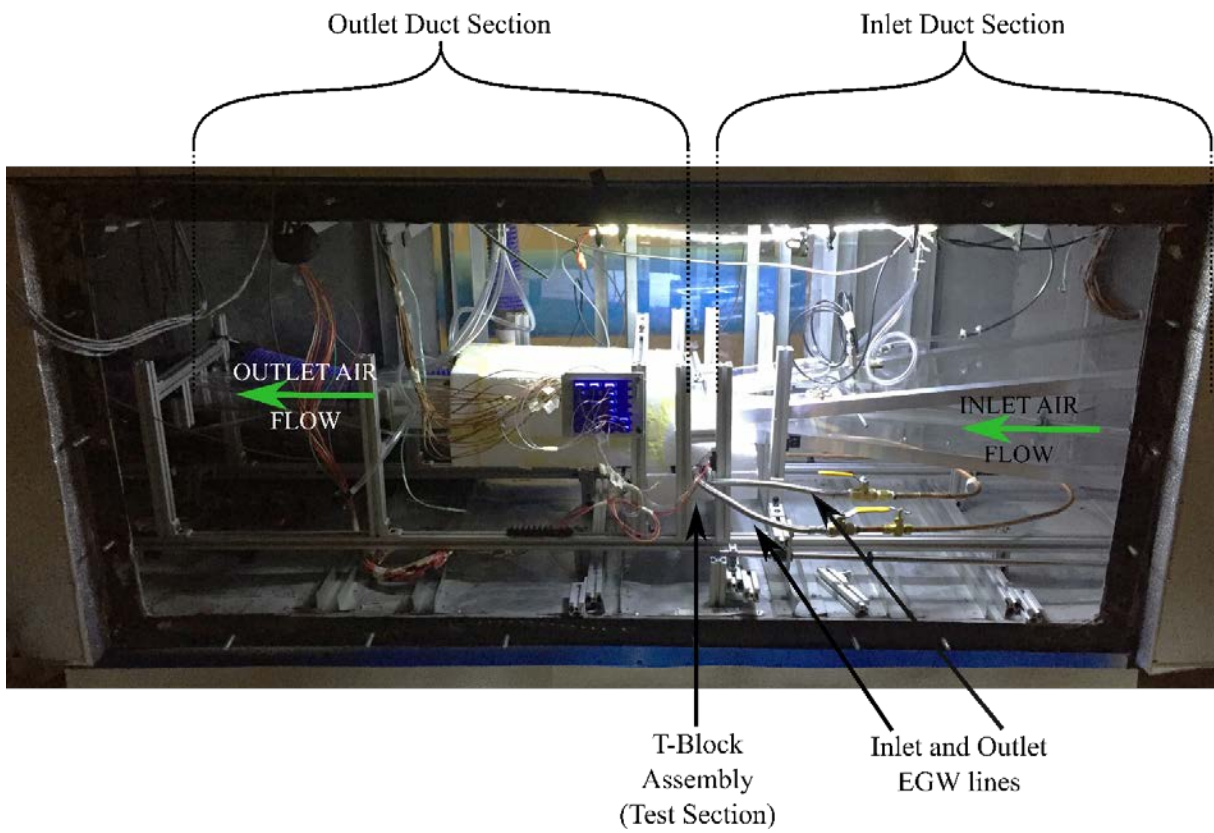


Figure 8: Picture of the test apparatus inside the large wind tunnel

4.3.1 Inlet duct



Figure 9: Inlet duct construction

The inlet duct directed air flow from the large closed return wind tunnel to the test section while maintaining smooth laminar flow (Figure 7) with a test section Reynolds number of approximately 1690 for duct flow. It also functioned as a guide for the videoscope to the test section. It was constructed from acrylic sheets with a wall angle of 7° and reinforced with aluminum angle. The entire test apparatus was supported by extruded aluminum t-slot framing. Silicone caulk was used to seal the corners and walls which helped to maintain both smooth and laminar flow. The most upstream portion of the duct, also the widest portion, was securely fixed in place inside of the large wind tunnel. The downstream and upstream portion of the duct were attached together with a PTFE-coated fiberglass fabric sheet with a 7 in. gap between the two sections of the duct. This allowed for the narrow duct section to slide back and forth on a set of stainless steel guide rails without breaking the seal. Once returned to the extended position, the fiberglass fabric would straighten allow smooth flow. The sliding action of the narrow section of the duct provided access to the test section to allow for the removal of test plates between experiments. The inlet duct also housed thermocouples for inlet air temperature measurements, an

air sampling probe to measure the inlet dew point temperature, and a pressure probe to measure inlet static pressure. The layout of these sensors is shown in Figure 8.

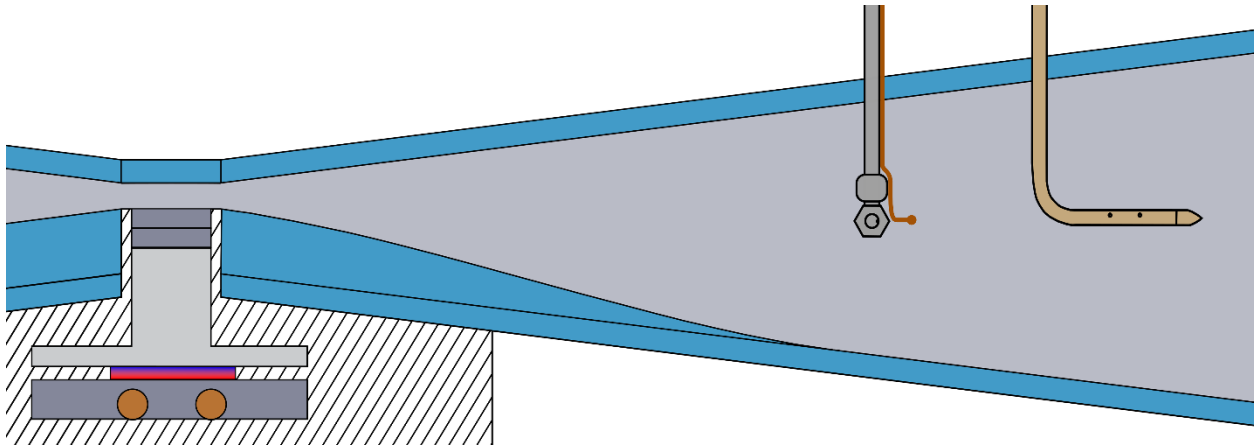


Figure 10: Inlet sensor layout

Air flowing from the inlet duct was directed into the test section where a test plate was mounted and maintained at a desired temperature. The test section was a small gap with dimensions of 6 inches wide, 4 mm tall, and 1 inch in depth. This thin gap was intended to mimic the gap between the fins in a heat exchanger. The upper bound of the test section was made from acrylic with a small viewing window made from a zinc selenide glass plate for viewing for an infrared camera. The far side edge was bounded by acrylic. The near side edge was bounded by a piece of clean borosilicate glass for viewing the test section from the side. The bottom of the test section was bounded by the test plate itself.

4.3.2 Test section assembly

The test plate was mounted on what was called the T-block assembly as shown in Figure 9. The T-block assembly is the device that facilitates the removal of heat from the surface of the test plate. The five major parts that make up the T-block assembly include a cold plate, two thermos-electric cooling modules (TECM), a stainless-steel T-block, a thermocouple embedded

aluminum plate, and the test plate. The cold plate has copper tubing embedded in it which allows chilled EGW to flow through it removing heat from the assembly. Six thermocouples were embedded into shallow grooves which were machined by a 1/16-inch end mill. These thermocouples were in place using aluminum based thermal epoxy. Two TECM were positioned directly above the thermocouples on the cold plate with the “hot” side of the TECM facing toward the cold plate. A silver based thermal grease was used to ensure good thermal contact with the cold plate. Similar to the cold plate, the stainless-steel T-block had six grooves machined into it and 6 thermocouples were secured in the grooves using aluminum based thermal epoxy. The T-block was positioned directly above the TECM so that the thermocouples would come into contact with the TECM. Silver based thermal grease was used again between the TECM and the T-block. Threaded nylon bolts were used to secure the T-block and the cold plate together and to ensure good contact with the TECM. Nylon was chosen as opposed to a metal bolt to prevent thermal bridging between the T-block and the cold plate. Additionally, Nylon is a flexible material and as the assembly cooled and warmed during testing, forces from the bolts were more stable and avoided putting an excessive load on the TECM which are quite brittle. The geometry of the T-block served two purposes. One, it evenly distributed the heat flux from the two TECM, and two, the heat flux was directed in the vertical direction through the test plate surface. By measuring the temperature from the bottom of the T-block to the thermocouple plate, the heat flux could be measured according to the methodology described in detailed in Cremaschi, et al., 2012.

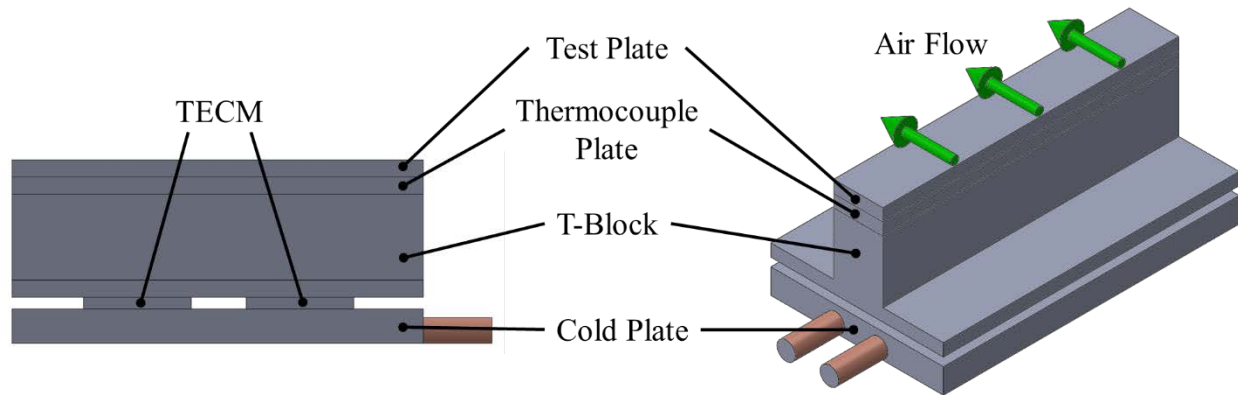


Figure 11: Schematic of T-block assembly (airflow indicated by arrows)

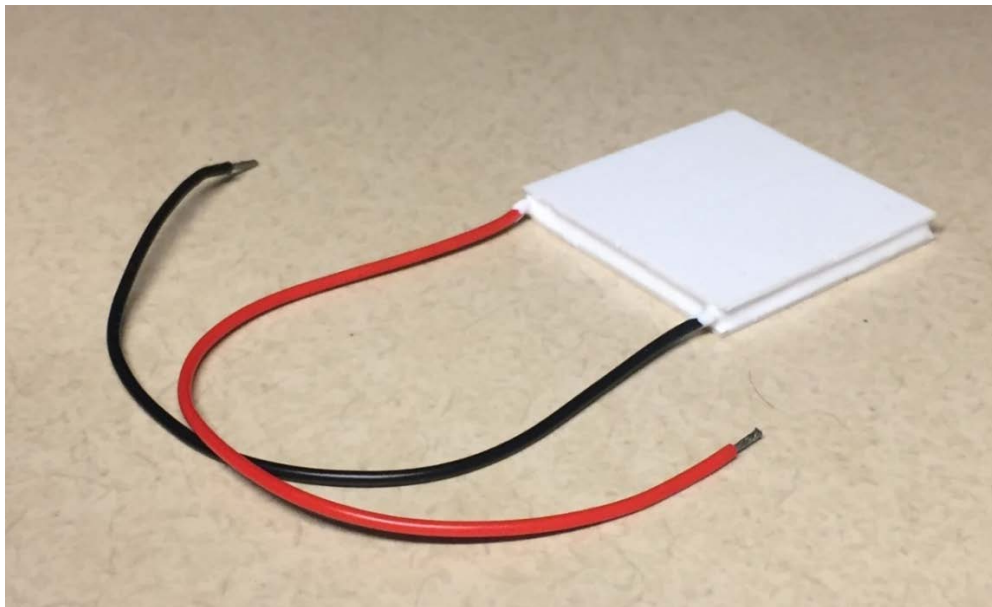


Figure 12: Photo of thermoelectric cooling module from Custom Thermoelectric (model # 19911-5L31-03CQ)

The two TECM were manufactured by Custom Thermoelectric (model # 19911-5L31-03CQ) and were rated for a maximum cooling load of 44 watts each. In ideal conditions. During testing the T-block assembly would only experience a thermal load of 4-6 watts of cooling depending on the test conditions. Two DC power supplies were used to manually adjust the power to the TECM. Two fuses were installed for each of the TECM for the rated limit of 3 amps. This proved to be very beneficial because any short or accidental surge could damage the modules

which would require the entire T-block assembly to be uninstalled and disassembled in order to replace the modules.

The T-block was designed and manufactured by Ehsan Moallem (2012) who used these T-blocks in his dissertation on coated surfaces of micro channel fin heat exchangers. Certain design aspects of his research inspired the design of the current study specifically in the design of the T-block assembly.

An aluminum thermocouple plate with four thermocouples embedded into one side, similar to the cold plate and bottom of the T-block, was attached to the top of the T-block using an aluminum thermal epoxy. Finally, the test plate was secured on top of the temperature plate by a custom clamping system to ensure good contact resistance and to help prevent movement of the test plate during and between experiments. A silver thermal grease compound was used in between the test plate and the underlying temperature plate to further ensure a good thermal contact.

4.3.3 Test plate clamping mechanism

The difficulty in designing a clamping system for the flat plate came from the need to press firmly on the top of the surface while keeping as much of that surface exposed so that it can grow frost unobstructed. The final design as shown in Figure 11 was a clamping system with two rods pressing near the edges of the test plate. The rods were secured to the rigid external structure through two brackets. Two equal sized springs were held in compression between the rigid bracket and the rod by a locknut. It was important that the position of the brackets and the lock nuts as well as the length of the rods were identical on both sides of the test plate to ensure even pressure. The rods were fabricated from a glass filled nylon rod. This material was chosen for its relatively high strength and relatively low conductivity. The rods were threaded using a die.

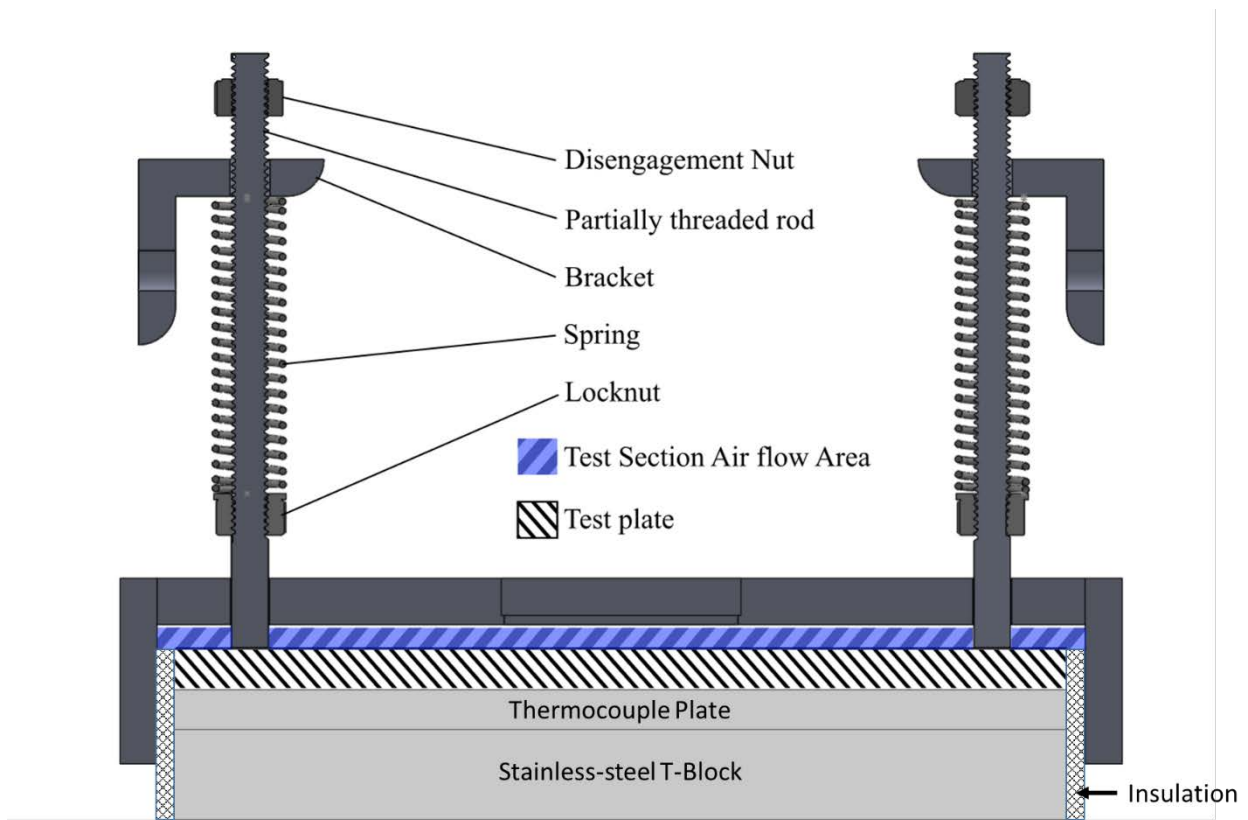


Figure 13: Cross section of test section and custom clamping system

Two disengagement nuts were located at the very top of the rod to enable the clamping mechanism to be disengaged. This was done by manually lifting the pins from the surface by compressing the springs further and then twisting the disengagement nuts until they came into contact with the top of the brackets. This prevented the springs from expanding and pushing the clamping rods back down onto the test surface.

This type of clamping system is beneficial because it is easy to engage, disengage, and it provides even symmetrical pressure on the test plate. Unfortunately, this setup requires that some of the surface be covered by the pins. This is not ideal however in order to maintain a secure and good contact for the test plate, some sacrifice of the frosting surface was unavoidable. During testing, most of the visual analysis of the droplets and frost layer were observed from the middle

sections of the test plate where the clamping rods have very little to no effect.

The entire T-block assembly was insulated with 2-inch thick polystyrene foam board and/or nitrile rubber foam insulation. With thermocouples at the base and top of the T-block, and knowing the conductivity of stainless-steel, the T-block could be used to measure the heat flux through the test plate.

The outlet duct performed two roles. One was to measure properties of the air after the test section. These properties included outlet air temperature, pressure, and dew point. Pressure differential across a flow nozzle was measured in order to calculate the flow rate. The second role was to control the flowrate of the air through the test section.

4.3.4 Test Section Airflow Handling

The test apparatus was designed to be able to test individual samples of a microchannel fin heat exchanger. Therefore, the inlet cone and outlet chamber were constructed to have a maximum air flow cross sectional area of 152 mm by 25 mm (6in by 1in). To conduct the flat plate experiments reported in this thesis, the original design was modified to create a 4mm (0.16in) gap for air to flow over the test plate. This required that a portion of the cone section to be positioned very closely to the T-block. Because of this, only a very thin layer of insulation could be used on either side of the T-block. To ensure smooth flow into and out of the test section as well as to improve the insulation in the upper portion of the T-block, two “air ramps” were constructed as shown in Figure 12 by item a and item b for the inlet ramp and outlet ramp respectively. These ramps were constructed by making a set of ribs connected together by spars and covered with a plastic film to create a smooth curved surface. The ribs and spars were designed in SolidWorks and were constructed from acrylic material. The plastic film coating used was Top Flight ® MonoKote high gloss polyester film which is commonly used to coat the wings of hobby remote

controlled aircraft. Because these air ramps were hollow, they prevented airflow from reaching either side of the thin insulation layer on the T-block directly. Instead only natural convection from the air inside of the ramps could transfer heat to the colder T-block reducing the heat loss.

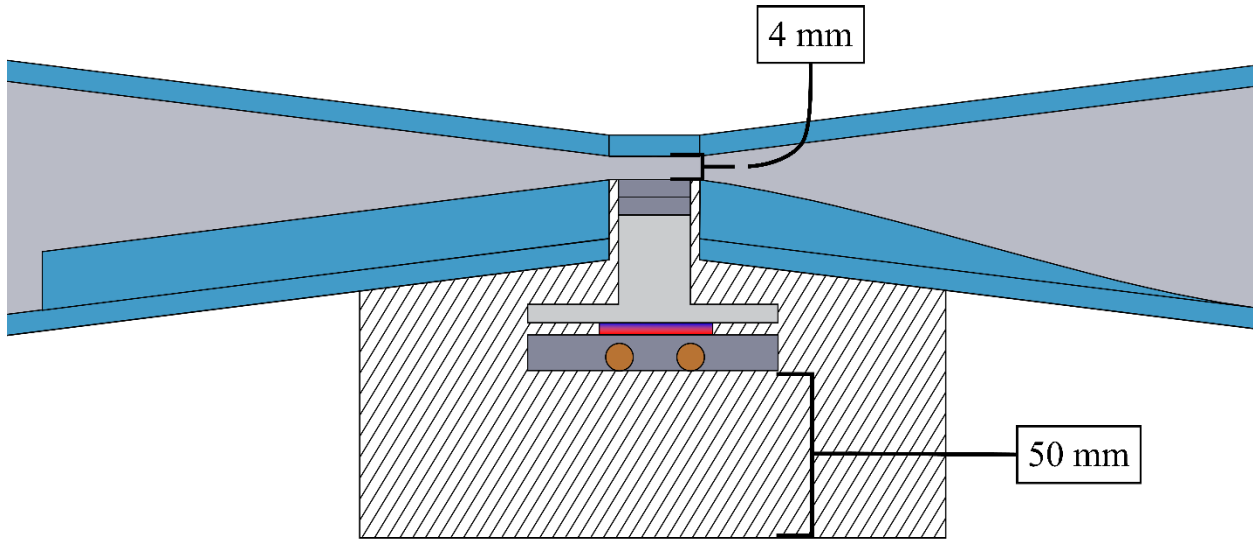


Figure 14: Test section where the coated surface is positioned

Although the T-block would ideally have the least heat gain possible, the primary purpose of the T-block was to evenly distribute the heat flux generated by the two thermoelectric modules in order to achieve an evenly distributed surface temperature. Nonetheless, this heat gain was measured and accounted for in our analysis by a steady state calibration test discussed later in this thesis.

4.3.5 Outlet Airflow Handling

After the outlet nozzle, the exhaust air was transported through semi-flexible tubing to two centrifugal blowers. These blowers were the primary source of pressure differential for the airflow through the test section. The blowers would then move the exhaust air through more flexible tubing and blown into the tower section of the recirculating wind tunnel just before the blower through

acrylic access paneling. This location was chosen because the paneling could easily be patched or replaced in the future. Additionally, because this location of the tower had a lower air pressure than at the test section, the air would flow through the test section at a low flow rate without power to the centrifugal fans. This was beneficial when the system was set to standby conditions so the air in the test section would not remain stagnant for a long period and also because the two blowers would not have to operate for very long periods of time thus extending the lifespan of the components. Figure 1 shows this test apparatus air flow path.

Originally the two outlet centrifugal blowers were to be located inside of the recirculating wind tunnel but in the final design they were positioned outside. The reason for this was partly for ease of manufacturing and maintenance, but there was also a concern that the blowers may malfunction if we were to test in below freezing air temperatures in the future. Additionally, a small air heater box was constructed to prevent damage that could be caused by the cold airflow on the fan components and also to prevent condensation from forming on the outlet air ducts.

The outlet flexible tubing was clamped to a 3" PVC size tube which was connected to a series of adapters to reach a final PVC tube diameter of 6". The heating chamber was made from a 6" clear PVC tube. A small radiant heater unit was installed inside of this tube section. The heater was rated to output 100 watts of radiant energy and had a mechanical thermostat controller built in to prevent itself from overheating. As an added layer of safety, a resettable temperature disk switch was wired in series with the heater and the sensor was installed in a hole drilled into the wall of the tube adjacent to the heater coils. In the event of a failure in the thermostat, the temperature disk switch would trip and require a manual reset for the heater to restart.

4.4 Sensor Instrumentation

Many instruments were used to observe and measure various parameters of the experiment

in real time including temperatures, pressures, velocities, flow rates, and dimensions. All of the measurements were taken using a Nation Instruments™ data logging acquisition system (DAQ) and an in-house newly developed LabVIEW™ program sampled the data every 2 seconds, calculated derived quantities, plotted the data in real time, and controlled the test facility (Figure 13).

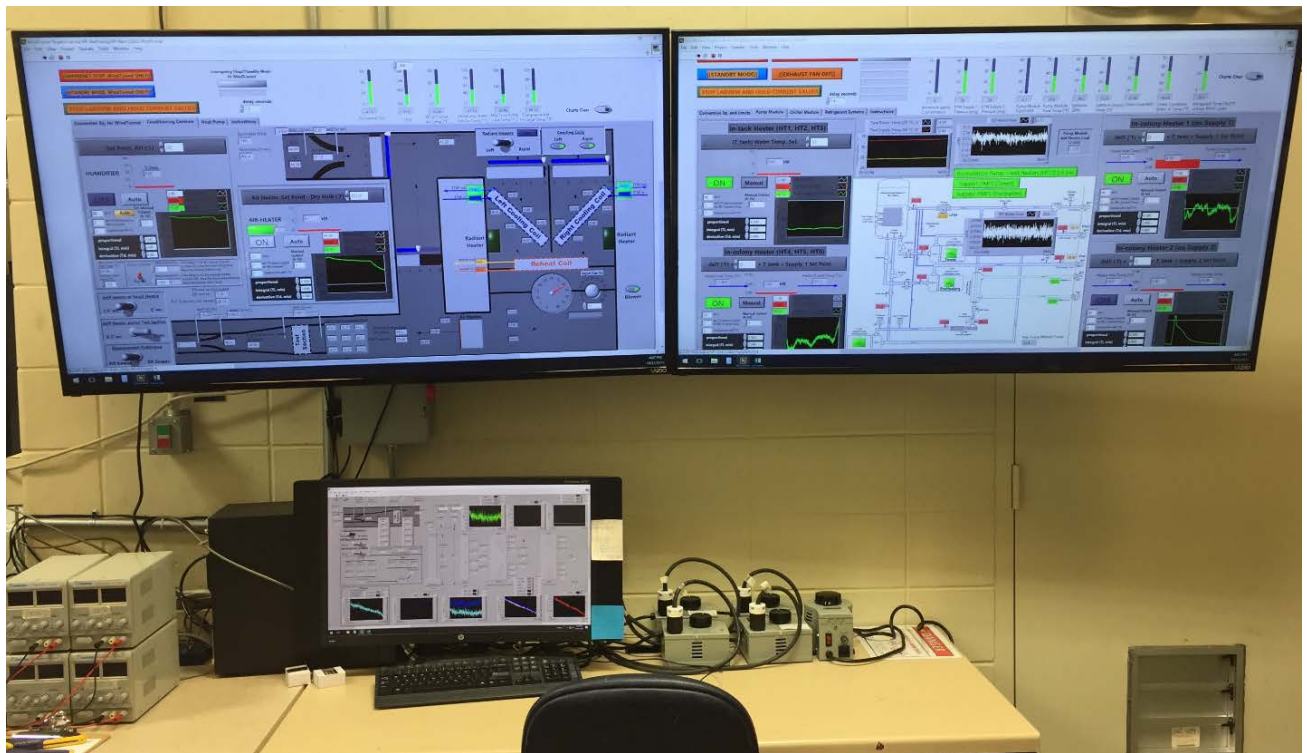


Figure 15: LabVIEW data acquisition and computer control system

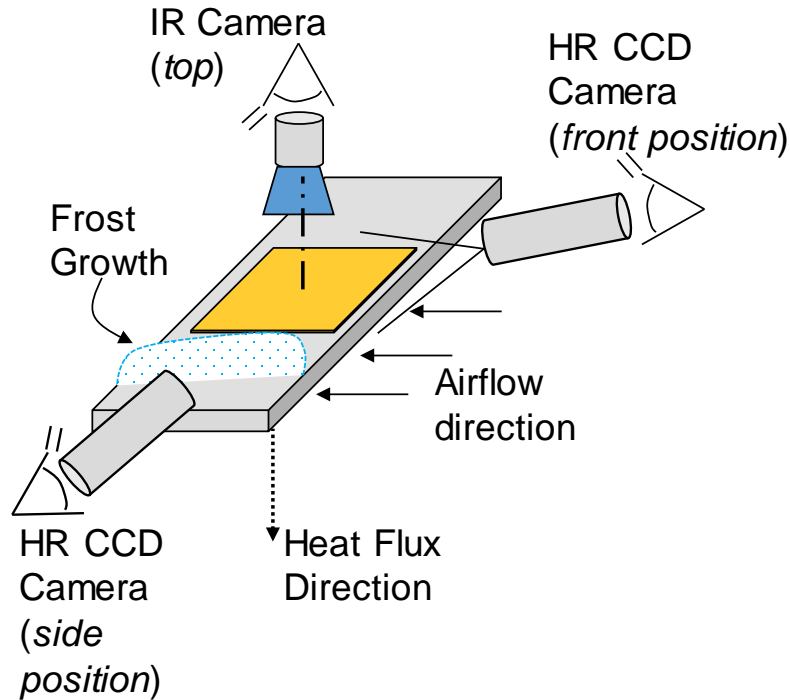


Figure 16: Illustration of the frost visualization sensors (HR CCD camera and IR camera) with respect to the test plate.

An infrared (IR) camera was positioned at the top of the plate and a High Resolution Charged Couple Device (HR CCD) camera was located at the front or, in repeated tests, at the side of the test plate, as shown in Figure 14. The IR camera measured the temperature of the frost surface and droplets size during freezing, while the HR CCD camera measured droplet size right after freezing and subsequent frost thickness. Sensors of the test apparatus measured the time dependent heat flux, surface temperature, air dry bulb and dew point temperatures at the inlet and outlet of the test plates, airflow rate, and air static pressure and air pressure drop across the channel of the test plate. Figure 15 shows the layout and positions of sensors in the airflow path of the test apparatus. Main derivative quantities were mass of frost, frost density, and the time dependent airside convective heat transfer coefficient. Table 1 lists the accuracy specifications for certain system parameters

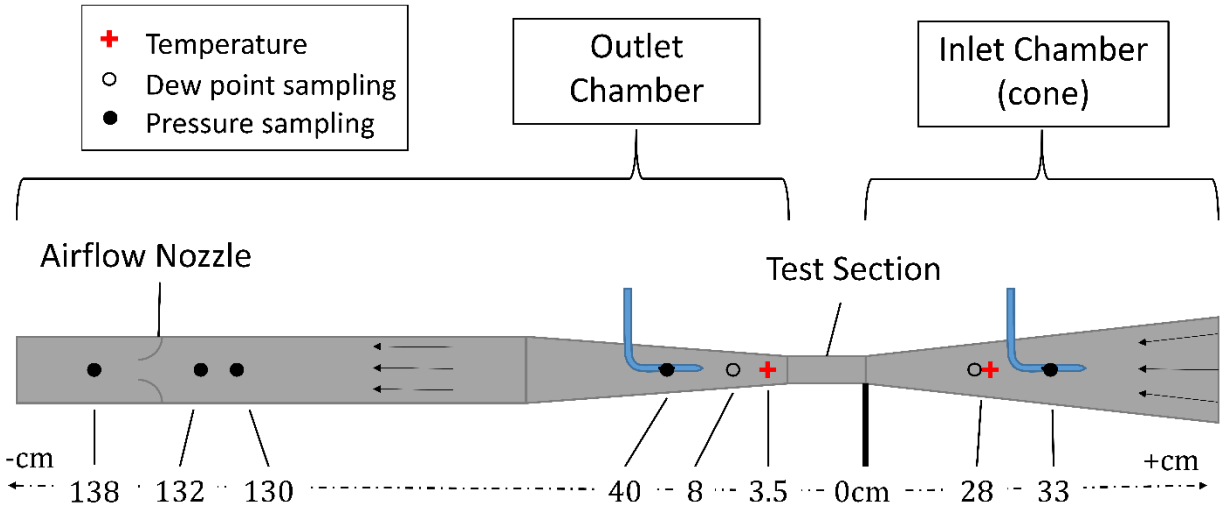


Figure 17: Diagram of test apparatus with sensor positions and their distance to the leading edge of the test section

Table 1: Measurement devices, set points, ranges, accuracies, and control tolerances

Parameter Measured	Measuring Device	Calibration	Set Point/Range	Accuracy	Control Tolerance
<i>Sensors for controlled variables</i>					
Air Temp. (dry bulb)	Thermocouple (grid)	In situ*	5°C (41°F)	±0.056°C (±0.1°F)	±0.28°C (±0.5°F)
Air Temp. (dew point)	Chilled Mirror Dew Point Meter	Manufacturer	0.56°C (~33°F)	±0.28°C (±0.5°F)	±0.28°C (±0.5°F)
Plate Temperature	Thermocouple (grid)	In situ*	-15°C (~5°F)	±0.04°C (±0.07°F)	±0.28°C (±0.5°F)
Air Volume Flow Rate	Flow Nozzle	Manufacturer	8.5 m ³ /h (~5 cfm)	±0.05 m ³ /h (±0.03 cfm)	±0.09 m ³ /h (±0.05 cfm)
<i>Measured Variables</i>					
Air Pressure Drop	Pressure Transducer	Manufacturer	0 to 250 Pa (0 to 1" H ₂ O)	0.25% full scale	(-)
Frost Surface Temperature	Infrared Camera	In situ	-22°C to 5°C (-8°F to 41°F)	±2°C (±3.6°F)	±1.6°C (±3.5°F)
Frost Mass	High Precision Digital Scale	Manufacturer	0 to 5 g (0.011 lbm)	±0.1 mg (±0.0015 gr)	(-)
Frost Thickness	CCD Camera	In-situ	0.2 to 3 mm	±80 μm @ 0.4 mm ±40 μm @ above 1 mm	(-)
Heat Transfer Rate	T-Block Assembly	In situ*	5 to 8 W (17 to 27.3 Btu/hr)	15%	(-)

*Temperature bath and temperature sensor with accuracy of ±0.05°C (±0.1°F) were used for in-site calibration.

4.4.1 Temperature probes

Two primary types of temperature sensors used were thermocouples and resistance temperature detectors (RTD). Two RTD probes were used to measure the sampled air of the inlet and outlet dew point sensors. These probes were provided by the dew point sensor device manufacturer. All other temperature sensors in the test apparatus were t-type thermocouples and were either welded or manufactured. Welded thermocouple wires were welded and calibrated in house. Fine gauge thermocouples were used to measure the temperature on both sides of the TECM and in the thermocouple plate of the T-block assembly. A thicker gauge thermocouple wire was used to measure air temperature at the inlet and outlet of the test section. Welded thermocouples were used in a 3x3 mesh pattern to measure air temperature after the flow straightener in the large wind tunnel and also upwind and downwind to the large cooling coils of the large wind tunnel. T-type thermocouple probes manufactured by Omega were used to measure temperature in the pressurized EGW tubing at various points of the facility notably at supply and return of the EGW booster assembly.

4.4.2 IR Camera

To measure the droplet diameter at the moment of and before freezing as well as to measure the surface temperature, an infrared (IR) camera was used. The FLIR T1030sc was chosen for its high resolution and ability to measure temperatures as low as -40°C (-40°F) a macro lens was used to achieve a “close-up” image of the droplets. Because of the short focal length of the lens, the camera was able to be installed inside of the wind tunnel without relying on a mirror or window in the wall of the large wind tunnel. The camera was attached to the structural frame of the test apparatus with aluminum extruded T-struts. When a new test plate was installed or the camera’s position was adjusted, a calibration image was captured. This was simply an image of a flat object

with a known shape and dimension. An American one cent penny was used as a scale reference with a known diameter of 19.05 mm (0.75 in). It was important that the camera did not move once the camera was in position and the calibration image was taken otherwise the measurements from the IR camera would not have been accurate.

The test plate was enclosed by acrylic. Because acrylic is not transparent to infrared light, a window was cut out over the center of the test plate and a small zinc selenide glass window was installed and glued in position. Zinc selenide was chosen for its optically transparent quality in the infrared range of the electromagnetic spectrum. This glass allowed for the IR camera to capture a clear image of the test plate surface without drastically affecting the geometry of the test section. Figure 16 shows three samples (acrylic, borosilicate, and zinc selenide) partially covering a gloved finger. Both the acrylic sheet and the borosilicate glass materials are opaque to infrared light and thus the outline of the finger covered by the materials is not visible. The zinc selenide glass however allows the outline of the gloved finger to be seen through it quite clearly.

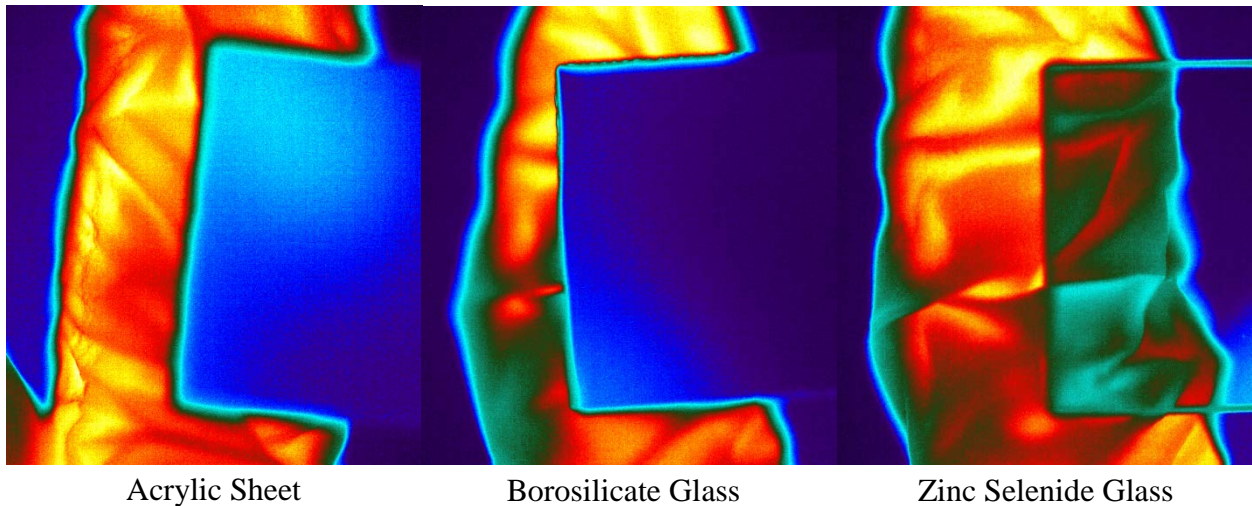


Figure 18: Representation of optically translucent quality of zinc selenide in the infrared spectrum compared to the optically opaque quality of acrylic and borosilicate glass

4.4.3 Videoscope

To capture images of the frost thickness from the front and sides of the test section, an industrial high definition endoscopic CCD (charged coupled device) camera was used (Figure 14). Specifically the Olympus IPLEX NX model IV9000N and the 6mm insertion tube was selected. This device will be referred to as the videoscope in this thesis. The videoscope is comprised of two parts; the main unit which processes, records, and displays the footage, and the scope unit which facilitates the insertion tube and the camera optics. The main unit was positioned outside of the wind tunnel and the insertion tube was inserted through a plastic tubing guide which guided the endoscope into the wind tunnel, through the inlet cone, and to an upstream position of the test plate. For some tests, the videoscope was positioned to the side of the test section to take side-view pictures of the frost layer. This was done in a similar manner with a plastic guide tube.

One concern about the videoscope is that it may cause a disturbance in the airflow large enough to effect the experiment. Tests were conducted with the videoscope positioned at varying angles and distances from the leading edge of the test plate and the effects on the frost were observed. It was found that if the videoscope was positioned too closely, streaks in the frost growth could be seen due to a disturbance in the airflow. It was also found that if the videoscope was positioned greater than approximately 2 cm away from the leading edge, this streaking effect would disappear.

The IPLEX NX has an integrated light source which the processor modulates automatically. This automatic brightness feature is convenient for recording the bright white frost, however it is not suitable for capturing clear images of the liquid water droplets before freezing occurs. The problem arises from the bottom surface of the cone closest to the test plate being made from a white film plastic. When the camera sees the bright white film, the processor automatically

dims the light to balance the overall image brightness and avoid overexposure. Even at the highest brightness setting, the test plate and subsequently the clear liquid water droplets are practically impossible to see. The manual brightness setting was turned on and the brightness was increased until the droplets could be seen clearly. As a result, the rest of the image became overexposed which was not a problem. The only drawback to this solution is that once the droplets froze, the bright manual light setting would also overexpose the now white ice. Because of this the experimenter was required to observe the droplets closely until the moment freezing occurred at which point the brightness would be either returned to the automatic setting or decreased to a level that the frost was clear and measurable.

4.4.4 Dew Point Sensor

Two dew point temperature sensors sampled air in positions upstream and downstream to the test section. The measured values from these sensors were used to calculate relative humidity, water content of the sampled air, and ultimately the mass of water that was deposited onto the test plate. The dew point sensors also helped in understanding the difference between the sensible and latent heat transfer rates through the test plate surface.

The Michell Instruments S8000 Remote Chilled Mirror Hygrometer was selected for that reason. This chilled mirror hygrometer is referred to as the dew point sensor in this thesis. To function, a sample of air from the area of interest was extracted and pumped across the chilled mirror sensor. A custom made sampling tee was constructed to sample air from various points across the width of the inlet and outlet ducts of the test section. Evenly spaced holes were drilled into 1/4" aluminum tubing into which sampled air flowed. Aluminum was selected for its machinability. The aluminum sampling wands were attached to a stainless steel fitting which directed the sampled air out of the wind tunnel through stainless steel tubing. The sampled air

flowed into an air flow regulator. From there the air entered the sensor housing and flowed across the chilled mirror sensor. The air then exited the sensor housing and traveled through flexible PVC tubing to the air pump. The air sampled from the inlet was pumped back into the wind tunnel but not the test apparatus. The air sampled from the outlet sampling wand was pumped back into the outlet chamber of the test apparatus so that the exact mass of the airflow over the test plate could be properly measured at the outlet nozzle. At the sensor, the temperature of a chilled gold plated mirror was decreased until water condensed on the surface as sampled air passed over the mirror. An optical light source and sensor above the mirror would measure the light reflected off of the mirror to determine when condensation occurred. A sensor control unit modulated the chilled mirror temperature and measured the exact temperature at which condensation occurred. This temperature was the dew point temperature of the sampled air.

The S800 sensor has an uncertainty of $\pm 0.25^{\circ}\text{C}$ in the temperature range for which it was used. Although this value seems quite large when compared to other simple temperature measurements in the experiment, this is actually quite an accurate dew point sensor due the nature and difficulty of measuring the dew point. To ensure that the dew point sensor was as reliable as possible, extra precautions in the design and operation of the device was taken.

In the design of the experiment, we chose to use stainless steel tubing to deliver the sampled air from the sampling point to the sensor because the steel tubing would not retain any moisture thus effecting an accurate dew point measurement. The sampled air traveled through approximately 4 m (13 ft) of 6.4 mm (0.25 in.) diameter stainless steel tubing. After the air was measured at the sensor, flexible PVC 13 mm (0.5 in) tubing was used to deliver the air to the dew point air pumps as well as to return the sampled air back into the wind tunnel. The sampled air

traveled approximately the same distance as it did through the stainless-steel tubing. Flexible PVC tubing was selected because of it was easy to construct and was easy to replace if needed.

In the operation of the experiment, prior to the start of each test, both sensor devices were turned on and the dew point was measured. The difference between both inlet and outlet dew point temperatures was verified to be less than 0.1°C which is less than half of the uncertainty range of each of the sensors. If the difference was greater than this amount, the sensors were cleaned per the manufacturer's instructions and then re-measured until both sensors agreed.

4.4.5 Pressure Transducer

Air Pressure measurements enabled the pressure drop and the flow rate of air across the test section to be calculated. Figure 17 shows the layout of the test apparatus and the positions at which pressure measurements are made.

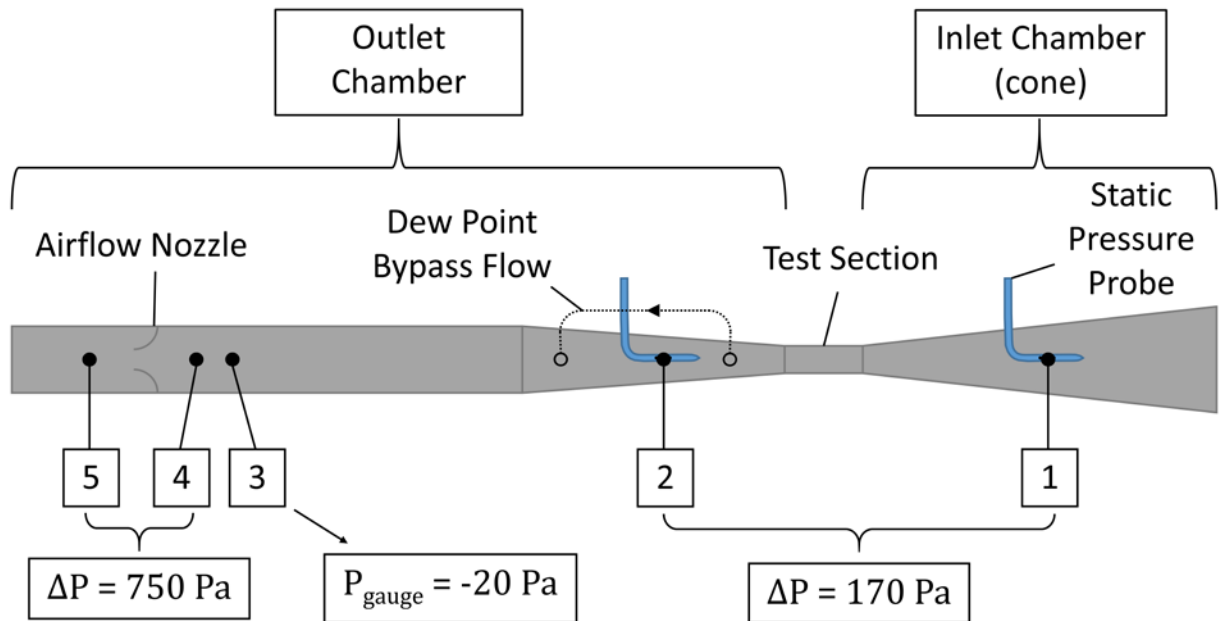


Figure 19: Pressure measurement locations

Two L-shaped static pressure probes shown in position 1 and 2 were connected to a

differential pressure transducer which measured the pressure drop across the test section. This difference would increase as the frost in the test section blocked the area through which air flowed which would increase the pressure drop. This pressure difference exemplifies the motivation behind this field of research as a whole. Preventing or delaying an increase in pressure drop across a heat exchanger is the primary objective of implementing surface coatings. Therefore it is important that these measurements are accurate and thus why these high quality L-shaped static pressure probes were used.

Figure 17 also shows an airflow nozzle in the outlet section of the test apparatus. The static pressure from four points (top, bottom, left and right) were sampled and averaged by directly connecting all four points together into one pressure tube. This arrangement of pressure sampling was used at position 4 and 5. Similar to the test section, the pressure difference across the air flow nozzle was measured. By taking a difference between point 4 and 5. Because the geometry of the flow nozzle did not change, unlike the airflow area of the test section, an accurate airflow rate through the nozzle could be accurately calculated. As previously explained, the outlet dew point sampling probe extracts a sample of air from the outlet chamber, but the dew point pump then injects that same air back into the outlet chamber slightly after the sampling point. This results in a net zero air mass loss from the outlet chamber. Because of this, we are able to assume that the air mass flow rate through the flow nozzle is identical to the air mass flow rate through the test section. Therefore from the mass flow rate of air, we are able to calculate an air velocity over the test section. The static pressure was additionally measured at position 3 for the purpose of confirming the pressure at position 4. The outlet nozzle and pressure sampling points can be seen in Figure 18.

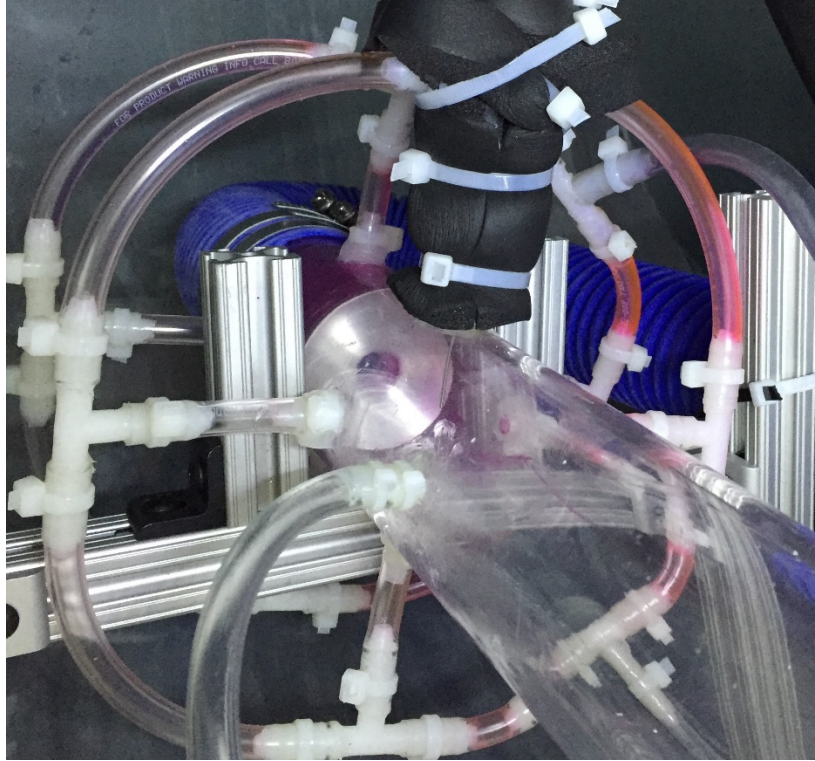


Figure 20: Outlet nozzle and pressure sampling nodes

Chapter 5: Experimental Procedure

5.1 Introduction

Three types of tests were developed over the course of this thesis. They were the pull-down test, constant surface temperature test, and the cycling test. The pull-down test was the simplest of the three. In it the surface temperature was decreased gradually from ambient temperature to a desired subfreezing temperature while moisture condensed on the surface. The constant surface temperature test implemented a dehumidifying nitrogen displacement technique to allow the surface to reach a target temperature before moisture was allowed to condense. The cycling test was a simulation of the freezing and defrost cycle experienced by typical heat exchangers in a heat pump system.

5.2 Achieving the test condition

During the frosting experiments, the plate top surface temperature was at -3.3°C (26°F), the air was at 5°C (41°F) dry bulb temperature, and 75% R.H. Since the air flow rate was constant, the air velocity increased from 3.8 m/s (~ 750 fpm) at the initial surface dry conditions, up to 19 m/s ($\sim 3,740$ fpm) for some tests with severe blockage of the free flow cross sectional area. The air flow rate was maintained at a constant mass flow rate by manually adjusting a valve in the outlet air flow tubing. This value was maintained within 1% of the target air flow rate during the tests. The air flow in the channel located at the top of the plate was turbulent with Reynolds number estimated to range from 6,000 up to 35,000 due to the frost accumulated on the plate (refer to section 7.3 in this thesis). All tests were conducted with the test plate initially in dry conditions,

which were defined as the conditions obtained after overnight exposure of the test plate to air circulating in the wind tunnel above 5°C (41°F).

5.3 Constant surface temperature test procedure

The constant surface temperature test was used primarily used because the data collected was more easily analyzed and conclusions more easily drawn. A nitrogen displacement technique was used to limit the variation of the surface temperature during the first few minutes of the test. Figure 19 and Figure 20 show the stages of a typical frost growth experiment. In phase I, the air temperature and humidity were steady state, there was no cooling and the plate was in thermal equilibrium with the surrounding air. In phase II the air flow was cut off and the plenum above the test plate was isolated. Nitrogen gas was slowly and gradually metered right above the test plate. The nitrogen displaced the air and the dew point temperature reduced to ultra-low levels as low as -30°C. The Nitrogen gas provided a blanket barrier for vapor intrusion to the test plate during the pull-down phase, that is, during phase 3 shown in Figure 19. The thermoelectric modules were energized and the plate surface temperature decreased close to the set point. During this phase III, because of the nitrogen blanket layer established on the top of the test plate surface, the dew point temperature was well below the surface temperature. Thus, condensation on the cold surface did not occur. The videos from the IR camera and the HR CCD camera confirmed that condensation was not visible.

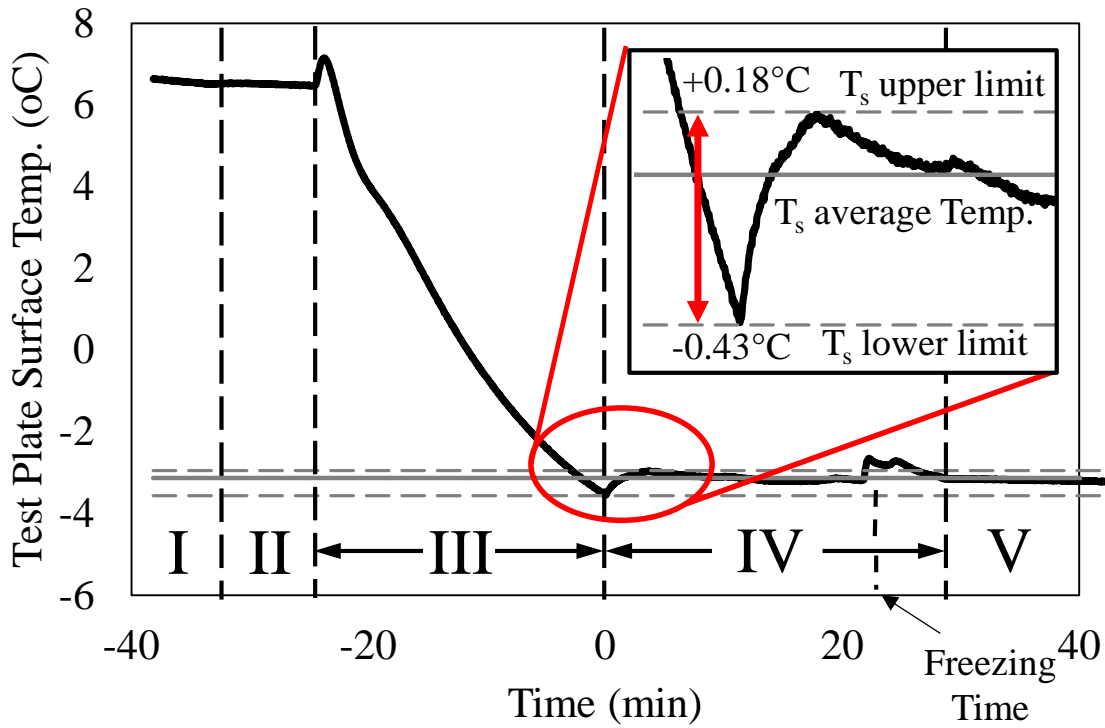


Figure 21: Test plate surface temperature vs. time during entire a typical frost test

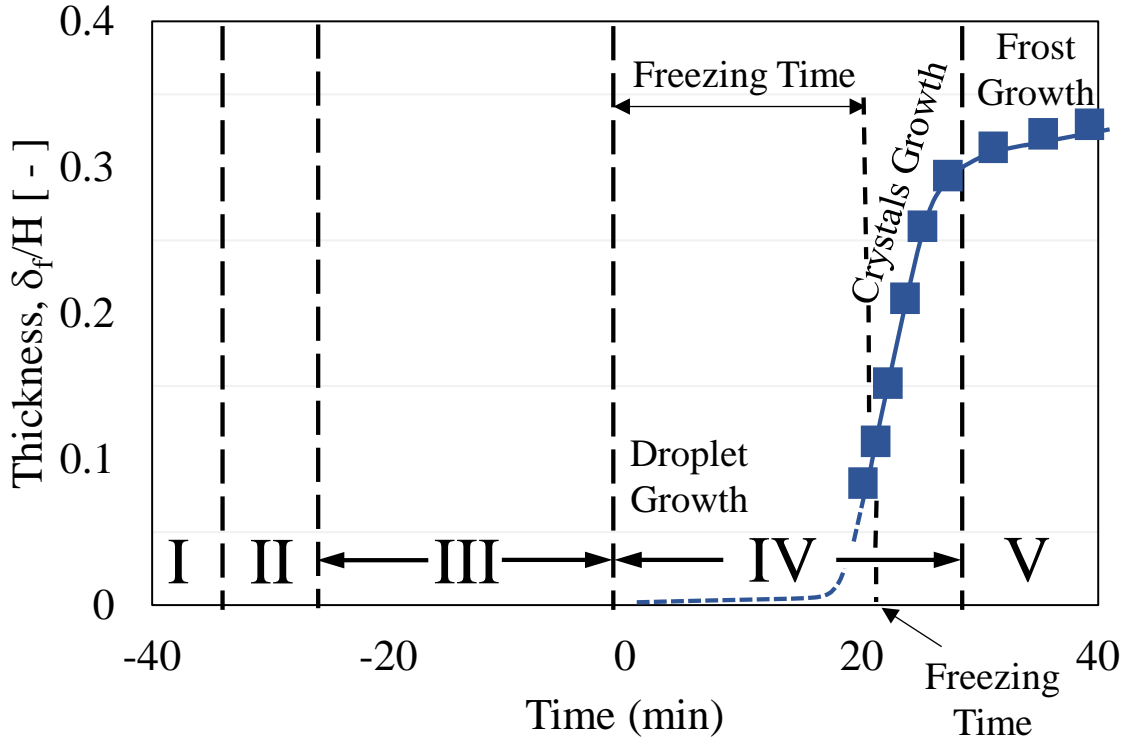


Figure 22: Thickness profile vs. time during the entirety of a typical frost test (square points are the measured thickness from the HR CCD camera)

When the test plate temperature reached slightly below the set point, the nitrogen gas flow was stopped, and the air flow was reopened to the top surface of the test plate. This time, indicated on the x-axis with 0 minutes in Figure 20, marked the starting period of water vapor condensation on the test plate. In phase IV, water vapor condensed on the test plate surface and droplets gradually grew. The freezing was observed by a slight increase of the surface temperature toward the end of phase IV. This was due to release of latent heat of solidification during the phase change process. At the same time, the HR CCD camera detected the ice beads thickness with crystals on their top. In phase V, the droplets appeared as complete ice beads with many crystals on their top, and the first frost appeared to form on the top of the ice crystals. This is the beginning of the frost growth stage, which many studies in the literature investigated. The focus of this thesis is to provide data during phase IV. Unique aspects of the test methodology were that (i) the surface temperature was constant during droplet growth, crystal growth, and frost growth stages; and (ii) the freezing time and freezing period were clearly identified from the start of condensation. To maintain a constant flow rate as the frost thickness increased to block the test section flow path area, a valve was manually adjusted to increase the pressure drop across the test section to stay within 1% tolerance of the desired flow rate.

5.3.1 Manual frost mass measurement procedure

Accumulated frost mass was measured using two methods. The primary method was to measure the difference in air water content across the test section over time with the dew point sensors. The secondary method was to physically remove the test plate at the end of a test and measure the frost mass using a scale. For the purpose of analysis, the air water content differential was used because the mass could be analyzed for any point during the test. The manual mass measurement method only aided in verifying the primary measurement.

For a test where the manual frost would be measured, a test was conducted as normal however the experiment was allowed accumulate condensate mass for three hours instead of the typical one hour. This was done so that a large amount of frost mass could accumulate. In doing so the percent error from the measurement procedure would be less significant than if a small mass was measured.

After 3 hours of frost growth, the TECM were turned off and the inlet cone duct was retracted to the open position allowing access to the test plate. While wearing gloves, a lint free cotton cloth was placed under the surface to catch it and any flakes of frost that may have fallen off as the test plate was removed. The two compression pins were lifted and locked in the up position by the two disengagement nuts. With the surface unclamped, a small hook tool was used to shear the thermal grease layer and remove the test plate. This tool was very important as it could apply a counter force on the underlying temperature plate directly which helped to avoid putting any unnecessary force which could delaminate the temperature plate from the underlying T-block. Once the test plate came loose, it was placed on and then wrapped by the cotton cloth, any flakes of frost may have fallen off during the removal process were also collected onto the cotton cloth.

The wrapped plate was quickly weighed on the A&D HR250AZ analytical balance along with two clean gloves. A heat gun was turned on and set to a temperature low enough to place one's hand directly in the output airflow without discomfort. The two clean gloves were put on and the wrapped test plate was picked up. Using the heat gun, the frost on the surface was melted and any moisture was evaporated from the test plate and the now wet cotton cloth. Once the test plate was visibly dry and the cloth became tactilely dry and stiffened, the test plate was again wrapped in the same cotton cloth and placed on the scale. The two gloves were also removed being certain that no visible moisture was on the inside of the gloves and weighed altogether with the

wrapped test plate. Moisture on the inside of the glove can be avoided by wearing two layers of gloves. The two clean gloves were measured with the test plate before and after the frost removal because while handling the frost late in the drying process, thermal grease remaining on the test plate would stick to the gloves and affect the total mass of the plate. Finally, the difference in mass was calculated and recorded. This measurement was compared to the deposited mass from the air water content differential calculation based on the dew point sensor measurements. An example of one test had a calculated frost mass of 4.26 grams whereas the manually measured mass of 4.04 which results in a percent error of 5.4%.

5.3.2 High humidity testing procedure

For tests in which an increased relative humidity was needed, the steam generator was implemented. Prior to a test, the steam generator was opened and drained of any remaining water from a previous test. 500 mL (0.13 gal) of ultra-pure type 1 deionized water was added to the humidifier. Once the test started, nitrogen displacement turned on, and the plate started to cool, then the steam generator was turned on and set to the highest power level. After a few minutes, the steam generator output steam into the large wind tunnel but because the test section airflow was closed and because of the nitrogen displacement, the steam was unable to reach the test plate surface. Once the test plate surface reached the target temperature, the nitrogen was turned off and the airflow valve was opened to allow the now humidified air to pass through the test section.

In order to maintain a sufficient supply of water inside the steam generator, water was added approximately every 30 to 40 minutes. Typically for a 1 hour test, the humidifier needed to be refilled only once. Prior to a refill, approximately 500 mL (0.13 gal) of water was heated to a boil inside of a microwave oven and then poured into the generator. If the steam generator was refilled with cold water, the steam output would immediately stop until the humidifier brought the

water up to boiling temperature.

5.4 Pull-down test procedure

In order to simulate a more realistic situation in which the test plate would gradually cool to operating conditions all the while condensation accumulated, a pull-down test was developed. This test began at a constant air temperature, humidity and air flow rate. This test was similar to the constant surface temperature test, but no nitrogen was used. The recording was initiated, and a few minutes of ambient conditions was recorded first. Then the EGW flow was initiated and set to a specified flowrate. The TECM were turned on and set to a power level higher than the anticipated required power level for that specific test's operating condition. This prevented the test plate from cooling too slowly. Once the surface temperature came within 0.55°C (1.0°F) of the target, the TECM power levels were reduced to the level required to maintain the target temperature. The test was carried on for a duration of 1-3 hours depending on weather the test plate would be removed for mass measurement.

5.5 Cycling test procedure

The cycling test is a six-part test which explored the performance and behavior of the uncoated, hydrophobic, and hydrophilic coated surfaces. The purpose of this test is to observe the possible effect that these coatings could have on a real world defrost duty cycle typical of a traditional vapor compression cycle. At the onset of the test an air flow rate of 138.8 l/m (4.9 cfm) was set. This flow rate corresponded to a pressure difference across the nozzle of 746 Pa ($3.0\text{ in. H}_2\text{O}$). This value was allowed to fluctuate for the subsequent cycles as frost growth would create a pressure drop naturally. The first portion of the test was considered to be a "pull-down" test wherein the surface temperature was reduced gradually until the desired surface temperature condition was met and maintained. Condensation on the surface would collect and freeze and then

frost would form and grow. The frost grew until it caused a pressure drop across the test section of 0.35 in. H₂O. At that moment, the TECMs were turned off for a period of exactly 12 minutes. During this period, the frost on the surface melted and the pressure drop across the test section decreased. The TECMs were turned back on and frost was allowed to accumulate again. This process was repeated until 6 frost growth periods and 5 defrost periods had been performed.

5.6 Surface cleaning procedure between experiments

It was found that the surface would become contaminated with some unknown contaminant which would cause the liquid condensation to nucleate into ice much sooner than normal resulting in very short freezing times as shown in Figure 21b.

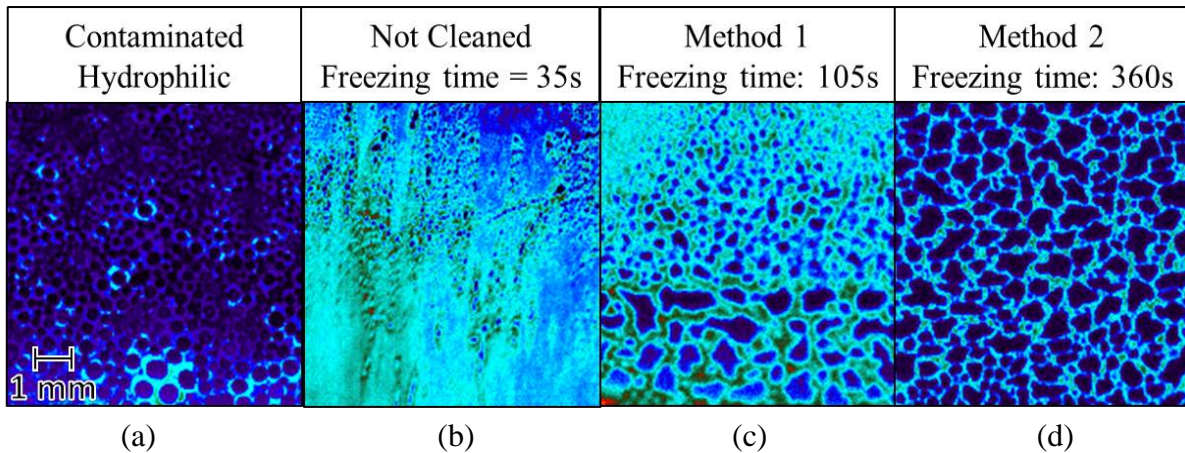


Figure 23: Images from IR camera showing typical type of iced droplets (a) contaminated hydrophilic surface; (b) new surface never cleaned; (c) after cleaning with Method 1; and (d) after cleaning with Method 2

Experiments were conducted to compare two cleaning methods with the objective of achieving consistent and longer freezing times. Cleaning method 1 involved the use of cotton swabs dipped in 99% isopropyl alcohol to swab the test plate to remove any contaminant and then allowing the alcohol to evaporate from the surface. Cleaning method 2 consisted of three steps. Step one was to use the cotton swabs dipped in isopropyl alcohol as done in cleaning method 1. Step two is to use a cotton swab dipped in distilled water to swab the test plate. Finally step three

is to use a lint free cotton cloth to absorb the remaining distilled water on the surface to dry the surface prevent droplets from drying and creating water marks. The second cleaning method was found to give longer freezing times and, in several cases, had a visually obvious improvement. Figure 21 shows the test surface at the moment of freezing using both cleaning methods. It is clearly shown that the first cleaning method left contaminated streaks on the surface resulting in uneven droplet distribution. Furthermore, the freezing time for the second cleaning method was approximately 3.5 times longer than the first cleaning method. Both cleaning methods were used on a piece of borosilicate glass and it was confirmed that cleaning method 1 resulted in a surface with visible streaks whereas cleaning method 2 resulted in a surface with significantly fewer or no visible streaks. The streaking likely occurs because the isopropyl alcohol dissolves the contaminants on the surface and simply spreads it around on the surface without fully removing it. The addition of the distilled water and drying steps allows for the contaminants to be suspended in the water then removed completely by the dry cloth.

It was also found that isopropyl alcohol had a negative effect on the contact angle for the hydrophilic surface resulting in a more hydrophobic contact angle. Therefore, the cleaning method for the hydrophilic test plates only used the distilled water cleaning and the drying steps from method 2. If the hydrophilic test plates did become contaminated with a hydrophobic contaminant such as oil, the plate was removed from the test section and soaked in an isopropyl alcohol bath to remove any contaminant. In order to restore the contact angle to previous hydrophilic values, the test plate was then submerged in a bath of 30% hydrogen peroxide for at least 1 hour. After this treatment, the test plate was dried and was ready to be installed into the test section.

5.7 Test plate replacement and plate cleaning procedure

After a test plate was removed using the procedure described previously in the section

discussing the manual frost mass measurement procedure, another test plate needed to be installed. Prior to installing a test plate, both the empty test section and the test plate were cleaned.

To clean the empty test section, any residual thermal grease left behind by the previous surface was gently scraped off while avoiding scratching the surface of the temperature plate, which is now the exposed surface. Cotton swabs and lint free cotton cloth squares were then used along with isopropyl alcohol to remove the remaining thermal grease. It was not necessary to remove all of the residue on the surface however it was important to collect any globules of thermal grease that had accumulated in any corners and cracks to prevent any undesired thermal bridging for the next test plate.

To clean the test sample, the majority of the thermal grease was gently removed using a paper towel or cloth. Then a soft towel and isopropyl alcohol was used to gently dissolve any remaining visible thermal grease from the surface. The plate was then submerged in an isopropyl alcohol bath for approximately one hour. The test plate was then removed and dried. A lint free cotton cloth and distilled water was used to wipe the surface and then dried again.

Because isopropyl alcohol increased the contact angle of the hydrophilic coating, to retain its original contact angle, the hydrophilic surfaces were removed from the isopropyl alcohol, dried, and then submerged in a 30% concentrated hydrogen peroxide bath for approximately 1 hour. Similar to the hydrophobic and uncoated surfaces, the plate was removed and dried off with a clean lint free cotton cloth. It was not necessary to wipe the surface again with distilled water like for the other two surfaces because any remaining hydrogen peroxide would evaporate or dissociate into water naturally.

Once the test section and the test plate were cleaned, the test plate could be prepared for installation. A thin strip of adhesive rubber foam insulation was attached to the test plate on the

front and side edges of the test plate. New thermal grease was then applied to the bottom uncoated side of the test plate in a zig-zag pattern. A sufficient amount of thermal grease was added to ensure that the test plate made good contact with the surface below it. The experimenter would practice this procedure on an example test plate and a piece of acrylic in order to practice this procedure and to be able to actually see the contact area being made on the underside of the acrylic. This helped the experimenter to understand the amount of thermal grease required to ensure good and even contact.

The test plate was then carefully installed into the test section and centered. Then the clamping pins were secured. This installation process was completed while wearing gloves and while being very careful not to contaminate the coated surface with thermal grease. Typically, the first test after installation resulted in poor results, but after one daily cleaning the results became more reasonable.

Chapter 6: Data Analysis

6.1 Introduction

Once the raw data was collected, it needed to be processed and computed in order to understand. In the case of the videoscope and IR camera, the footage needed to be analyzed to quantify the information which could then be used to be plotted or used in other calculations.

6.2 Frost Thickness Image Processing

Real time videos of frost growth were taken by using the HD CCD camera. The videos were input into the multimedia processing software, ffmpeg, to create a series of jpeg images for every 10 seconds. A MATLAB function flattened images using a checkerboard calibration pattern. Calibration curves of pixel per millimeter across the images were created and MATLAB's Fuzzy Logic Toolbox and provided the outline of the frost in each image, as shown in the example of Figure 22. Once a binary image was generated, a MATLAB code calculated the number of white pixels in each column and the instantaneous height of frost across the entire width of the observation window. The uncertainty of the frost thickness measurement was about $\pm 7.6\%$.

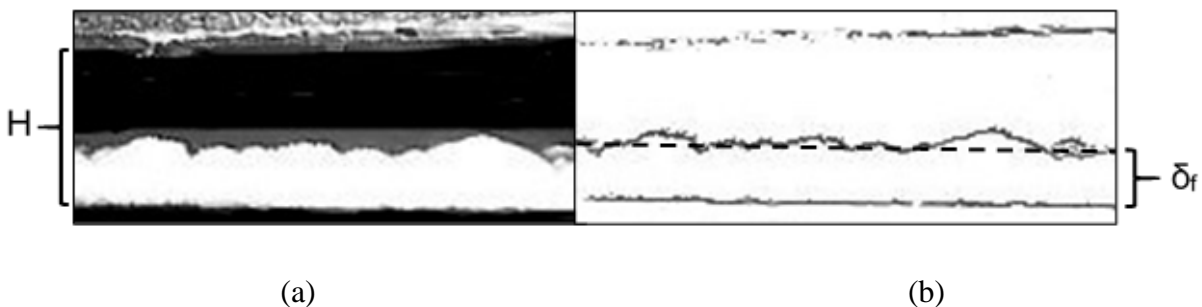


Figure 24: (a) Flattened image from video scope, and (b) frost outline created from the actual image

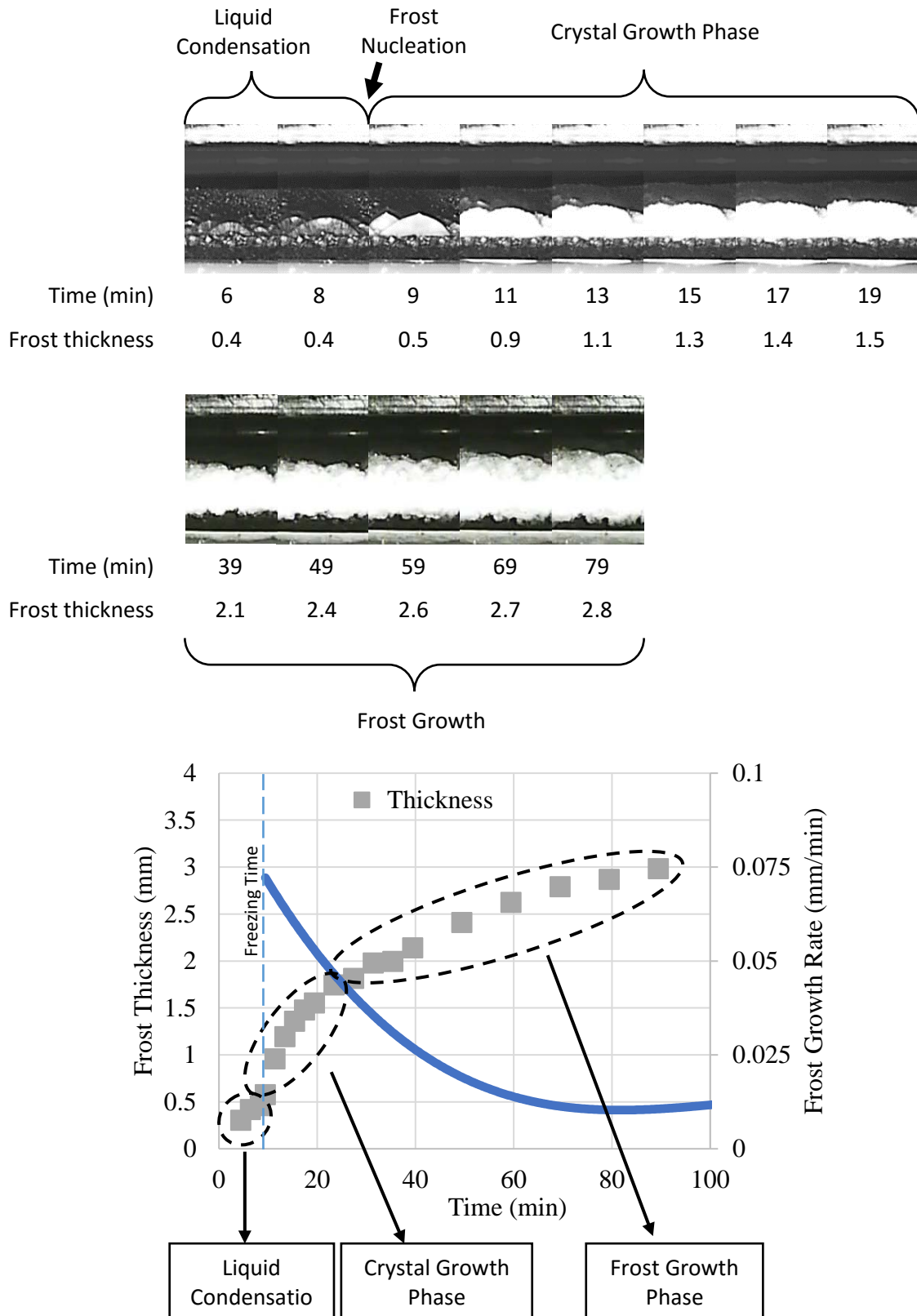


Figure 25: Sample frost thickness analysis

Figure 23 is an example of the results from a frost thickness analysis where three phases of condensation and frost growth are shown. It can be seen clearly that the frost growth rate decreases as the frost thickness increases. The crystal growth phase is indicated by a large frost growth rate and gradually transitions into the frost growth phase where frost densification is more prevalent.

6.3 IR Camera Image Processing

An infrared camera measured the surface temperature and the frost temperature. The range of emissivity for all test plate surfaces was determined by calibrations and it was about 0.42. Emissivity values for snow (the closest approximation to the texture that we observed) ranged from about 0.8 to 0.85 (Siegel and Howell, 2002). In the present study, the emissivity values were adjusted between the 0.42 for the surfaces in dry conditions and increased linearly up to 0.82 for the droplets condensation and during early frost growth stages. The infrared camera also measured the diameter of the droplets that condensed and then froze on the test plate, i.e., measured the average diameter of the ice beads. Figure 24 summarizes an example, and the smallest droplets that could be individually distinguished from each other had diameter of 110 to 120 μm . The individual ice beads are circled in white and a binary image provided the actual shapes and sizes of the ice beads immediately after freezing took place.

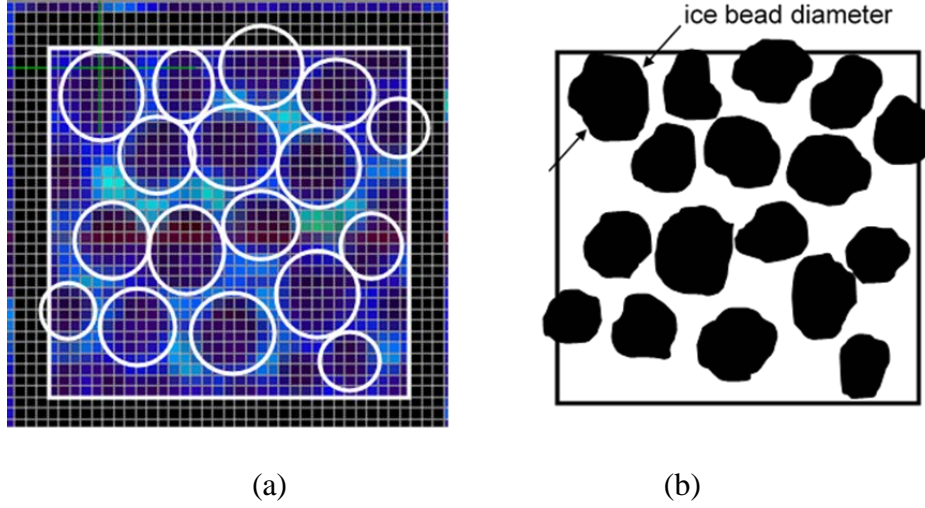


Figure 26: Droplet size (a) and (b) actual ice bead shapes and sizes immediately after freezing

6.4 Frost mass calculations

The frost mass calculated by using Equation (1) and the frost density was calculated by using Equations (2) – (3).

$$m_f = \sum \dot{m}_a (\omega_{in} - \omega_{out}) t_{step} \quad (1)$$

$$\rho_f = \frac{m_f}{Vol_{f,avg}} \quad (2)$$

$$Vol_{f,avg} = A_s \delta_f \quad (3)$$

The volume of frost was calculated assuming the frost profile along the depth of the plate, i.e., in the direction of the air flow, was linearly decreasing with angle α , which was taken as average between maximum and minimum possible angles observed in the experiments. The heat flux through the test plate was measured with the flux meter, as follows:

$$q''_{tee} = \frac{\Delta T_{tee}}{R_{tee}} \quad (4)$$

$$R_{tee} = \frac{L_{tee}}{k_{steel}} \quad (5)$$

Using an average value of the contact resistance between the heat flux meter and the test plates, which was derived from calibration tests, the temperature of the top surface of the test plates and the air-side heat transfer coefficients were obtained by using Equations (7) – (10).

$$T_s = R_c q''_{tee} + T_{tee,bottom} \quad (6)$$

$$R_c = \frac{\Delta T_{tee} + \Delta T_s}{q''_{resistor}} \quad (7)$$

$$q''_{resistor} = \frac{Voltage^2 R_{electric}}{A_s} \quad (8)$$

$$h = \frac{q''_{air}}{(T_{a,in} - T_{fs})} \quad (9)$$

6.5 Dew point temperature correction

During the constant surface temperature test procedure, the outlet and test section were purged with dry nitrogen gas. As a result during this period, the outlet dew point sensor measured an extremely low dew point temperature. When the nitrogen was stopped and the airflow started, the outlet dew point sensor took several minutes to readjust to measure an accurate dew point temperature, and in the process the sensor would measure values even higher than the inlet dew point sensor. This was an artifact of the dew point sensor overshooting the correct dew point temperature resulting in a false spike. This can be seen in Figure 25 at time 0 seconds. In order to correct this artifact in the data analysis, the outlet dew point temperature was linearized from the time that the nitrogen was turned on to the time at which the dew point sensor reached a minimum

or steady value after the airflow started. The mass summation from Equation 1 only summed values from after the airflow start ($t=0s$). With these corrections, the data analysis resulted in a more accurate calculation of frost mass.

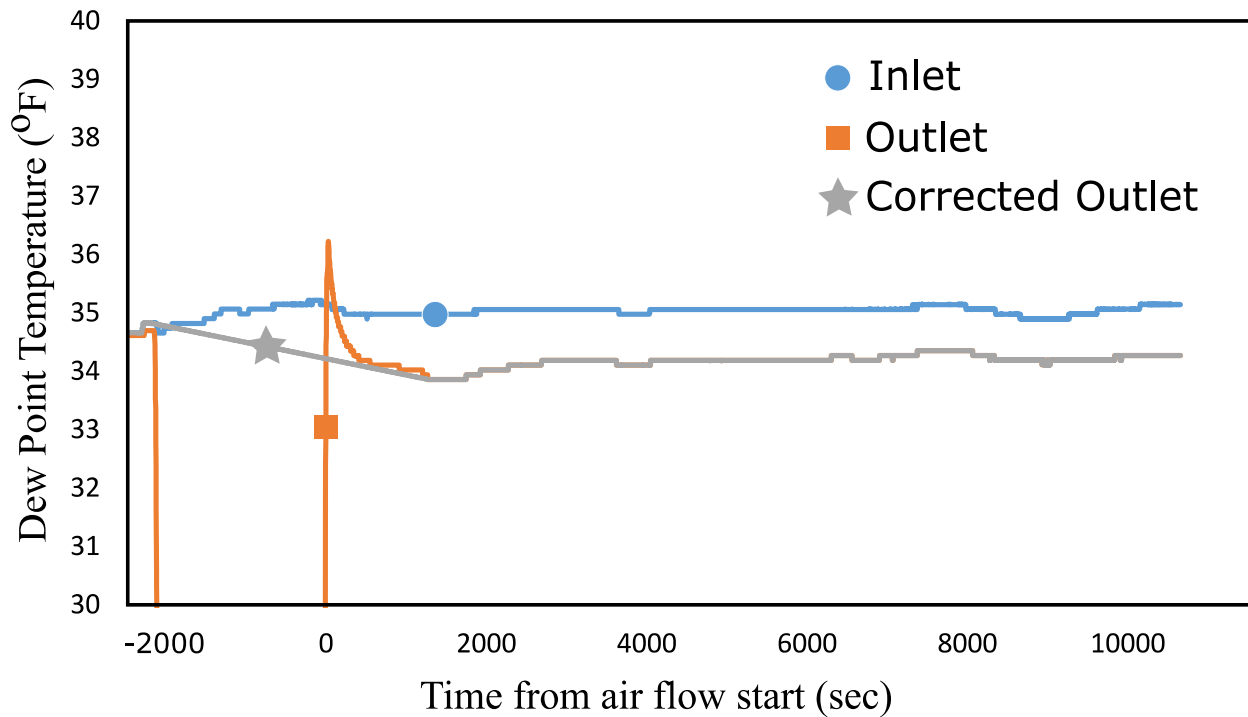


Figure 27: Example of inlet and outlet dew point temperature correction

6.6 Uncertainty Analysis

The uncertainty of individual sensor instrumentation was provided by the manufacturer. An uncertainty analysis was conducted to determine the uncertainty of calculated variables based on these individual sensor uncertainties. The program Engineering Equation Solver (EES) was used to calculate the uncertainty of these variables. EES implements a Taylor series uncertainty propagation method to calculate uncertainty. This method is calculated according to equation 11

where U_Y = is the uncertainty of the calculated variable, U_{X_i} is the uncertainty of the individual sensor and n is the number of sensors.

$$U_Y = \sqrt{\sum_{i=1}^n \left(\frac{\partial Y}{\partial X_i}\right)^2 U_{X_i}^2} \quad (10)$$

The uncertainties of the calculated variables are presented in Table 1 found in Chapter 4.

In addition to the Taylor series uncertainty propagation method, a bias uncertainty analysis method was used to calculate the uncertainty that arises from the use of multiple sensors measuring a single variable. In this thesis, this applied to thermocouple arrays measuring air average temperatures at a common location. This method is calculated according to equations 12 – 14 where B_T is the bias uncertainty of the calculated temperature and $B_{T,distribution}$ was taken as 0.2°C .

$$B_{T,distribution} = \frac{T_{max} - T_{min}}{n} \quad (11)$$

$$B_{T,uniform} = \frac{\Delta T_{uniform}}{n} \geq U_T \quad (12)$$

$$B_T = \sqrt{B_{T,uniform}^2 + B_{T,distribution}^2} \quad (13)$$

The bias uncertainty and Taylor series uncertainty for all temperature averages ranged from 0.03°C to 0.01°C but a more conservative temperature uncertainty of $\pm 0.056^\circ\text{C}$ (0.1°F) was presented.

Chapter 7: Calibration and Verification of Test Setup

7.1 Introduction

Prior to testing, in order to calibrate and verify the sensors, various calibration procedures were conducted. These procedures ranged from simple sensor calibrations to small tests including a double T-block calibration test and steady state wet tests.

7.2 Double tee calibration test

Before final assembly of the test apparatus, the T-block assembly (cold plate, TECM, T-block, and temperature plate) was tested to verify that all of the thermocouples were functioning and to calculate the thermal resistance of the T-block assembly.

The T-block assembly was positioned to allow free clearance above the test plate. The test plate was an uncoated test plate. A thermocouple plate and another stainless-steel T-block was installed above the test plate as shown in Figure 26. Thermal grease was used to improve the thermal contact between the surfaces. At the top of the test setup, a resistive heater was attached. Once the components were secure and temperature sensors were in place, the entire assembly was thoroughly insulated.

The resistive heater had an internal resistance of 68Ω . With this known electrical resistance, the heater was powered at a set voltage of 45.1V to provide a calculated power output of 30 watts. On the bottom side of the assembly, chilled EGW was flowed through the cold plate and the TECM were powered on. Both the EGW flowrate and the TECM power settings were controlled until the temperature readings on all sensors were constant and the test setup could be considered steady state. The LabVIEW program recorded these data for a short period of time and

then the test was concluded.

Later during the analysis, based on the known power input from the resistive heater and the measured temperatures from the thermocouples, we were able to calculate a thermal resistance of the T-block and the thermocouple plate/test plate pair.

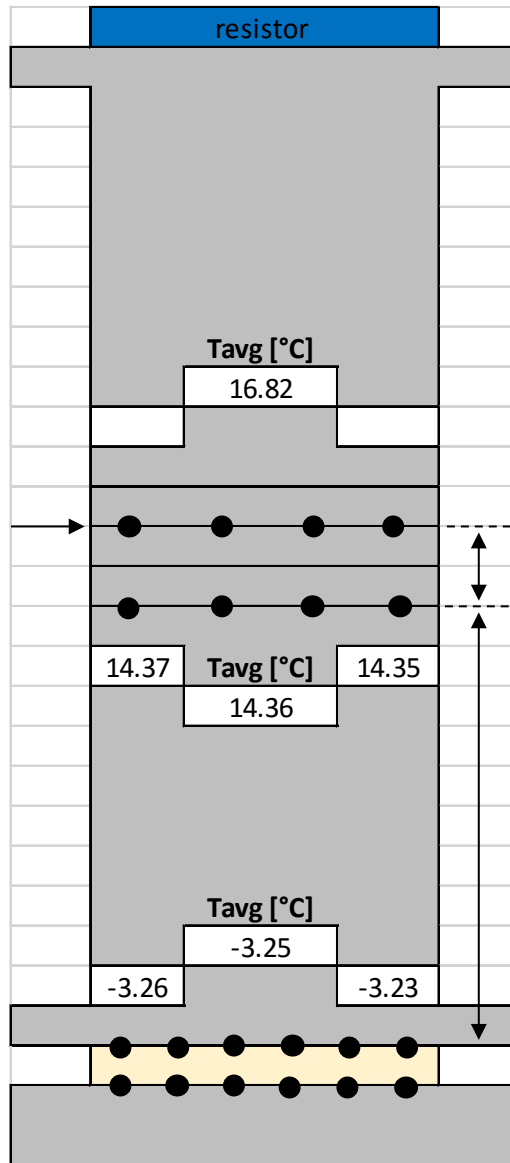


Figure 28: Layout of double T-block calibration test.

7.3 Steady state wet test

Upon installing a new test plate, it remained uncertain if the thermal resistance network had remained constant. The primary concern was with the contact resistance of the thermal grease layer. To verify that the thermal resistance had remained constant, a few steady state tests were conducted each time a surface was replaced. These steady state tests were conducted by firstly setting the air temperature the value shown in Table 2. The EGW tank temperature was set to 0.67°C (33.2°F). Once these conditions were reached, a LabVIEW recording was started, the EGW flow was then started and the EGW flow rate was adjusted to 6.3 mL/s (0.1 Gal/min). The EGW heater was then turned on once flow was established. The TECM were turned on and set to constant values represented in Table 2.

Table 2: Set point conditions for steady state wet tests

Test ID	Air Temperature °C (°F)	Front TECM Voltage (V)	Back TECM Voltage (V)
1	8.33 (47.0)	1.2	1.6
2	4.94 (40.9)	1.1	1.75
3	12.78 (55.0)	1.4	1.9

Liquid condensation was allowed to accumulate during these tests which is why these tests were called steady state wet tests. The surface continued to decrease in temperature until the system reached a thermally steady state. This was confirmed by the temperature sensor measurements remaining within a 0.1°C (0.2°F) temperature range. The test was continued for approximately 30 minutes after this steady condition was reached. The test was stopped by first turning of the TECM, then the EGW heater, EGW booster pump, and lastly the LabVIEW Recorder in that order.

Sometimes during these tests, the surface droplets would freeze before the full 30 minutes of steady state recording was reached, or sometimes even before the surface temperature became

steady. In the event that at least 5 minutes of steady recording was reached before freezing, the test was ended and was not retested. The logic behind this decision was that if the 5 minutes of data verified the thermal network as well as the other two steady state tests, then it could be safely assumed that the thermal network was verified. On the other hand, if the surface froze before steady state could be reached, then the test was redone.

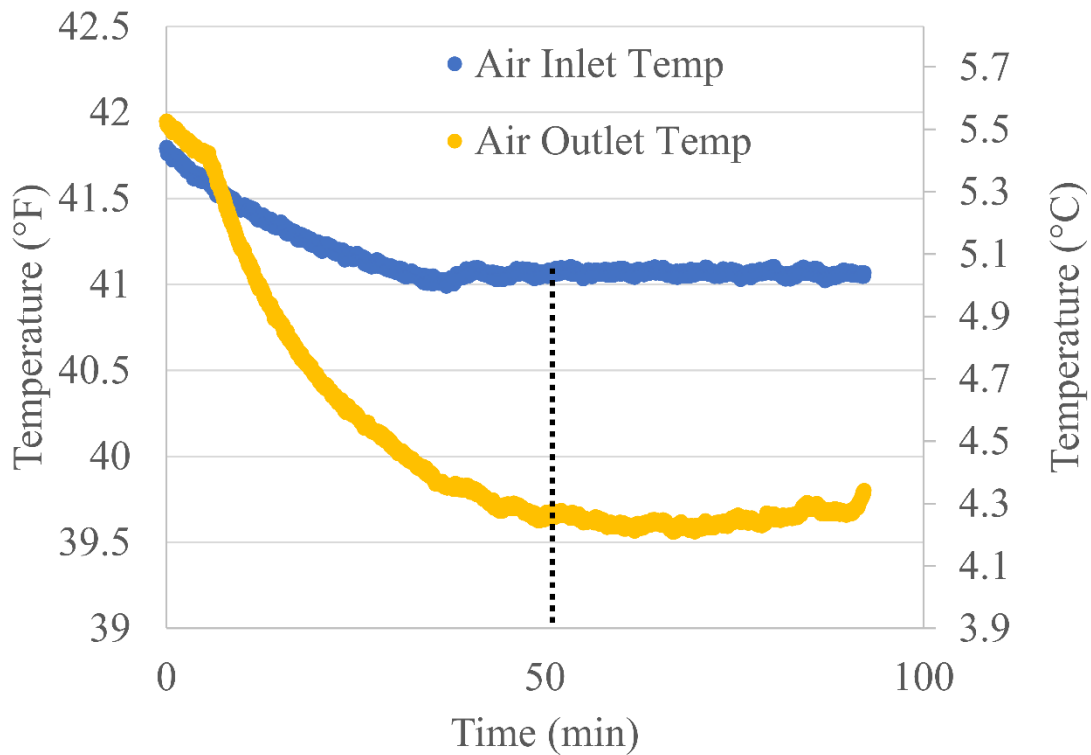


Figure 29: Temperature comparison at the inlet and outlet of the test section for steady state wet tests

To redo a steady state test, or to conduct a steady state test in the same day after another test was conducted, the frost was first thawed. It was helpful to insert a clean cloth or paper towel inside the test section on top of the frost. This way as the frost melted, it would be immediately absorbed instead of possibly running off the surface and wetting the surrounding insulation. Once the frost was thawed, the surface was allowed to warm slightly, and the surface was wiped dry

with a lint free cotton cloth. Removing the water from the surface helped to achieve a steadier recording. If the water remained on the surface, as the droplets got larger and coalesced, the surface temperature would fluctuate more erratically. It was not necessary to start the steady state tests with a completely dry surface as is the requirement for the nitrogen tests because the initial conditions of the steady state test were of little importance to the final steady state conditions.

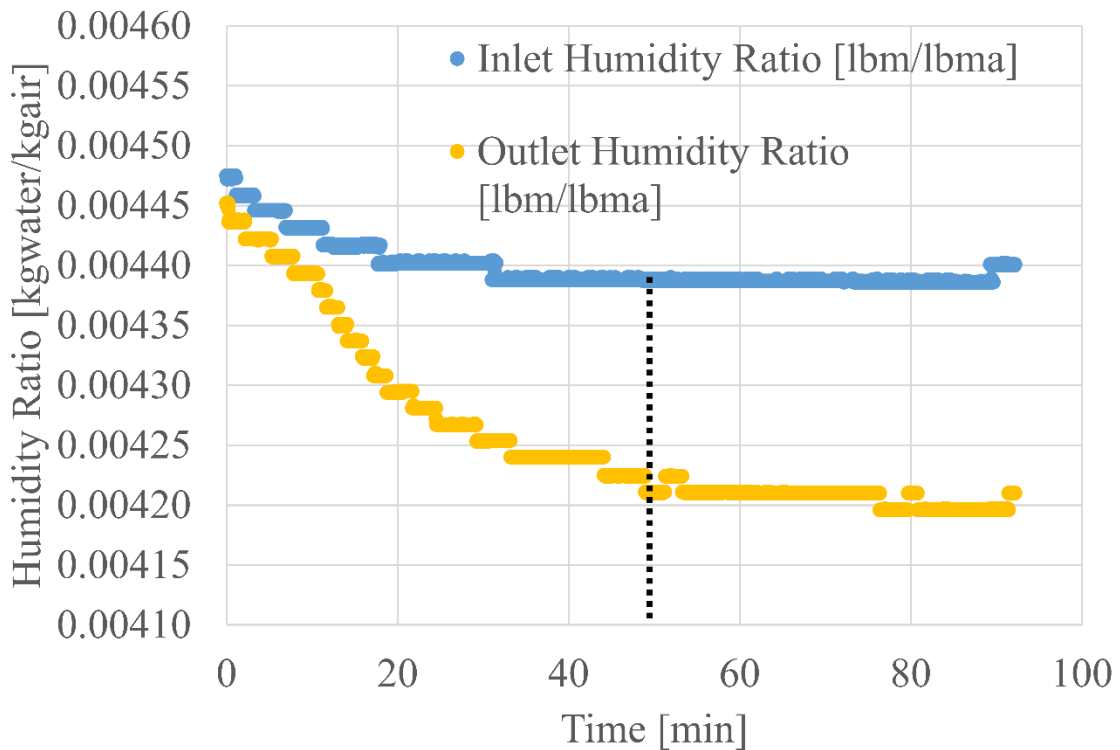


Figure 30: Humidity ratio comparison at the inlet and outlet of the test section for steady state wet tests

Sensible and latent heat transfer rates were calculated from the temperature and humidity ratio measurements at the inlet and outlet of the test section. These values were then used to compare the heat transfer coefficient of the test plate to a baseline heat transfer coefficient range of $h_o = 100$ to $120 \text{ W/m}^2\text{-K}$ as calculated from the experimental system for steady state conditions. If the heat transfer coefficients of the subsequent test plates were to differ significantly from the

baseline, then the necessary corrections were made to make sure that all the heat transfer coefficient values matched to an acceptable level.

The analytical calculation of the convection heat transfer coefficient (h) necessitates some careful consideration due to the possible differences between the experimental system and the ideal physical set ups based on which the formulas in the literature are given.

The convection coefficient (h) is calculated analytically from the Nusselt (Nu) correlation:

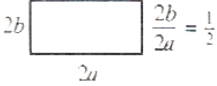
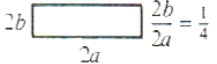
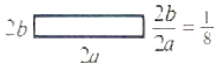
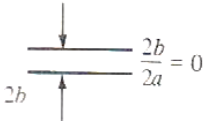
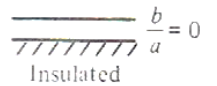
$$Nu = \frac{h D_h}{k} \quad (14)$$

where D_h is the hydraulic diameter and given by:

$$D_h = \frac{4A_c}{P} \quad (15)$$

where A_c is the cross sectional area of the test section airflow path and P is the wetted perimeter.

Table 3: Nusselt number for hydrodynamically and thermally developed laminar flow in various cross-sections [Ozisik, M. N., Heat Transfer: A Basic Approach, McGraw-Hill Book Company, 1985].

Geometry ($L/D_h \gtrsim 100$)	Nu_T
	3.391
	3.66
	5.597
	7.541
	4.861

* From Shah and London [5].

For the flow conditions of the experimental system (for the air flow with 1 bar pressure and 5°C), the thermal conductivity of the bulk air flow was $k = 0.025 \text{ W/(m}\cdot\text{°C)}$. For laminar flow inside ducts of various cross sections, the Nusselt number (Nu) for uniform surface temperature (Nu_T) is given in Table X [Ozisik, M. N., Heat Transfer: A Basic Approach, McGraw-Hill Book Company, 1985].

The geometry of the test set up is closest to the last configuration in Table X. Therefore, for a Nusselt number of 4.861 and a calculated $D_h = 7.79 \cdot 10^{-3} \text{ m}$, the theoretical heat transfer coefficient h is about $16 \text{ W/(m}^2 \text{ K)}$. This value seemed too low and might not be a realistic benchmark for the comparison because of the following two reasons. First, the table indicates that the values are valid for $L/D_h \gg 100$ and $b/a = 0$. In the current experimental setup, $L/D_h = 3.26$ and $b/a = 38.1$. If I consider that the flow is undeveloped at the entrance of the duct, it would take 0.662 m (26.06 inch) of duct length for the air flow to be fully developed hydrodynamically and 0.47 m (18.5 inch) of duct length to be fully developed thermally (when heated from both sides) using the formulas below (Incropera et al. (2003)):

$$\left(\frac{x_{fd,h}}{D}\right) \approx 0.05 Re \quad (16)$$

$$\left(\frac{x_{fd,t}}{D}\right) \approx 0.05 Re Pr \quad (17)$$

where $x_{fd,h}$ is the hydrodynamic entry length and $x_{fd,t}$ is thermal entry length. Even if the flow is considered to be partially developed at the entrance of the duct, it is unlikely that within the depth of the experimental setup of only 0.0254 m (1 inch) along the direction of the air flow, the conditions resulted developed fully hydrodynamically or thermally. Rather, the upper duct wall of my test setup geometry had very little effect on the thermal boundary conditions created in the flow by to the bottom cold test plate. Thus I can compare my data with the theoretical heat transfer

coefficient h for a laminar flow over a flat plate rather than a duct flow.

Considering a laminar flow over a flat plate, the average Nusselt number at a distance downstream from the edge of the plate can be calculated as (Incropera et al. (2003)):

$$\overline{Nu} = 0.664 Re^{1/2} Pr^{1/3}, Pr \geq 0.6 \quad (18)$$

with $Re = 7190$ and $Pr = 0.7101$ determined by using the EES software with the experimental test conditions as the input. The average Nusselt number results 50.2, which gives a convection coefficient of 49.4. This value is still below the experimental ranges. The possible reason is that the flow in the duct may have a higher Re number due to the disturbances caused by the inlet leading edges of the test plate. There could be a small discontinuity between the plastic inlet duct and the metal plate that turbulate and trip the air flow within the film boundary region in the bottom wall of the duct. This discontinuity was not visible in the setup by naked eye or by the videoscope but nevertheless microscopic gaps could still be present. Finally, as first order of magnitude analysis, I can compare the h_0 from steady state experimental tests in dry/wet conditions with the theoretical heat transfer coefficients over a flat plate for turbulent flows regime. Nusselt number for turbulent flow over an isothermal plate is given by (Incropera et al. (2003)):

$$Nu = 0.0296 Re^{4/5} Pr^{1/3} \quad (19)$$

where Prandtl (Pr) number is between 0.6 and 60. Using the values of $Re = 30000$ and $Pr = 0.71$ results in the convection heat transfer coefficient of approximately $99 \text{ W/m}^2\text{-K}$. This theoretical value of h is in agreement with my measured h_0 from steady state experimental tests in slightly wet surface conditions, which ranged from 80 to $120 \text{ W/m}^2\text{-K}$.

7.4 Sensor calibration and verification

Prior to installation and testing, certain sensors required to be calibrated and verified. The

calibrations were typically done by referencing a more accurate sensor. Verification was accomplished by either repeating a calibration measurement or by comparing multiple sensors to check that they are all in agreement.

7.4.1 Temperature

To achieve accurate temperature measurements, each of the thermocouples were calibrated prior to being installed. Using the National Instruments Measurement & Automation Explorer (NI MAX) program, the thermocouples were calibrated in reference to a VWR® Traceable® platinum ultra-accurate thermometer which had an uncertainty of $\pm 0.013^{\circ}\text{C}$ ($\pm 0.0234^{\circ}\text{F}$) according to the sensor's calibration certificate (Figure 29). A Cole-Parmer Polystat® cooling/heating circulating bath was used to maintain a 50% ethylene glycol 50% water mixture bath at a constant temperature. The picture of the bath is shown in Figure 30. The ultra-accurate thermometer and all of the thermocouples to be calibrated were submerged in the bath being careful that none of the sensors were touching but that they were all close together in the fluid to avoid any local differences in fluid temperature.



Figure 31: Ultra accurate thermometer



Figure 32: Circulating temperature bath

The bath was set to a constant temperature. Approximately half an hour was enough time for the bath to reach a fully steady temperature which confirmed by the ultra-accurate thermometer. Using the NI MAX program, the values of each of the thermocouples were averaged across one second to average out some of the digital noise, and the temperature measured by the ultra-accurate thermometer was also recorded. This process was repeated at several points across a desired range of temperatures. The NI MAX program then calculated a line-fit for the measured values. This calibration was verified by repeating the measurement process at a few different temperatures and in a different order than the calibration was made. This was to ensure that there was no hysteresis effect during the initial calibration.

Once the calibration was completed, the thermocouples were then removed from the bath,

wiped clean, then installed in their final measurement positions. For most temperature measurements, multiple thermocouples were used to record the temperature of the region. This was done to help avoid bias uncertainty. Using multiple thermocouples also made it easier to check that their values did not drift over time. A so-called iso-temperature check was conducted to verify correct readings with no drift.

For an iso-temperature check, conditions for the large wind tunnel were set at a constant value and the entire system was allowed to come into equilibrium over the course of several hours. The measured values from the thermocouples were recorded then compared to each other. An example this type of verification is shown in Figure 31. The circles are individual data points and the line represents the average. The measured values are well within the $\pm 0.056^{\circ}\text{C}$ (0.1°F) uncertainty shown in Table 1.

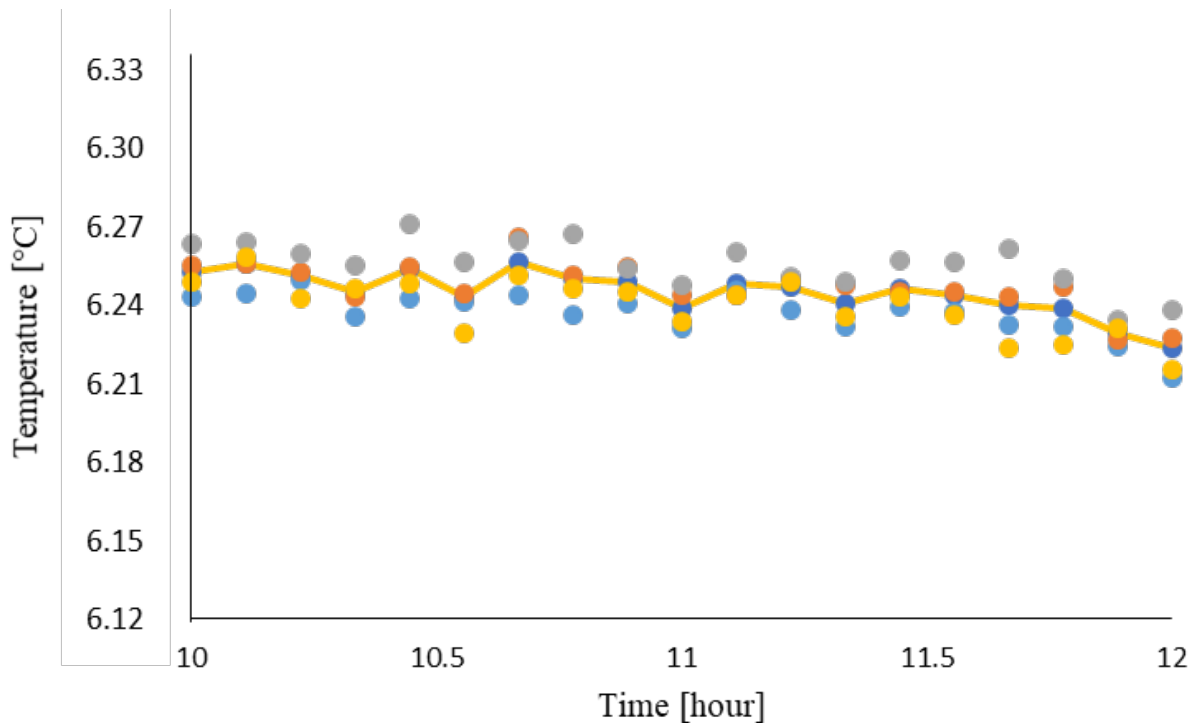


Figure 33: Example of temperature measurements of thermocouples at test section inlet during an iso-temperature check

7.4.2 Air Water Content – ω

Water content in the air was measured by relative humidity (RH) sensors and dew point sensors. The RH sensors were less accurate at measuring air water content than the dew point sensors however they served as a useful tool to verify that the dew point sensors were functioning properly. A simple verification test was designed to accomplish this task. This test consisted of maintaining the temperature, humidity, and flow rates at a constant level for some time. Then data from the dew point sensors, RH sensors, and temperature sensors were all measure and recorded. From these measurements, water content at each point was calculated using psychrometric property tables. A simple uncertainty analysis was conducted to confirm that the measured differences between the sensors fell between the sensor's tolerance levels. It was important that the temperature was measured at the same point as the RH sensor or the dew point sampling probe. For example, because the outlet RH sensor was located outside of the large wind tunnel, and because the temperature of the air at the sensor was warmer because of this, a thermocouple was installed directly next to it in order accurately measure the temperature and thus water content.

Similar to the iso-temperature check, an iso- ω check was conducted. After reaching steady conditions, the dew point temperatures from the dew point sensors and relative humidities from the RH sensors were recorded. From these values and from dry bulb temperature measurements at the location of each of the sensors, the air water content was calculated and compared. Figure 32 shows an example of the humidity ratio for each sensor from one of these checks. It can be seen that the inlet and outlet dew point sensors are practically identical and the RH sensors are slightly different.

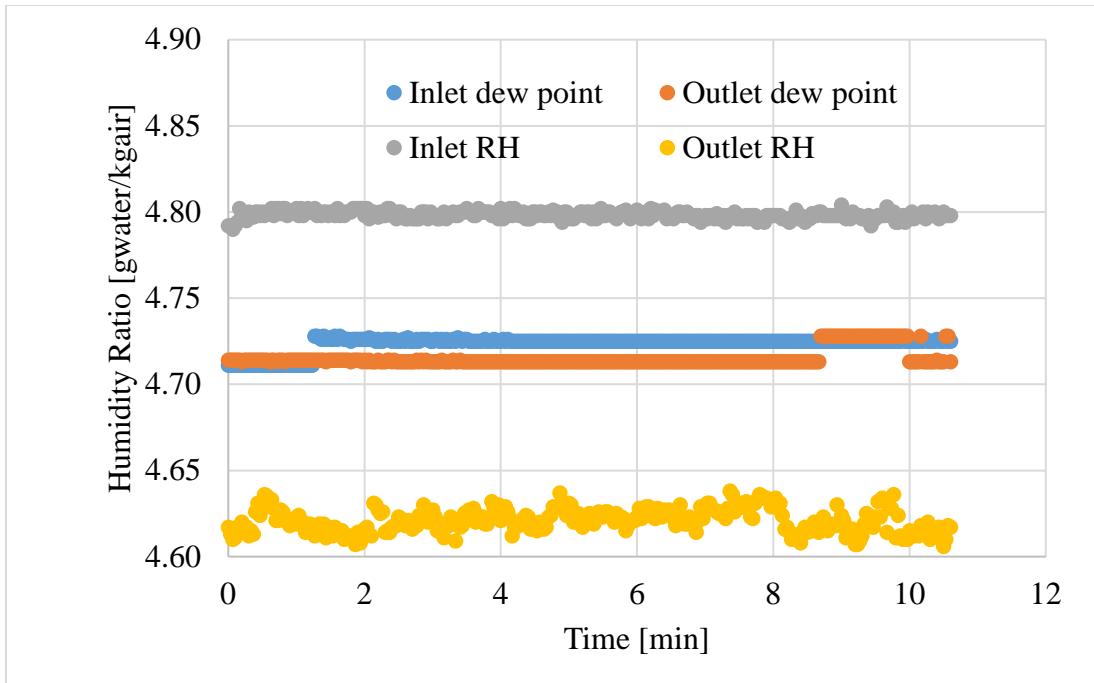


Figure 34: Example of water content recordings during an iso- ω check

During constant surface temperature tests in which nitrogen was used, nitrogen displaced the humid air as the test plate cooled to operating temperature at which point the nitrogen was removed. The duration of nitrogen displacement was approximately 20-25 minutes. In order to verify that the nitrogen was not a variable affecting frosting properties, a constant surface temperature test was conducted but the nitrogen displaced air for approximately 35 minutes. The results showed that the nitrogen had no discernible effect on the freezing time or frosting properties.

Chapter 8: Results and Discussion

8.1 Frost characteristics during tests with small variations of the surface temperature

Figure 33 presents frost thickness at the leading edge of the test plates as a function of time for all surfaces (aluminum, hydrophobic, and hydrophilic) during the nitrogen displacement tests. The frost thickness, δ_f , was normalized with respect to the height of the channel, $H_{\text{channel}} = 4\text{mm}$ (0.16 in.), of the cross section of the rectangular duct available to the airflow directly above the test plates. It was observed that there was a rapid increase of frost thickness during the first four to six minutes of frosting and the graph in Figure 34 presents zoomed-out plots during this period of the frosting tests. The thickness trends for the aluminum and hydrophilic surfaces were similar. They both had significantly lower thickness during the initial frost accretion period. Then, the frost thickness increased slowly and with almost constant slope for the remainder of the frosting period. The surface characteristics affected the time and the initial thickness of the frost after the droplets froze on the test plates. This was also the starting point for the frost growth phase.

Figure 35 shows the average frost density as a function of time for all surfaces during the nitrogen displacement tests. The density for the aluminum surface was the highest and showed large fluctuations during the early stage of frost growth, as shown in the zoom out of Figure 36. These fluctuations were likely due to the uncertainty in frost thickness during the initial crystal growth period because for thicknesses smaller than 0.4 mm, the frost mass was very small, and the calculated density resulted quite sensitive to small apparent fluctuations of frost layer thicknesses measured from the digital images.

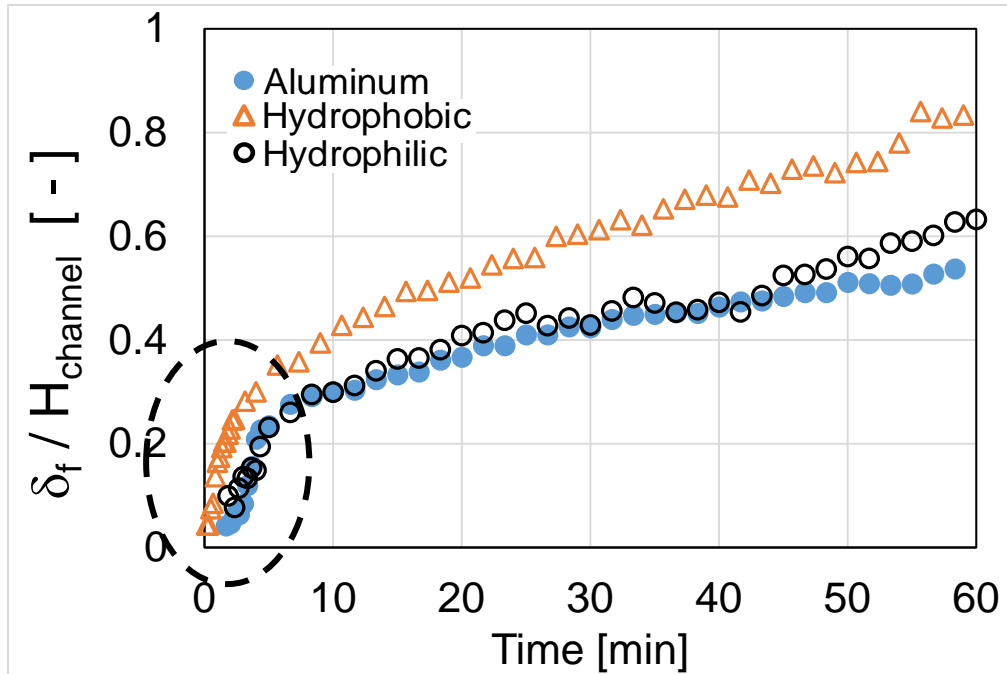


Figure 35: Frost thickness vs. time for all surfaces (coatings) during the nitrogen displacement tests - Frost thickness during the entire test period (Heat Flux of 1300-1500 W/m², T_s = -15 °C, T_{a,in}= 5°C, Humidity inlet of 80 % R.H., Flow Rate of 8.5 m³/h)

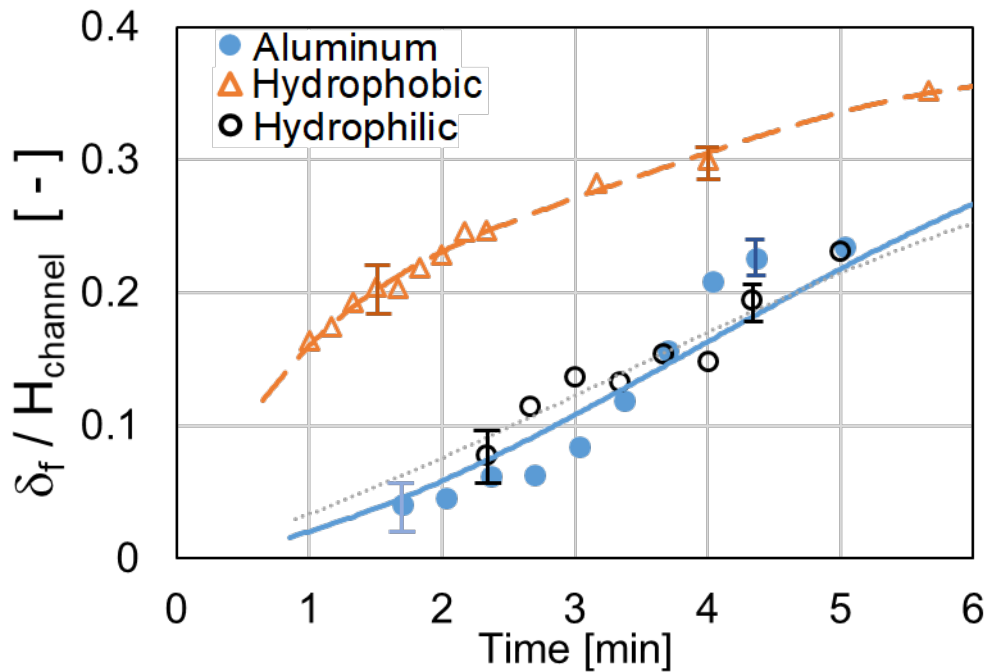


Figure 36: Frost thickness vs. time for all surfaces (coatings) during the nitrogen displacement tests - Frost thickness during the initial early frost nucleation stage (Heat Flux of 1300-1500 W/m², T_s = -15 °C, T_{a,in}= 5°C, Humidity inlet of 80 % R.H., Flow Rate of 8.5 m³/h)

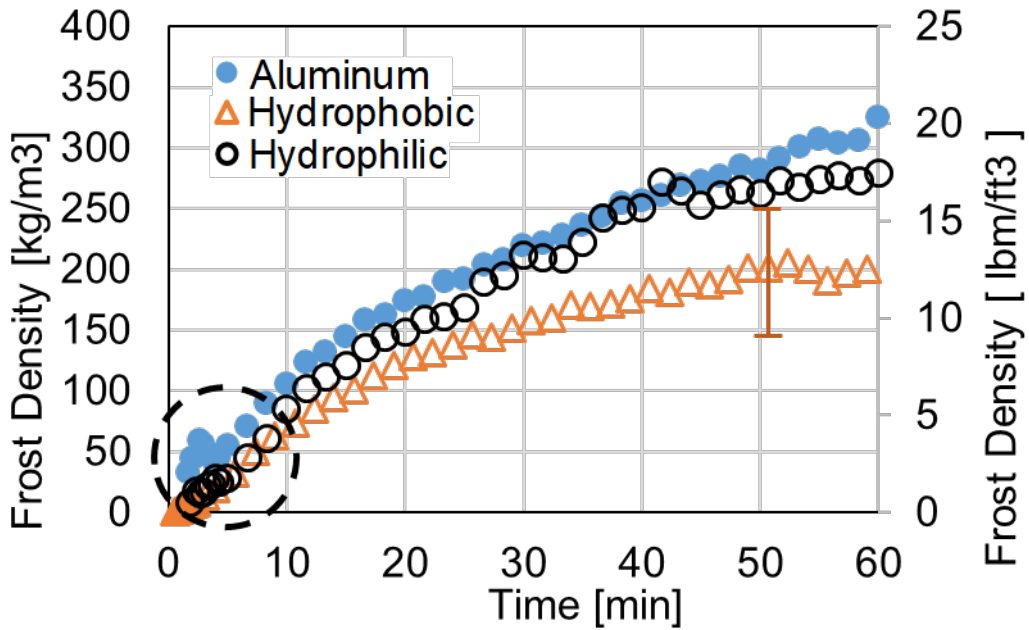


Figure 37: Frost density vs. time for all surfaces (coatings) during the nitrogen displacement tests - Frost density during the entire test period (Heat Flux of 1300-1500 W/m², T_s = -15 °C, T_{a,in} = 5°C, Humidity inlet of 80 % R.H., Flow Rate of 8.5 m³/h)

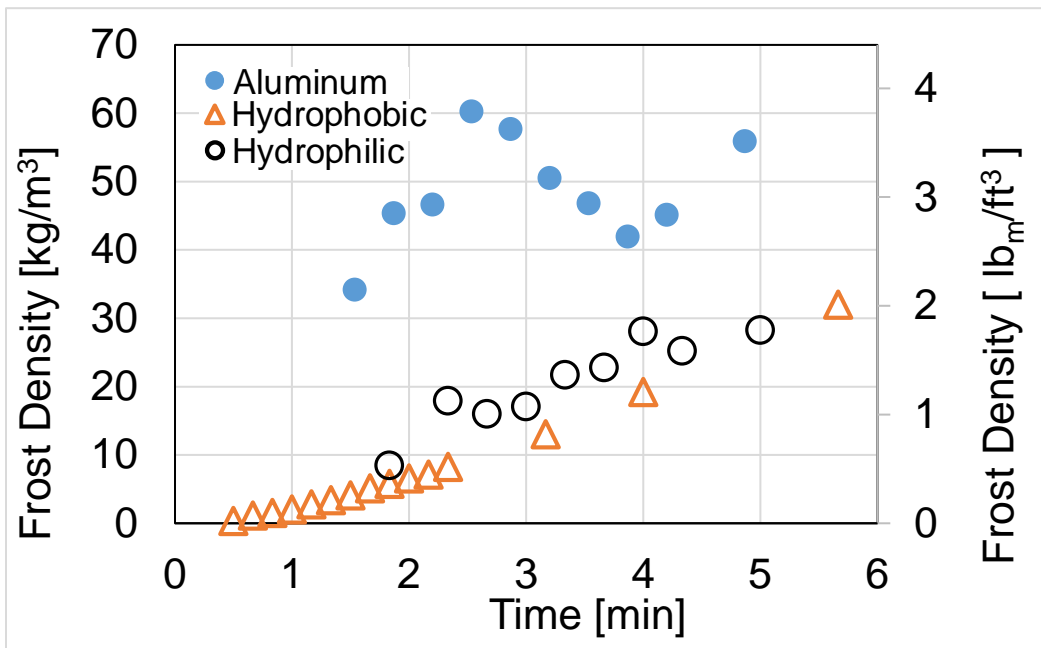


Figure 38: Frost density vs. time for all surfaces (coatings) during the nitrogen displacement tests - Frost density during the initial early frost nucleation stage (Heat Flux of 1300-1500 W/m², T_s = -15 °C, T_{a,in}= 5°C, Humidity inlet of 80 % R.H., Flow Rate of 8.5 m³/h)

Figure 37 provides an example of the frost surface temperature as a function of time for each surface during the nitrogen displacement tests. The frost surface temperatures were very similar to each other until about forty minutes into the tests. Then, the temperature dropped for the hydrophobic surface, but then began to climb again toward the end of the test. This frost temperatures drop was likely due to melting and refreezing of the very top of the frost layers. As the frost melted, the liquid water seeped into the frost layer and refroze, providing higher density and thermal conductivity of the frost layer. This resulted in higher heat conduction and lower temperature of the frost surface. Then, as frost started to grow on the top surfaces again, the temperature began to increase. This behavior was observed for the hydrophobic surface, it was repeatable.

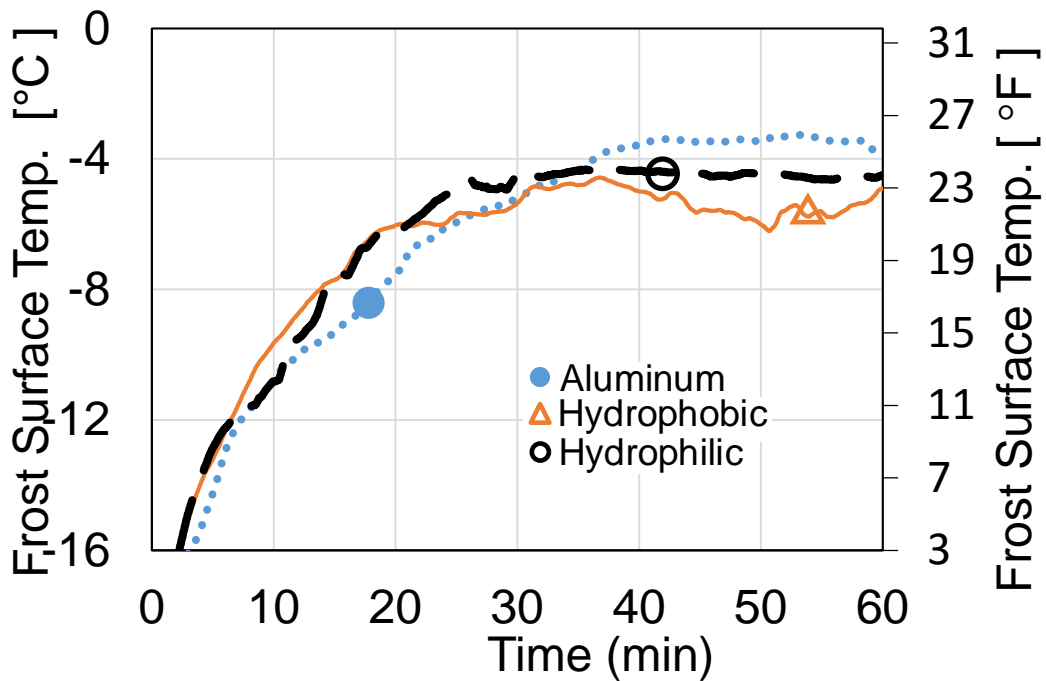


Figure 39: Time dependent variables for the surfaces (coatings) during the nitrogen displacement tests - Frost surface temperature vs. time (Heat Flux of 1300-1500 W/m², T_s = -15 °C, T_{a,in} = 5°C, Humidity inlet of 80 % R.H., Flow Rate of 8.5 m³/h)

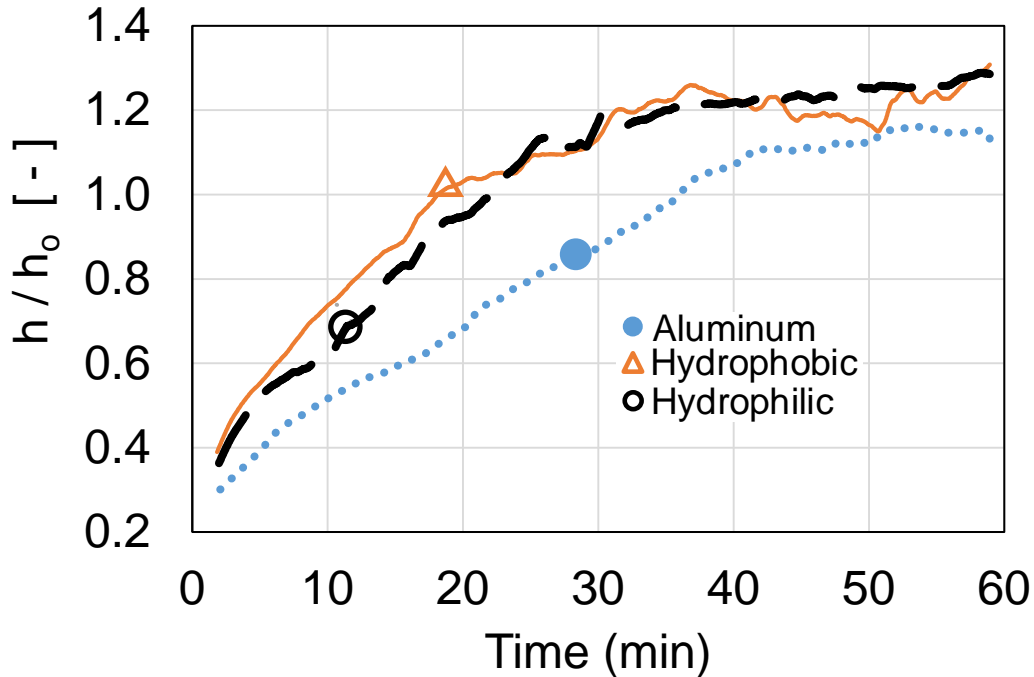


Figure 40: Time dependent variables for the surfaces (coatings) during the nitrogen displacement tests - Air-side convective heat transfer coefficient (normalized) vs. time (Heat Flux of 1300-1500 W/m², T_s = -15 °C, T_{a,in} = 5°C, Humidity inlet of 80 % R.H., Flow Rate of 8.5 m³/h)

Figure 38 shows the airside convective heat transfer coefficient for each surface during the nitrogen displacement tests. The heat transfer coefficients were calculated based on actual instantaneous heat fluxes at the test plate surface, air inlet dry bulb temperature, and frost surface temperatures. The data were normalized with respect to $h_0 = 120 \text{ W/m}^2\text{-K}$ measured during steady-state wet tests. During frost nucleation, the heat transfer coefficients were about 60 to 70% lower than that of steady state wet-test value. They also remained quite low during the first six to ten minutes (i.e., during the droplet growth and ice crystal growth phases).

During frost accretion, the heat transfer coefficients increased over one because the airflow rate was constant and, as frost built up, it reduced the free flow area. Thus, the local air velocity

immediately adjacent the top of the surfaces increased significantly. The heat transfer coefficient of the aluminum surface was the lowest of all of them.

8.2 Frost characteristics during pull-down tests

Table 4 summarizes the radius of the ice beads, the freezing time, the freezing duration, and the period it took for the frost thickness to block the cross-sectional area of the channel until the pressure drop across the air flow above the test plate reached 87 Pa (0.35 in. H₂O) during the pull-down tests. Recall that in this mode of operation, the surface temperature of the test plates decreased gradually from initial temperature of 5 °C, which were in thermal equilibrium with the airflow above the plates, down to -15 °C. During this pull-down period, water vapor condensed on the surfaces and large droplets (with respect to those observed in the nitrogen displacement tests) formed before turning into ice beads.

Table 4: Frost variables during the pull-down tests for the all surfaces (air at 5 °C and 78-80 % R.H., 8.5 m³/h)

Surface Coating Type	Frozen Droplet Radius (mm)	Freezing Time (min, sec)	Freezing Duration (min, sec)	Time until $\Delta P = 0.35$ in. w.c. (min)
Fine-finished Aluminum ($\theta \approx 75^\circ$)	0.135	12m 53s – 14m 14s	1m 4s	~65 (± 30 s)
Hydrophobic ($\theta = 110$ - 116°)	0.139	12m 52s	2m 12s	~45 (± 30 s)
Hydrophilic ($\theta = 19$ - 29°)	0.0985	11m 36s	52s	~57 (± 30 s)

In Table 4, the freezing time was defined as the time elapsed between turning on of the thermoelectric coolers for cooling down the test plates and the midpoint of the droplet freezing process. The freezing duration was defined as the number of minutes and seconds it took for all the droplets in the viewing window to appear frozen. Hydrophilic surface froze very quickly, in only about 11 minutes and 36 seconds. The radius of the frozen droplets was dependent on the

freezing time, which was in turn a function of the type of coating. Even though droplets on hydrophilic surfaces appeared flat and more “spread out,” the frozen droplets were much smaller than any other droplets measured on the other surfaces. Ice nucleation on the hydrophilic surface occurred quickly, leaving less time for disc-like shaped water droplets to continue to grow in the radial and vertical directions before freezing.

Figure 39 and Figure 40 show frost thickness versus time for all surfaces during the pull-down tests. As frost started gradually to grow on the top of the iced beads, A range for the freezing time is presented for the aluminum surface because of the variability of the freezing time in repeated frosting tests at about one month apart.

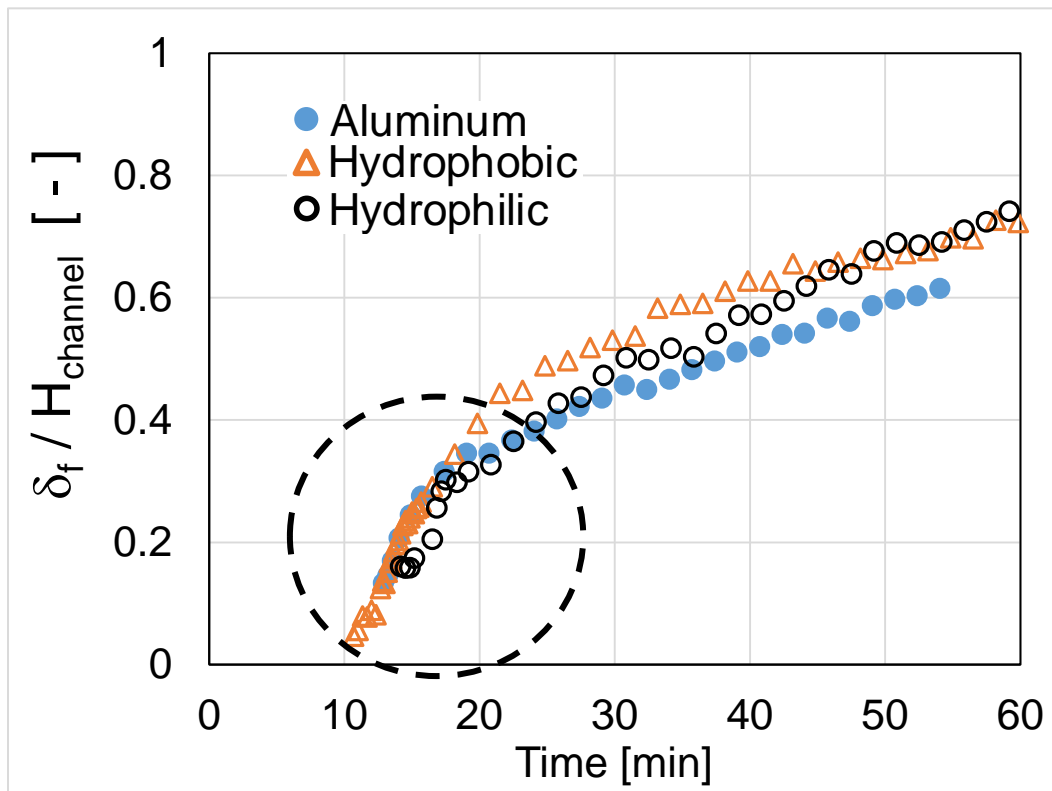


Figure 41: Frost thickness vs. time for all surface (coatings) during the pull-down tests - Frost thickness during the entire test period (Heat Flux of 1300-1500 W/m², T_s = -15 °C, T_{a,in}= 5°C, Humidity inlet of 80 % R.H., Flow rate of 8.5 m³/h)

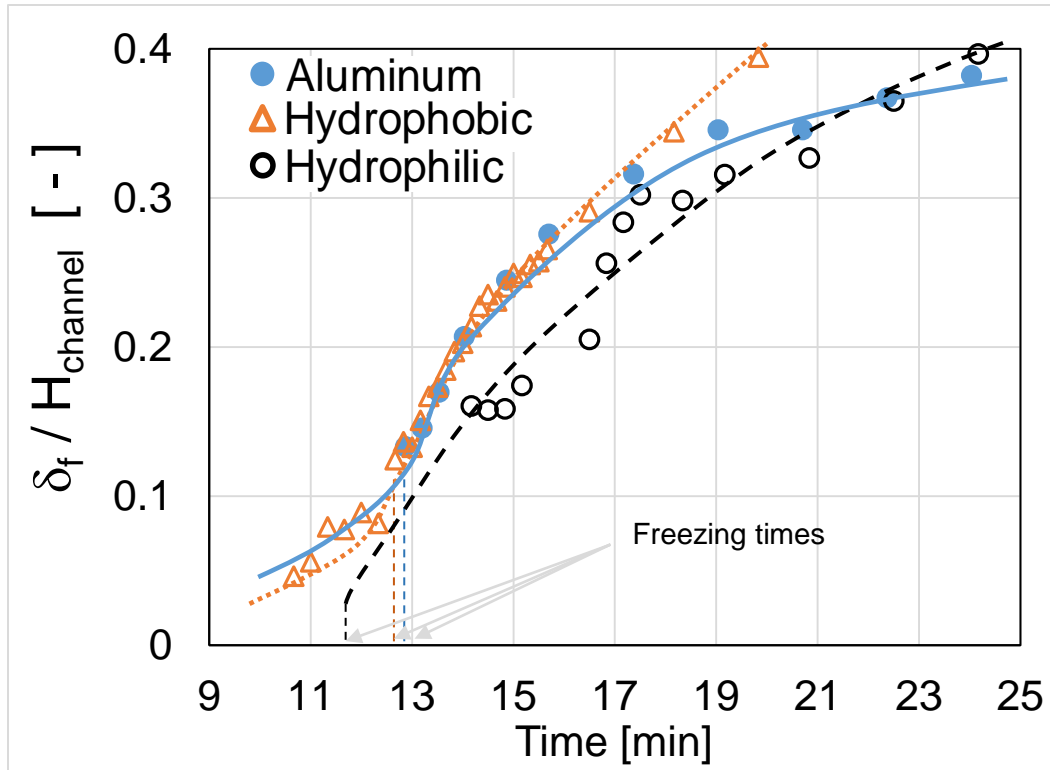


Figure 42: Frost thickness vs. time for all surface (coatings) during the pull-down tests -Frost thickness during the transitions from droplets to ice beads, and to frost growth (Heat Flux of 1300-1500 W/m², T_s = -15 °C, T_{a,in}= 5°C, Humidity inlet of 80 % R.H., Flow Rate of 8.5 m³/h)

Figure 39 gives thickness data for the entire pull-down test period and the trends are clearly not linear. They followed “S” shaped like profiles and Figure 40 zooms out across the 15 minutes period during the transitions of droplets to ice beads, to crystals growth, and to initial frost accretion on the top of the ice beads. These phase changeovers are indicated in Figure 40 by variations of the slope of the frost thickness data when plotted vs the elapsed time: the first slope change shows the transition from droplets/iced beads to crystal growth phase and the second slope change represent the switch from crystal growth phase to frost growth phase. After this phase changeover, frost accretion during the remaining frost growth phase increased almost linearly with time. The wettability characteristics of the surface coatings affected the elapsed time of the phase changeovers and the thresholds of the frost thickness at the switch to the frost growth phase.

Hydrophobic surface had early transitions and high thresholds of the frost thickness before switching to the frost growth phase. This result was due to the presence of large droplets on the surfaces before the droplets froze into ice beads. Aluminum surface had an early transition and a low threshold. The changeovers were not measurable for the hydrophilic surface for which the freezing time was 11 minutes and 36 seconds. For hydrophilic surface, the droplets were too small to be detected with our HRCCD camera. The profile of frost growth in Figure 40 for hydrophilic surface is indicated with a black dashed line and circle data points.

Figure 41 and Figure 42 depicts frost density versus time for all surfaces during the pull-down tests. The evolutions of the frost density with time were similar: they started high, decreased to a minimum value during the transitions periods from crystal growth to frost growth phases, and then they started to increase again during the frost growth phase. A zoom out of the frost densities during the phase changeover period is in Figure 42. The initial high density was because droplets grew for some time before they froze. These liquid droplets were more dense and compact than typical porous solid frost, leading to large masses but associated small volumes (i.e., large initial densities). As frost crystals developed on the frozen ice beads, they contributed to decrease the average frost density. This effect continued until minimum values of density were observed. Then, the frost behaved as solid that grows and become less and less porous. In pull down tests, the hydrophobic surfaces had lowest range of densities. While the trends of the density data shown in Figure 41 and Figure 42 are, according to the authors' opinion, reasonable, caution should be used during comparison among the actual values from the different surface wettability cases. Due to transient nature of the pull-down tests and due to the repeatability of the measurements, the experimental uncertainty on the density data of Figure 42 could be quite high. Further investigation and additional tests are needed to confirm the repeatability of the results shown in Figure 42.

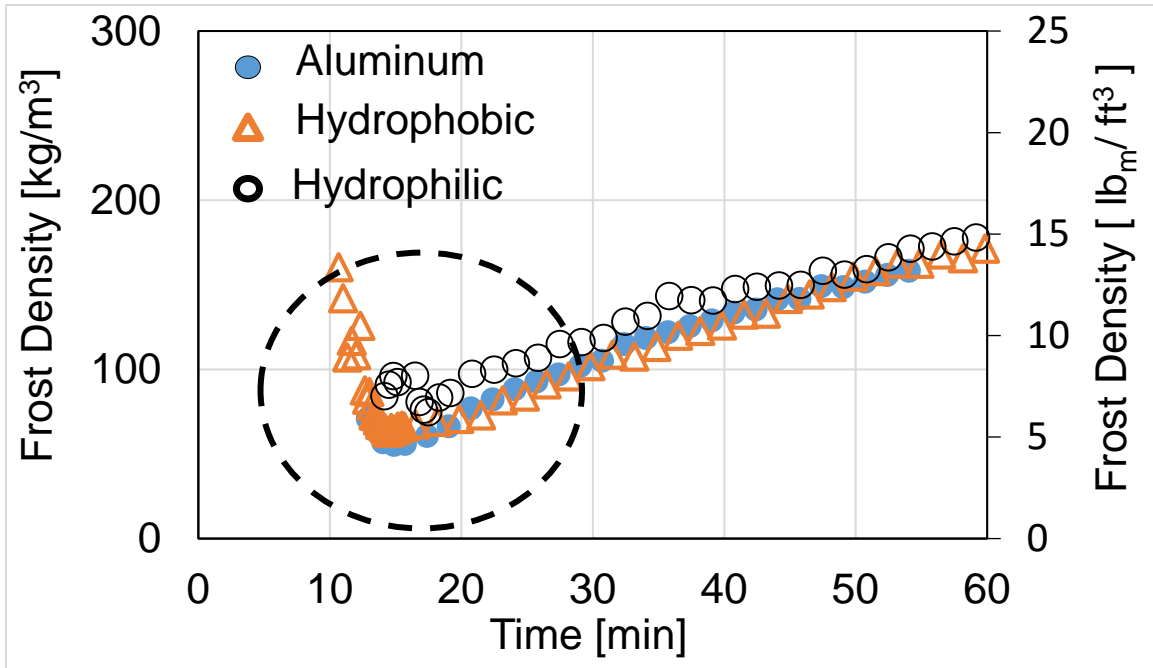


Figure 43: Frost density vs. time for all surfaces during the pull-down tests - Frost density during the entire test period (Heat Flux of 1300-1500 W/m², T_s = -15 °C, T_{a,in} = 5°C, Humidity inlet of 80 % R.H., Flow Rate of 8.5 m³/h)

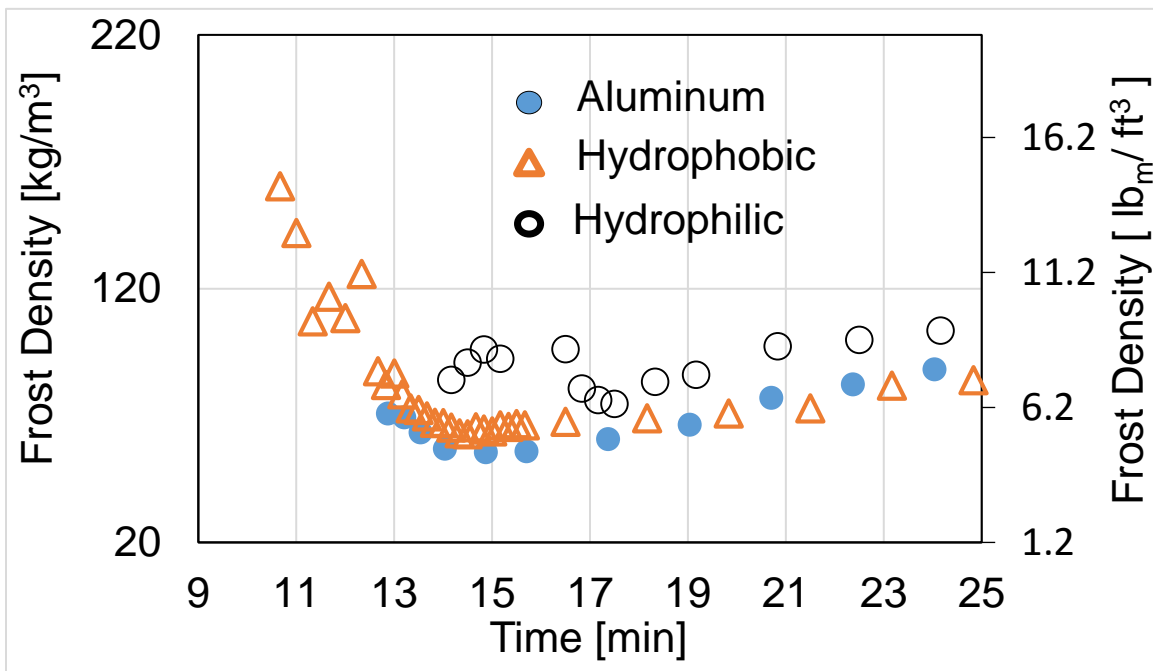


Figure 44: Frost density vs. time for all surfaces during the pull-down tests - Frost density during the transitions from droplets to ice beads, and to frost growth (Heat Flux of 1300-1500 W/m², T_s = -15 °C, T_{a,in} = 5°C, Humidity inlet of 80 % R.H., Flow Rate of 8.5 m³/h)

8.3 Effect of test conditions on hydrophobic, hydrophilic and uncoated surfaces

Test conditions may affect the freezing time and frost growth rate. To explore these effects, different test conditions were used. Table 5 lists the test conditions and the legend of the results reported in Figure 43 to Figure 54 is given in the top rows.

Table 5: Test Conditions and Legend Number for Figure 43 to Figure 54

Test Conditions No. →	No. 1	No. 2	No. 3	No. 4
Surface Temperature, °C (°F)	-3.25 (27)	-7.11 (19)	-3.04 (27)	-3.43 (27)
Relative Humidity, %R.H.	80	80	95	80
Air Temperature, °C (°F)	5 (41)	5 (41)	5 (41)	5 (41)
Air Volume Flow Rate, m ³ /h (cfm)	8.5 (5)	8.5 (5)	8.5 (5)	4.25 (2.5)

Figure 43 to Figure 46 present the results from test conditions No. 1. Frost mass accumulated on the test plate with linear trends, and the hydrophilic surface accumulated slightly less mass after 60 minutes. This could be due to the slightly higher frost surface temperature observed for the hydrophilic surface, as indicated in Figure 44. The frost surface temperatures were very similar to each other until about forty minutes into the tests. Then, the frost temperature gradually climbed for the fine-finished aluminum surface and the hydrophilic surface. The “spikes” in the measured apparent frost temperatures were due to melting and refreezing of the top of the frost layers. As the frost melted, the liquid water seeped into the frost layer and re-froze, providing higher density and thermal conductivity of the frost layer. This resulted in higher heat conduction and lower temperature of the frost surface. Then, as frost started to grow on the top surfaces again, the temperature began to increase. This behavior was observed for the aluminum and hydrophobic surfaces. It was also observed for the hydrophilic surface but with much lower magnitude. Figure 45 shows the airside convective heat transfer coefficient for each surface. The heat transfer coefficients were calculated based on actual instantaneous heat fluxes at the test plate

surface, air inlet dry bulb temperature, and frost surface temperatures. The data were normalized with respect to $h_0 = 120 \text{ W/m}^2\text{-K}$ measured during steady-state non-freezing wet tests. During water vapor condensation and droplet growth, i.e., during the initial part of phase III (see Figure 19), the heat transfer coefficients were about $120 \text{ W/m}^2\text{-K}$ for all three surfaces. From this observation, we concluded that the contact resistance of the test plates with the metal block heat flux meter were also similar and comparable to each other during the frost tests. As droplets began to turn into ice beads, large fluctuations of the heat transfer coefficient were observed. Then, as crystals started to grow on the top of the ice beads, the heat transfer coefficients gradually increased because of the augmented surface roughness created by frost during its nucleation. It should be noticed that during frost accretion, the normalized heat transfer coefficients exceeded 1.0 because the airflow rate was constant and, as frost built up, it reduced the free flow area. Thus, the local air velocity immediately adjacent to the top of the surfaces increased significantly. Another clear indication of the frost nucleation is shown in the airside pressure drop profiles in Figure 46. The change of slope in these profiles, coincide with the spikes in heat transfer coefficients and, of course, with the spikes in the measured frost surface temperatures in Figure 44. The hydrophilic surface froze very quickly, in only about 22 minutes. The radius of the frozen droplets was dependent on the freezing time, which was in turn function of the type of coating. Even though droplets on hydrophilic surfaces appeared flat and more “spread out”, the frozen droplets were much smaller than any other droplets measured on the other surfaces. Ice nucleation on the hydrophilic surface occurred quickly, leaving less time for disc-like shaped water droplets to continue to grow in the radial and vertical directions before freezing. On the contrary, the freezing and the droplets radius were high for the hydrophobic surface. Large mass and volume of the droplets on this surface were observed before they turned into ice beads. Interesting, the aluminum surface had freezing time in between hydrophilic and

hydrophobic and its frost surface temperature resembled the one observed for the hydrophilic surface.

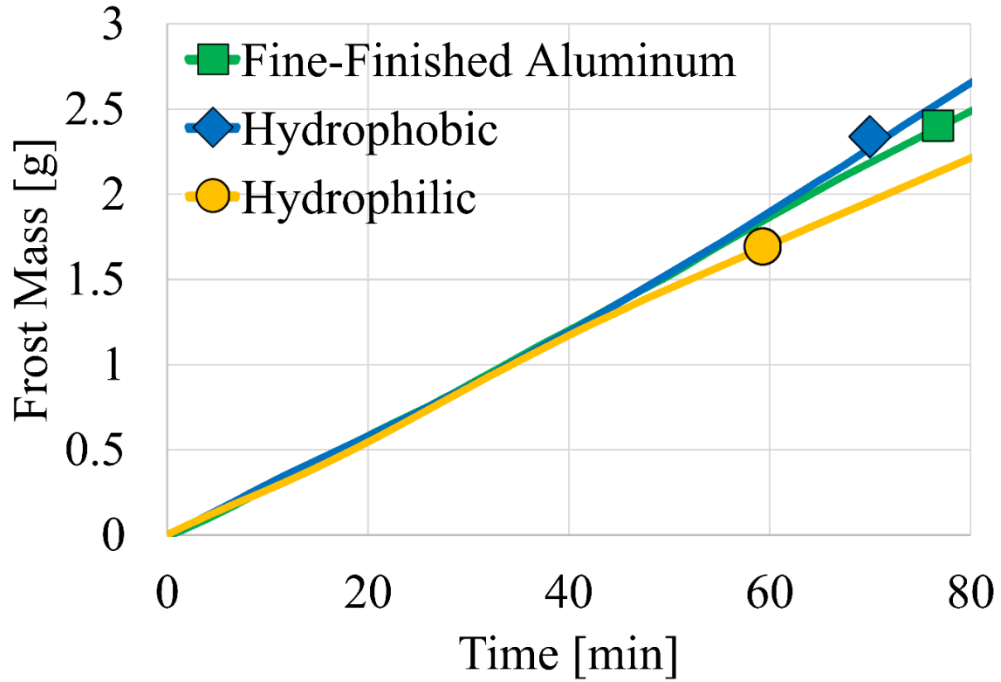


Figure 45: Test results from test conditions No. 1 - Frost mass vs. time

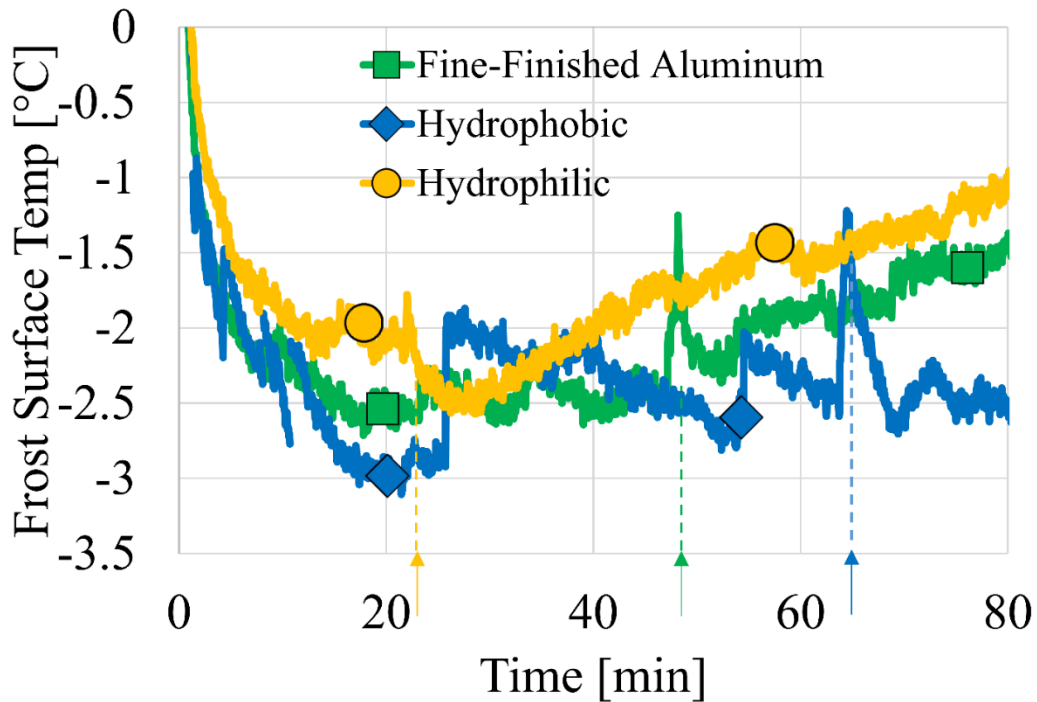


Figure 46: Test results from test conditions No. 1 - Surface temperature vs. time

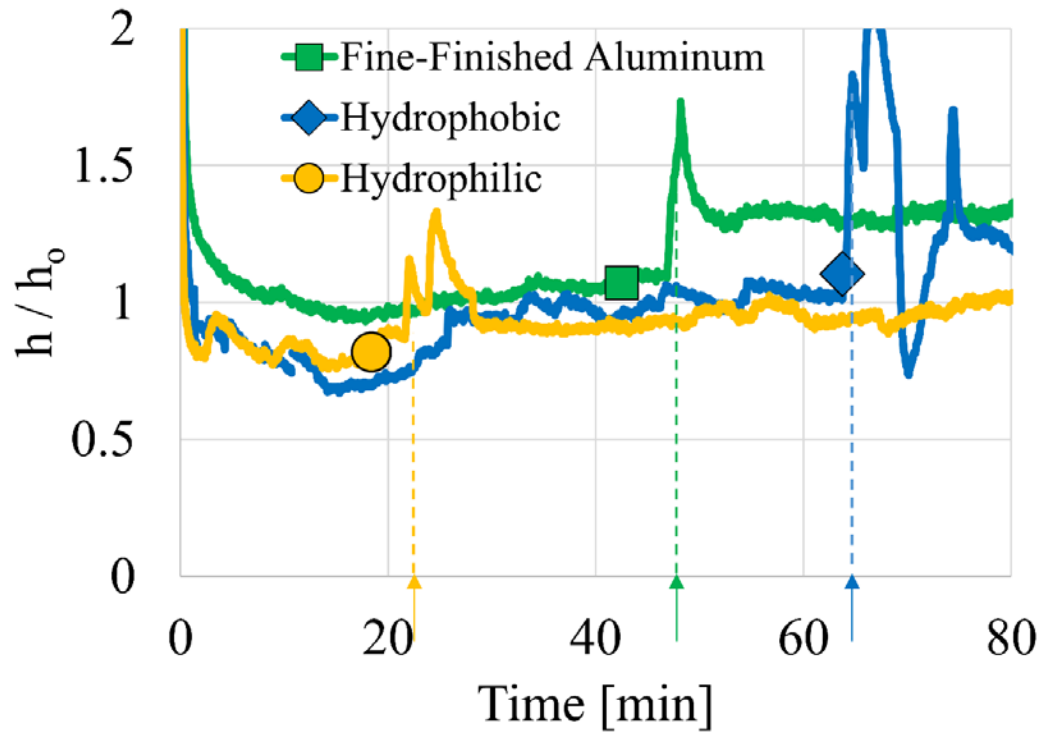


Figure 47: Test results from test conditions No. 1 - Normalized heat transfer coefficient vs. time ($h_0 = 120 \text{ W/m}^2\text{-K}$)

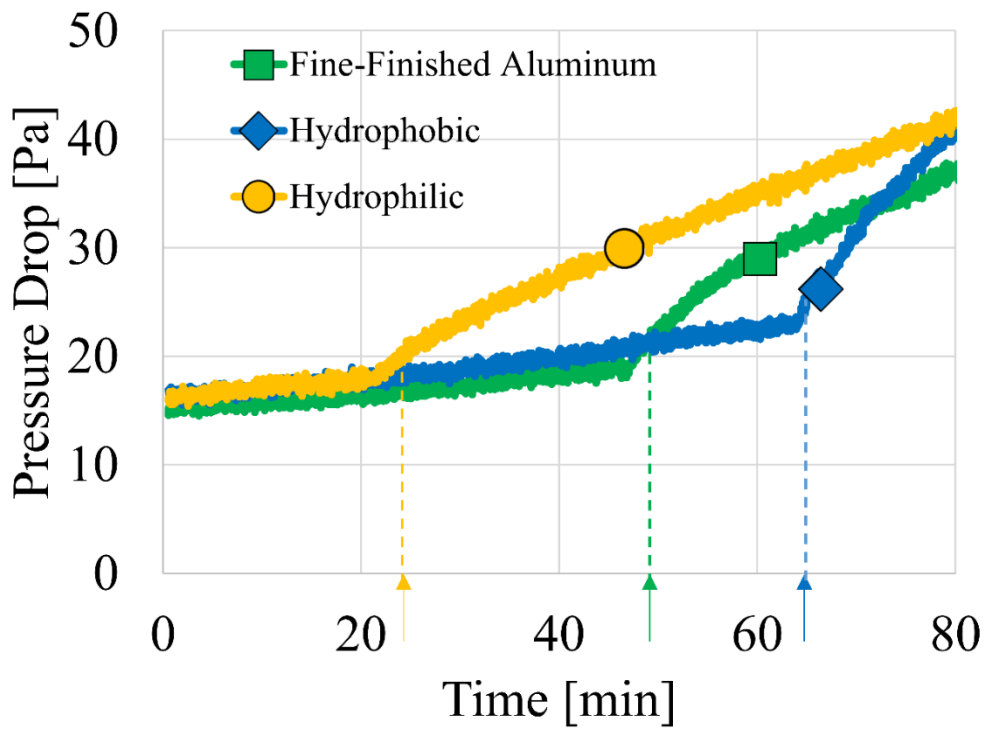


Figure 48: Test results from test conditions No. 1 - Pressure drop vs time

Figure 47 presents frost thickness at the leading edge of the test plates as a function of time for all surfaces (aluminum, hydrophobic, and hydrophilic) for the test conditions No. 1. The frost thickness, δ_f , was normalized with respect to the height of the channel, $H_{\text{channel}} = 4 \text{ mm}$ (0.16 in), of the cross section of the rectangular duct available to the airflow right above the test plates. There was a rapid increase of frost thickness during frost nucleation, due to the crystals growing on the top of the ice beads. The thickness trends for the aluminum and hydrophilic surfaces were similar. They both had significantly lower thickness during the initial droplet growth and frost nucleation period. Then, the frost thickness increased slowly and with almost constant slope for the remaining of the frosting period. The surface characteristics affected the time and the initial thickness of the frost after the droplets froze on the test plates. This was also the starting point for the frost growth phase V (refer to Figure 19). The hydrophobic coating surface had the highest thickness and this was consistent with the formation of large droplets that took very long to freeze. Figure 48 shows the average frost density as a function of time for all surfaces and the data were normalized with respect to the density of the water at 25°C, that is, ρ_o was 1000 kg/m³. The density for the aluminum surface was the highest and showed large fluctuations during the early stage of frost growth. hydrophilic coating had small range of densities because the droplets froze earlier than the other two surfaces. Thus, the mass accumulated on the hydrophilic surface during incipient frost was quite low. The frost density gradually increased during the frost growth. Error bars are reported for three representative points in the figures and they account for the overall experimental error of the measurements.

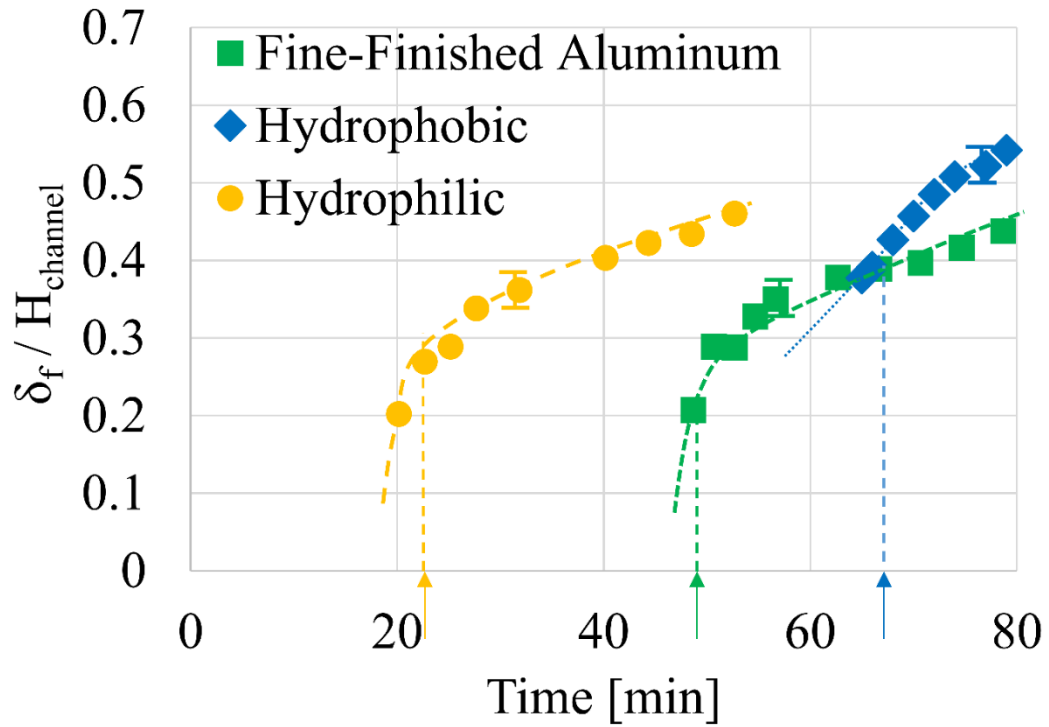


Figure 49: Frost thickness vs time for test conditions No. 1

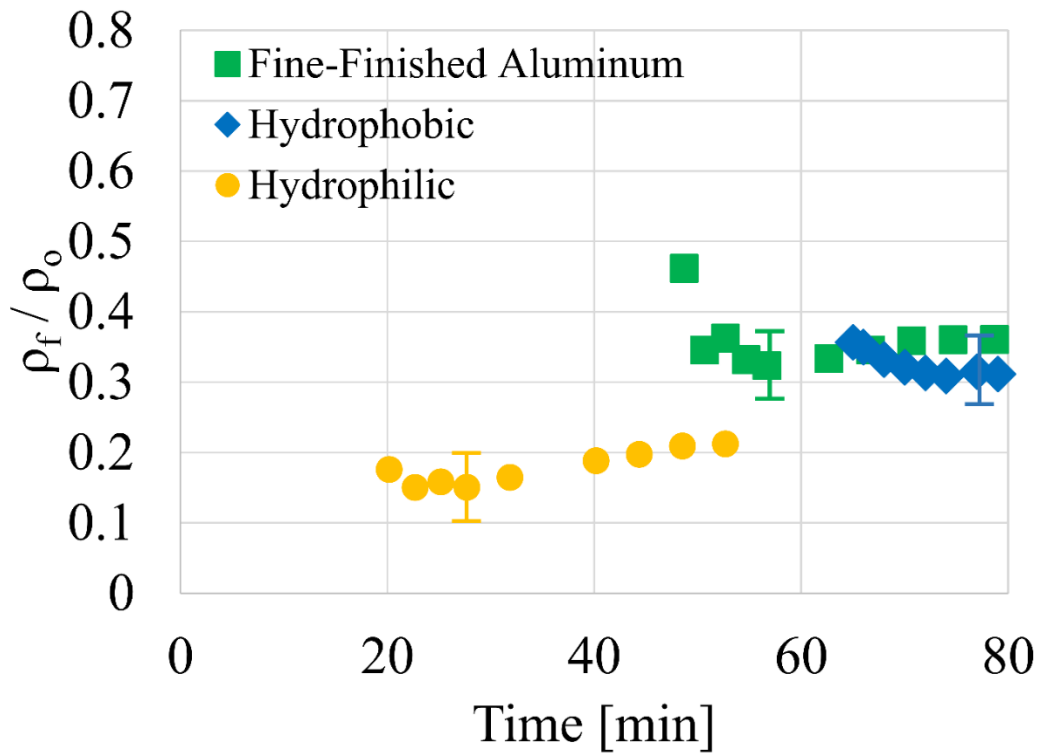


Figure 50: Density vs time for test conditions No. 1

Table 6 summarizes the radius of the ice beads, the freezing time, the freezing duration, and the period it took for the frost thickness to block the cross sectional area of the channel until the pressure drop across the air flow above the test plate reached 87 Pa (0.35 in H₂O) during the tests. The freezing time was defined as the time elapsed between time zero in which the air flow rate on the top of the test plate was reestablished after the nitrogen and the midpoint of the droplet freezing process. The freezing duration was defined as the period, in seconds, it took for all the droplets in the viewing window to appear frozen. Right after freezing, the iced droplets on the hydrophobic surface were the largest and those on the hydrophilic surface were the smallest. The freezing time for the hydrophobic surface was about 65 minutes, that is, the longest time to freeze among all the surfaces. hydrophilic surface froze very quickly, in only about 22 minutes. The radius of the frozen droplets was dependent on the freezing time, which was in turn function of the type of coating. Even though droplets on the hydrophilic surface appeared flat and more “spread out”, the frozen droplets were much smaller than any other droplets measured on the other surfaces. Thus, the frost blockage time for the hydrophilic surface was higher than that for the hydrophobic surface because of the very thin and more porous (i.e., less dense) frost layer initially formed on the hydrophilic surface.

Table 6: Frost characteristics for test No. 1 conditions (air at 5 °C and 80 % R.H., 8.5 m³/h)

Surface Coating Type	Frozen Droplet Radius (mm)	Freezing Time (min)	Freezing Duration (s)	Time until $\Delta P = 0.35$ in. w.c. (min)
Fine-Finished Aluminum ($\theta \approx 75^\circ$)	1.07	49 (± 0.2)	144	161 (± 1.5)
Hydrophobic ($\theta = 110-116^\circ$)	1.74	65 (± 0.2)	62	140 (± 1.0)
Hydrophilic ($\theta = 19-29^\circ$)	0.81	22 (± 0.2)	30	157 (± 1.1)

Figure 49 and Figure 50 present the results from test conditions No. 2 in which the test

plate surface temperature was low. The nucleation of frost occurred earlier when the test plate temperature decreased from -3 to -7°C . For the aluminum and hydrophobic surface, the crystal growth phase was also quicker, which is shown by flattened profiles of the “S” during the crystal growth period. In other words, the frost growth as soon as the droplets froze. A marked dependence of the freezing was observed for aluminum, in which freezing time decreased from 49 minutes to 5 minutes, and for the hydrophobic surface, in which the freezing time decreased from 65 minutes to less than 15 minutes. The freezing time for the hydrophilic surface did not vary appreciably if the test plate temperature decreased from -3 to -7°C . As result of early frost nucleation, the density of the frost for Aluminum also decreased markedly from ρ/ρ_0 of 0.35 (see Figure 48 at 49 minutes) to ρ/ρ_0 less than 0.1 (see Figure 50 at 9 minutes). Much smaller variations of the frost density were observed for the hydrophilic surface because the freezing time was not affected. On the other hand, early freezing but similar initial frost density were observed for the hydrophobic surface. This was because the droplets that turned into ice beads were smaller, resulting in lower thickness but also less water mass accumulated on the hydrophobic surface at the frost nucleation time.

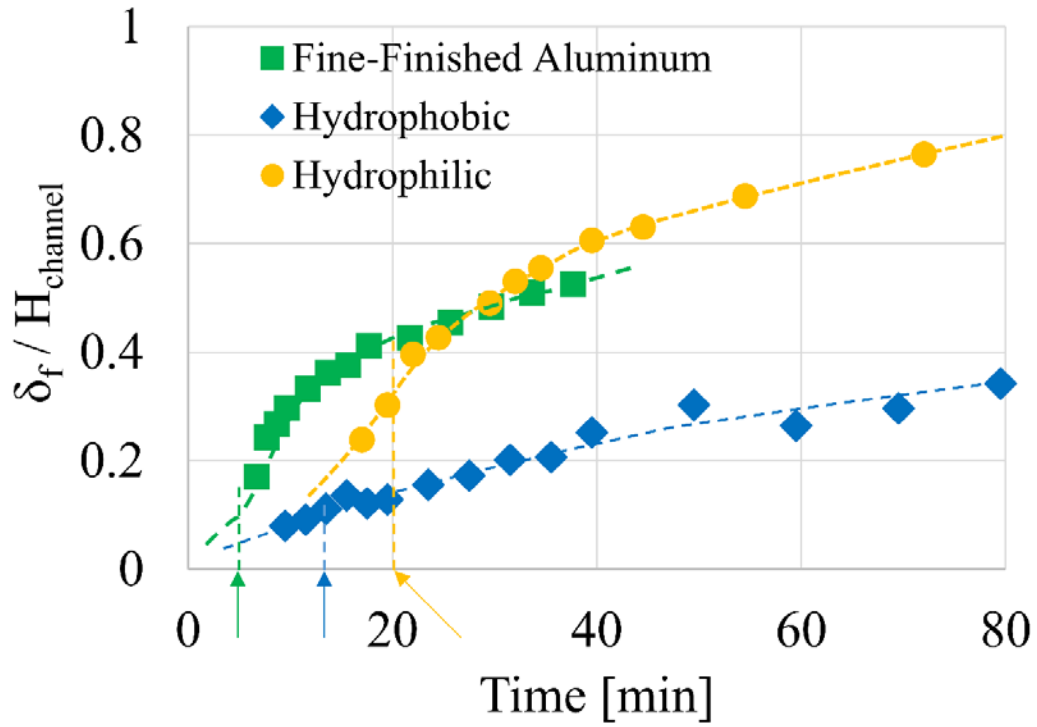


Figure 51: Frost thickness vs time for test conditions No. 2

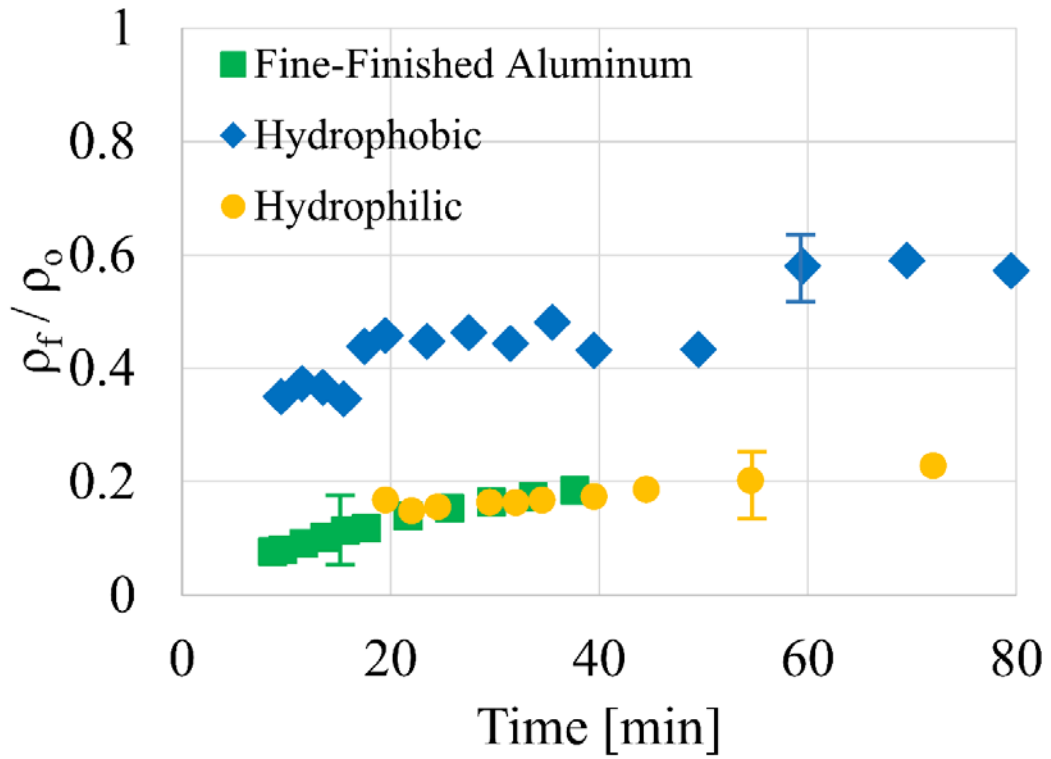


Figure 52: Density vs time for test conditions No. 2

Figure 51 and Figure 52 present the results from the test conditions No. 3, in which the relative humidity was quite high and at about 95% R.H. When comparing the results with that of 80% R.H. (see Figure 47 and Figure 48), we observed early frost nucleation for the aluminum and for the hydrophobic surfaces. The freezing time decreased with increase of relative humidity: significant reductions in freezing time were observed for the aluminum and hydrophobic surfaces and a slight reduction of few minutes were measured for the hydrophilic surface. The frost densities in Figure 52 were similar in magnitude to those of Figure 48 but their order was inverted with respect to the elapsed time.

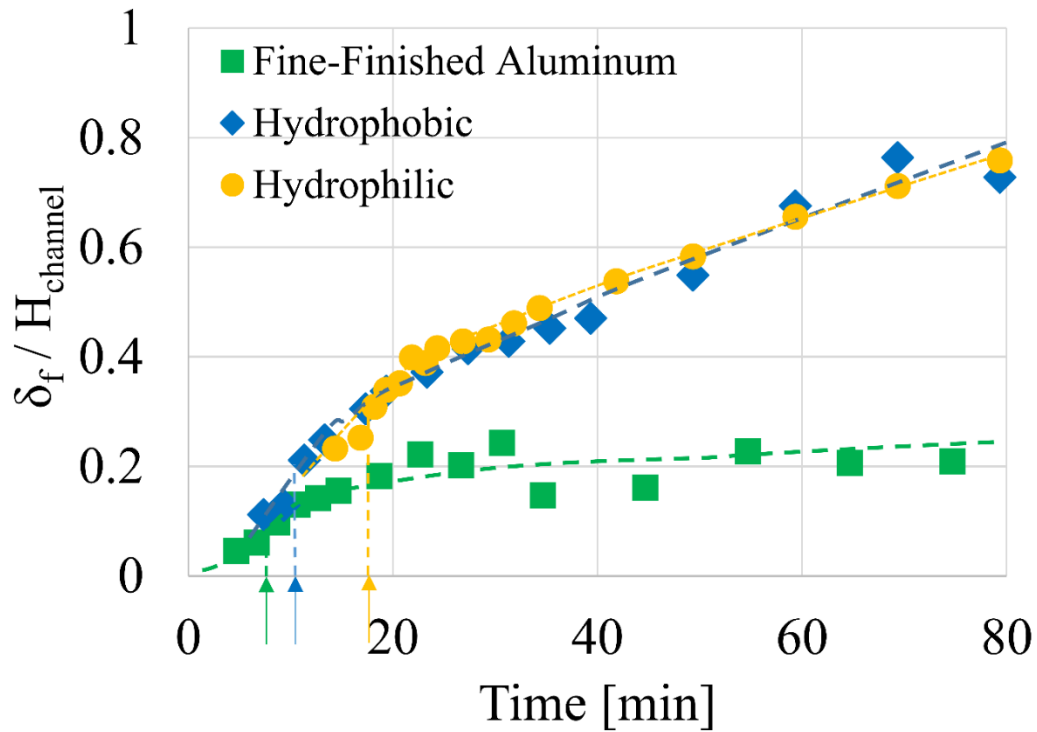


Figure 53: Frost thickness vs time for test conditions No. 3

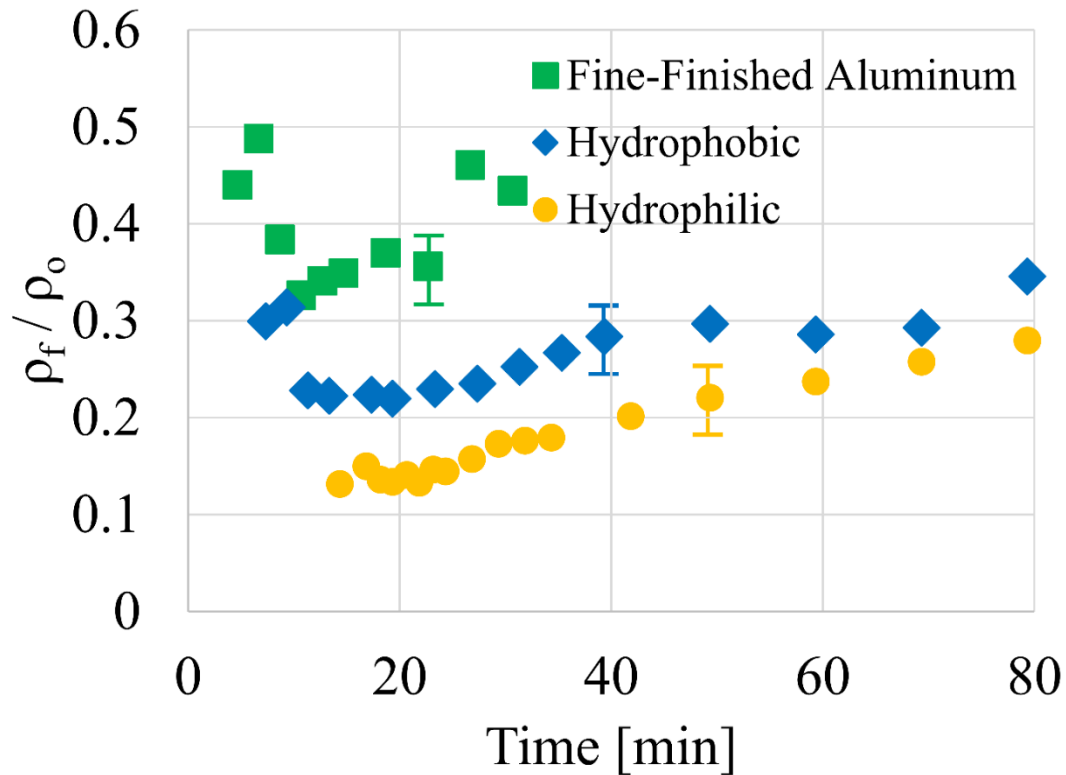


Figure 54: Density vs time for test conditions No. 3

Figure 53 and Figure 54 present the results from test conditions No. 4, in which the air volume flow rate was about a half with respect to the other tests. This reduction of air approaching velocity tremendously increased the freezing time for all surfaces. For example, for hydrophilic surface the freezing time increase from 22 minutes at $8.5 \text{ m}^3/\text{h}$ (5 cfm) to over 80 minutes when the air flow rate was $4.25 \text{ m}^3/\text{h}$ (2.5 cfm). The ‘delay’ was created by a lower heat transfer rate and a slower mass diffusion process of the water vapor from the air in to the crystals. In addition, the ice beads on the hydrophilic surface increased in diameter when the approaching air flow rate was reduced by half. The densities for the low air flow rate test conditions are summarized in Figure 54.

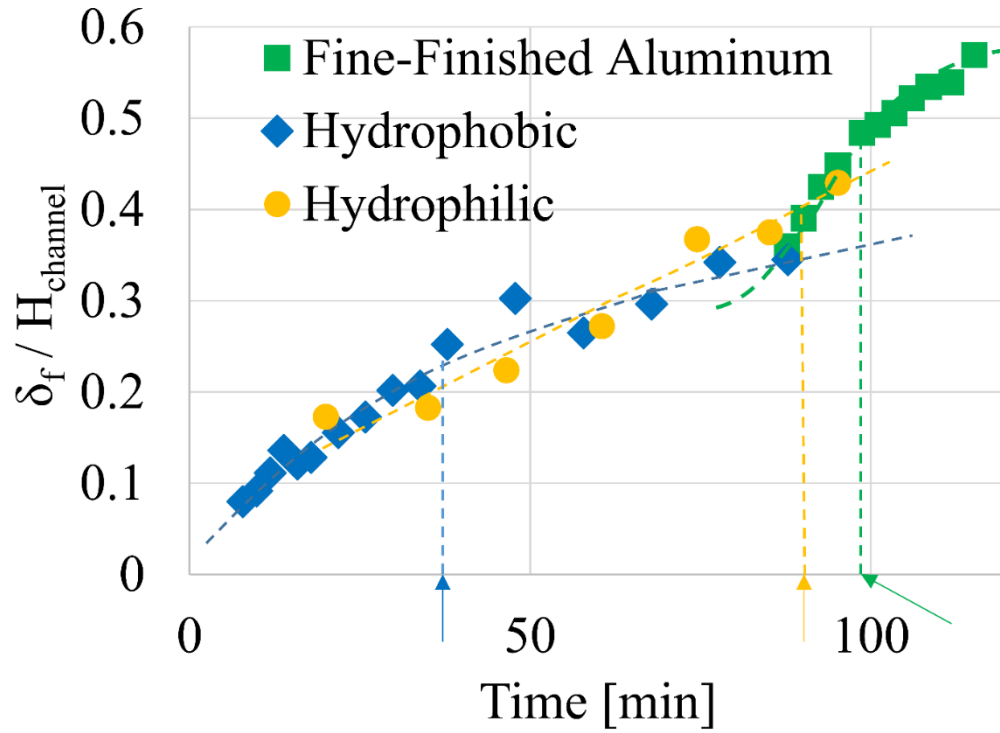


Figure 55: Frost thickness vs time for test conditions No. 4

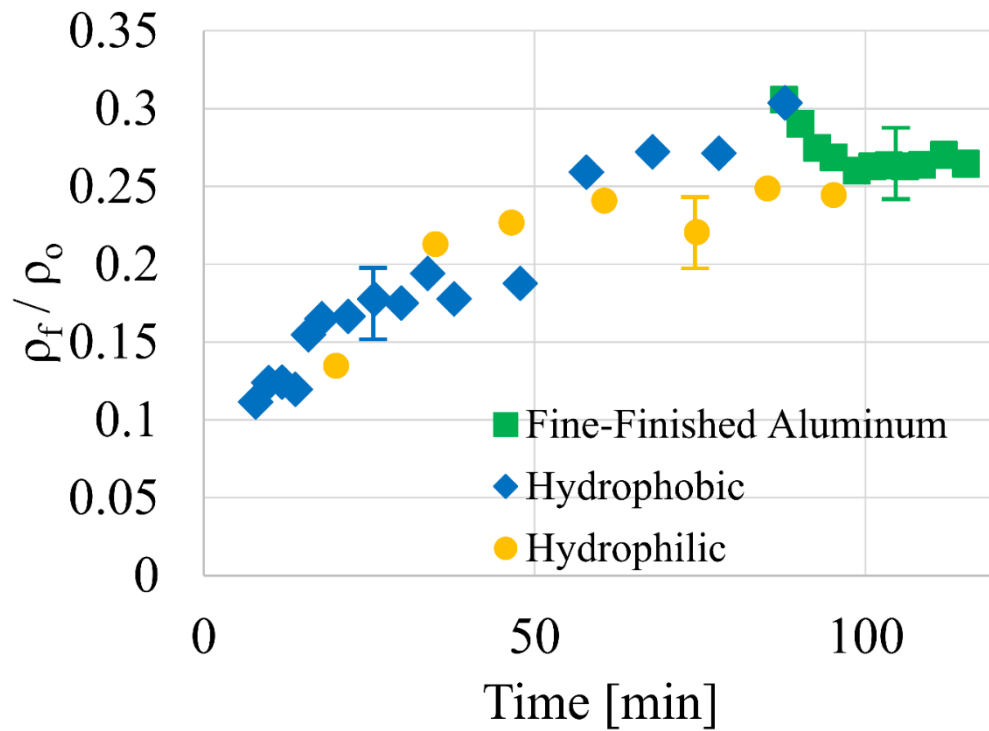


Figure 56: Density vs time for test conditions No. 4

8.4 Cycling tests

Table 7 summarizes the results from the cycling tests conducted on the fine finished aluminum surface, hydrophobic surface, and hydrophilic surface. The results show that the hydrophobic surface had the shortest (most frequent) cycle time and the hydrophilic surface had the longest (least frequent) cycle time. This suggests that the cycle duration increases with decreasing contact angle. Figure 55 shows an example of the pressure drop measured across the test section during an entire cycling test.

Table 7: Summary of cycle duration results from cycling tests

	Aluminum	Hydrophobic	Hydrophilic
Cycle 1 Duration (min)	75.9	81.6	91.2
Cycle 2 Duration (min)	68.5	86.0	83.4
Cycle 3 Duration (min)	74.8	72.0	87.8
Cycle 4 Duration (min)	80.5	64.9	87.3
Cycle 5 Duration (min)	83.7	67.1	67.0
Cycle 6 Duration (min)	69.3	66.4	51.9
Average of cycle 5 & 6 (min)	76.5	66.7	59.5

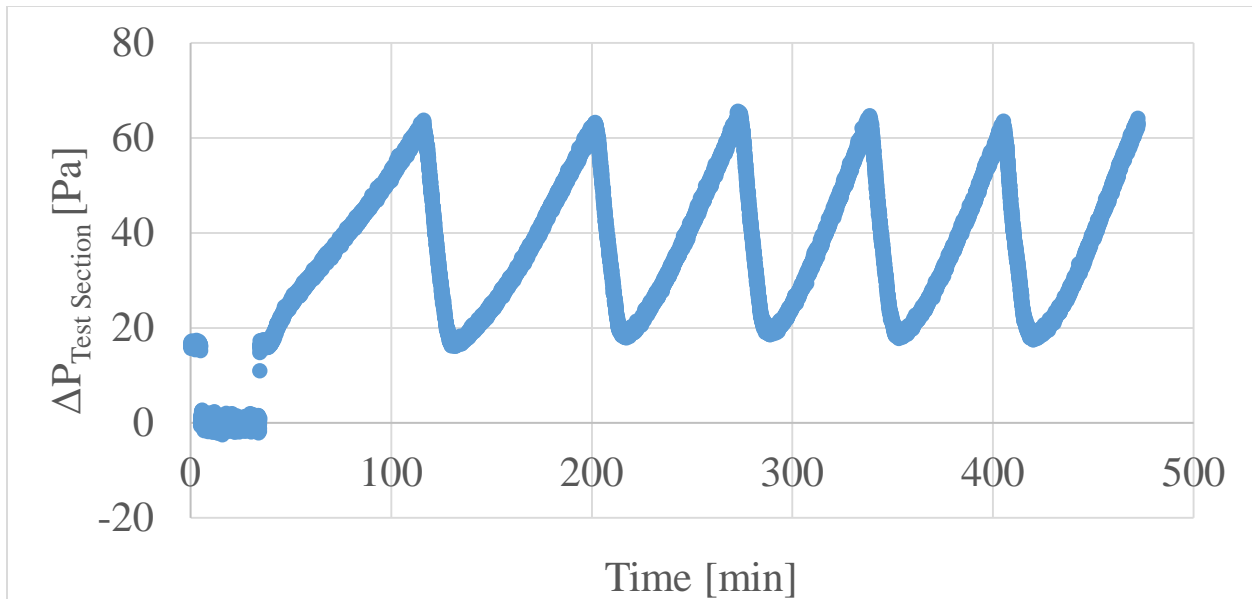


Figure 57: Example of pressure drop across test section for cycling test

Chapter 9: Conclusions

Frost formation is a phenomenon that decreases the performance and efficiency of heat exchangers. Surface coatings have the potential to be able to prevent or to hinder the negative effects that frosting has. Not only is it useful to know how surface coatings could affect heat exchanger performance, but the data from this thesis is also very important for the scientific community to help further understand the complexity and the behavior of frost.

In order to understand these surface coatings and their performance in frosting conditions, a new experimental test setup was designed, constructed and operated in order to facilitate these experiments. Testing conditions of the experiment were maintained by an assortment of equipment and sensors. Experimental procedures were developed to operate and maintain the test setup as well as to gather consistent and accurate test data. A new nitrogen displacement technique was developed for constant surface temperature tests.

This thesis demonstrates that the experimental setup was capable of gathering data for all three testing surfaces (aluminum, hydrophobic, and hydrophilic) including freezing time, droplet diameter, frost thickness, etc. The setup was used to investigate the effect that condition variables such as temperature, velocity, relative humidity, etc. had on the frost properties of these three plates.

During pull-down tests, water vapor condensed on the surfaces and large droplets formed before turning into ice beads. Ice nucleation on the hydrophilic surface occurred quickly, leaving less time for disc-like shaped water droplets to continue to grow in the radial and vertical directions before freezing. Frost thicknesses followed “S” shaped like profiles due to transitions of droplets

to ice beads, to crystals growth, and to initial frost accretion on the top of the ice beads. These changeovers were identified by variations of the slope of the frost thickness profiles when plotted vs elapsed time. The wettability characteristics of the surfaces affected the elapsed time at which these changeovers occurred and the thresholds of the frost thickness when switching to the frost growth phase. Hydrophobic surface had early transitions and high thresholds. Implementing these coatings in actual surface designs required further research.

This thesis also presented new preliminary experimental data of frost nucleation and frost growth on cold flat plates operating in frosting conditions with air forced convective flow. The plate surfaces had different wettability from an uncoated aluminum surface with fine finish roughness and contact angle of $\theta \approx 75^\circ$, to hydrophobic ($\theta \approx 110-116^\circ$) coating and hydrophilic ($\theta \approx 19-29^\circ$) coating. Droplets size and freezing times, local temperatures, heat fluxes and rate of frost mass accretion were directly measured by using the newly developed experimental technique. Air entered to the test plate at 5°C (41°F) dry bulb temperature and the effects of plate surface temperature, air relative humidity, and airflow rate on frost nucleation and subsequent frost growth were investigated.

A nitrogen air displacement technique was used to cool the test plate without condensing water onto the surface before the test start time. This technique is unique in that no physical contact is made with the test plate during the test procedure. Air entered to the test plate at 5°C (41°F) dry bulb temperature. The airflow rate was constant at about $8.5 \text{ m}^3/\text{h}$ ($\sim 5 \text{ cfm}$) for the phases of frost nucleation and subsequent frost growth.

The frost thicknesses for the fine-finished aluminum surface and hydrophilic coating were similar. They both had significantly lower thickness during the initial frost accretion period. Then, the frost thickness increased slowly and with almost constant slope for the remaining of the frost

growth phase. The surface wettability characteristics affected the elapsed time and the initial thickness of the frost before the droplets froze on the test plates. They also affected the starting point for the phase changeover from crystal growth to frost growth. During frost nucleation and early frost growth stages, the airside convective heat transfer coefficients were about 60 to 70% lower than that of steady state wet-test value.

At test plate temperature of -3°C , the hydrophilic surface froze quickly while the freezing and the droplets radius were the highest for the hydrophobic surface. However, the freezing time decreased markedly for the hydrophobic surface if the surface temperature decreased from -3 to -7°C or if the air relative humidity increased from 80% R.H. to 95% R.H. In fact, in such conditions, an inversion of trends was observed and the hydrophobic surface resulted in earlier frost nucleation than that in hydrophilic surface. When the air flow rate was decreased by half, resembling low air velocity on the top of the surfaces, the freezing time of the hydrophilic surface increased drastically from 22 minutes to over 80 minutes.

During water vapor condensation and droplets growth the heat transfer coefficients were about $120 \text{ W/m}^2\text{-K}$ for all three surfaces. Because of the constant air flow imposed in our experiments, as droplets began to turn into ice beads and as crystals started to grow on the top of the ice beads, the heat transfer coefficients gradually increased because of the increased air velocity over the test plate as well as the augmented surface roughness created by the frost accumulated on the surfaces.

Recommendations for future work

It is believed that the insulation in the system may be improved. Different insulating materials such as aerogel could be investigated. The effect of the location of the thermocouples can be examined more thoroughly. In addition to horizontal flat plate experiments, investigations

can be made on a vertical flat plate. It could be worthwhile to investigate the effect of micro-patterned coated surfaces. The experimental system developed and data collected from it would be useful to develop and verify a frosting model.

References

- Alizadeh, A., Yamada, M., Li, R., Shang, W., Otta, S., Zhong, S., Ge, L., Dhinojwala, A., Conway, K. R., Bahadur, V., Vinciguerra, A. J., Stephens, B., Blohm, M. L., 2012. "Dynamics of Ice Nucleation on Water Repellent Surfaces" *Langmuir* 28(6), 3180-3186.
- Boreyko, J. B., Srijanto, B. R., Nguyen, T. D., Vega, C., Fuentes-Cabrera, M., Collier, C. P., 2013. "Dynamic Defrosting on Nanostructured Superhydrophobic Surfaces" *Langmuir* 29(30) pp. 9516-9524
- Brian, P. L. T., Reid, R. C., & Shah, Y. T., 1970. "Frost deposition on cold surfaces." *Industrial & Engineering Chemistry Fundamentals* 9(3), 375-380.
- Bryant, J.A., 1995. "Effects of Hydrophobic Surface Treatments on Dropwise Condensation and Freezing of Water." Ph.D. Thesis, Texas A&M University
- Cai, L., Wang, R., Hou, P., & Zhang, X., 2011. "Study on restraining frost growth at initial stage by hygroscopic coating." *Energy and Buildings* 43(5), 1159-1163.
- Cheng, C.-H., and Shiu, C.-C., 2002. "Frost formation and frost crystal growth on a cold plate in atmospheric air flow." *International Journal of Heat and Mass Transfer* 45(21), 4289-4303.
- Cremaschi, L., Harges, E., Adanur, B., and Strong, A., 2018. "Frost nucleation and frost growth on hydrophobic and hydrophilic surfaces for heat exchangers fin structures." *Proceedings of the 17th International Refrigeration and Air Conditioning Conference at Purdue University, West Lafayette, IN (USA), July 9-12, Paper No. 2508, Pages 1-10.*
- Cremaschi, L., Hong, T., Moallem, E., and Fisher, D. (2012). "Measurements of Frost Growth on Louvered Folded Fins of Microchannel Heat Exchangers Part 1: Experimental Methodology." (RP-1589) (CH-12-034). *ASHRAE Transactions*. 118.

- Haque, M., R., and Betz, A., R., 2018. "Frost Formation on Aluminum and Hydrophobic Surfaces." Proceedings of the ASME 2018 International Conference on Nanochannels, Microchannels, and Minichannels (ICNMM 2018), Paper No. ICNMM2018-7609, June 10-13, Dubrovnik, Croatia.
- Harges, E., and Cremaschi, L., 2018a, A New Model for Frost Growth Incorporating Droplet Condensation and Crystal Growth Phases, ASHRAE Transactions, ASHRAE Conference Paper, ASHRAE Winter Conference, Chicago, IL, USA, Jan 20 - 24. Conference Proceedings
- Harges, E., Cremaschi, L., 2018b, Modeling of Frost Growth On Surfaces With Varying Contact Angle, Paper TFEC-2018-20908, Proceedings of the 3rd Thermal and Fluid Engineering Conference, Ft. Lauderdale, FL, Mar 4-7. Conference Proceedings
- Hayashi, Y., Aoki, A., Adachi, S., & Hori, K., 1977. "Study of frost properties correlating with frost formation types." *Journal of Heat Transfer* 99(2), 239-245.
- Hermes, C. J. L., Piucco, R. O., Barbosa Jr., J. R., & Melo, C., 2009. "A study of frost growth and densification on flat surface." *Experimental Thermal and Fluid Science* 33(2), 371-379.
- Hermes, C., J., L., Sommers, A., D., Gebhart, C.W., and Nascimento, V. S., 2018. "A semi-empirical model for predicting the frost accretion on hydrophilic and hydrophobic surfaces." *Int. J. Refrig.*
- Hermes, C., J., L., Sommers, A., D., Gebhart, C., W., and Nascimento, V., S., 2018, A semi-empirical model for predicting the frost accretion on hydrophilic and hydrophobic surfaces, *Int. J. Refrig.*, 100, pages 76-88. Journal Paper
- Hoke, J.L., Georgiadis, J.G., Jacobi, A.M., 2000. "The Interaction between the Substrate and Frost Layer through Condensate Distribution." *Air Conditioning and Refrigeration Center, College of Engineering, University of Illinois at Urbana-Champaign.*
- Huang, L., Liu, A., Liu, Y., & Gou, Y., 2010. "Experimental study of frost growth on a horizontal cold surface under forced convection." *Journal of Mechanical Science and Technology* 24(7), 1523-1529.
- Huang, L., Liu, Z., 2010. "Effect of contact angle on water droplet freezing process on a cold flat surface." *Experimental Thermal and Fluid Science* 40 pp. 74-80.

- Huang, L., Liu, Z., Liu, Y., Gou, Y., and Wang, L., 2012, Effect of contact angle on water droplet freezing process on a cold flat surface, *Exp. Therm. Fluid Sci.* 40, pp. 74-80. Journal Paper
- Janssen, D., 2013. "Experimental strategies for frost analysis." Doctoral dissertation, University of Minnesota.
- Kim, H., Kim, D., Jang, H., Kim, D.R., Lee, K.S., 2016. "Microscopic observation of frost behaviors at the early stage of frost formation on hydrophobic surfaces." *Int. J. Heat Mass Transf.*, 97, pp. 861-867.
- Kim, K., and Lee, K., S., 2011, Frosting and defrosting characteristics of a fin according to surface contact angle, *Int. J. Heat Mass Transfer* 54, pp. 2758-2764. Journal Paper
- Kim, M. H., Kim, H., Lee, K. S., Kim, D. R., 2017. "Frosting characteristics on hydrophobic and superhydrophobic surfaces: A review." *Energy Conversion and Management* 138 pp. 1-11
- Kim, M-H, Kim, H., Lee, K-S, and Kim, D-R, 2017, Frosting characteristics on hydrophobic and superhydrophobic surfaces: A review, *Energy Conversion and Management* 138, pp. 1–11. Journal Paper
- Lee, H., Shin, J., Ha, S., Choi, B., and Lee, J., 2004, Frost formation on a plate with different surface hydrophilicity, *Int. J. Heat Mass Transfer* 47 pp. 4881-4893. Journal Paper
- Lee, H., Shin, J., Ha, S., Choi, B., and Lee, J., 2004. "Frost formation on a plate with different surface hydrophilicity." *Int. J. Heat Mass Transfer* 47 pp. 4881-4893.
- Lee, K.-S., Jhee, S., and Yang, D.-K., 2003. "Prediction of the frost formation on a cold flat surface." *International Journal of Heat and Mass Transfer* 46(20), 3789-3796.
- Lee, K.-S., Kim, W.-S., and Lee, T.-H., 1997. "A one-dimensional model for frost formation on a cold flat surface." *International Journal of Heat and Mass Transfer* 40(18), 4359-4365.
- Leoni, A., Mondot, M., Durier, F., Revellin, R., & Haberschill, P., 2017. "Frost formation and development on flat plate: Experimental investigation and comparison to predictive methods." *Experimental Thermal and Fluid Science* 88, 220-223.

- Moallem, E., 2012. "Experimental and theoretical investigation of effect of fin geometry on frost formation on microchannel heat exchangers." Doctoral dissertation, Oklahoma State University, Stillwater, Oklahoma
- Rahman, M., A., and Jacobi, A., M., 2015, Effects of microgroove geometry on the early stages of frost formation and frost properties, *App. Therm. Eng.* 56, pp. 91-100. Journal Paper
- Sahin, A. Z., 1994. "An experimental study on the initiation and growth of frost formation on a horizontal plate." *Experimental Heat Transfer* 7(2), 101-119.
- Schmiesing, N. C., Sommers, A. D., 2017. "Defrosting performance on hydrophilic, hydrophobic, and micro-patterned gradient heat transfer surfaces." *Science and Technology for the Built Environment* 23(6) pp. 946-959
- Siegel, R., & Howell, J., 2002. "Thermal radiation heat transfer: 4th edition." New York, NY: Taylor and Francis.
- Sommers, A. D., Gebhart, C. W., Hermes, C. J.L., 2018. "The role of surface wettability on natural convection frosting: Frost growth data and a new correlation for hydrophilic and hydrophobic surfaces." *International Journal of Heat and Mass Transfer* 122 pp. 78-88.
- Sommers, A. D., Truster, N. L., Napora, A. C., Riechman, A. C., Carballo, E. J., 2016. "Densification of frost on hydrophilic and hydrophobic substrates - Examining the effect of surface wettability" *Experimental Thermal and Fluid Science* 75 pp. 25-34.
- Sommers, A., D., Gebhart, C., W., and Hermes, C., J., 2018, The role of surface wettability on natural convection frosting: Frost growth data and a new correlation for hydrophilic and hydrophobic surfaces, *Int. J. Heat Mass Transfer* 122, pp. 78-88. Journal Paper
- Song, M. and Dang, C., 2018. "Review on the measurement and calculation of frost characteristics" *International Journal of Heat and Mass Transfer* 124 pp. 586-614
- Tao, Y.-X., Besant, R.W., Mao, Y., 1993. "Characteristics of Frost Growth on a Flat Plate during the Early Growth Period." *ASHRAE Transactions: Symposia*, CH-93-2-2, 746-753.

- Tourkine, P., Merrer, M. L., Quéré, D., 2009. "Delayed Freezing on Water Repellent Materials"
Langmuir 25(13) PP. 7214-7216
- Wang, W., Gou, Q. C., Lu, W. P., Feng, Y. C., & Na, W. (2012). A generalized simple model for predicting frost growth on a cold flat plate. International Journal of Refrigeration 35(2), 475-486.
- Wu, X., Dai, W., Shan, X., Wang, W., and Tang, L., 2007, Visual and theoretical analyses of the early stage of frost formation on cold surfaces, J. Enhanced Heat Transfer, 14, pp. 257-268. Journal Paper
- Yang, D.-K., and Lee, K.-S., 2004. "Dimensionless correlations of frost properties on a cold plate."
International Journal of Refrigeration 27(1), 89-96.
- Yoon, S., Hayase, G., and Cho, K., 2010. "Measurements of frost thickness and frost mass on a flat plate under heat pump condition." Heat Transfer Engineering 31(12), 965-972.
- Yun, R., Kim, Y., and Min, M., 2002. "Modeling of frost growth and frost properties with airflow over a flat plate." International Journal of Refrigeration 25(3), 362-371.